Low Energy States In Hybrid Semiconductor-Superconductor Majorana Devices

by

Peng Yu

Bachelor of Science, Jilin University, 2012

Submitted to the Graduate Faculty of

the Kenneth P. Dietrich School of Arts and Sciences in partial fulfillment

of the requirements for the degree of

Doctor of Philosophy

University of Pittsburgh

2020

UNIVERSITY OF PITTSBURGH

KENNETH P. DIETRICH SCHOOL OF ARTS AND SCIENCES

This dissertation was presented

by

Peng Yu

It was defended on

August 27, 2020

and approved by

Sergey M. Frolov, Associate Professor, Department of Physics and Astronomy

Michael Hatridge, Assistant Professor, Department of Physics and Astronomy

Roger Mong, Assistant Professor, Department of Physics and Astronomy

Michael Wood-Vasey, Associate Professor, Department of Physics and Astronomy

Daniel Lambrecht, Assistant Professor, Department of Chemistry

Low Energy States In Hybrid Semiconductor-Superconductor Majorana Devices

Peng Yu, PhD

University of Pittsburgh, 2020

Majorana zero-energy modes (MZMs), which comprise an equal superposition of electrons and holes, are predicated to emerge as quasiparticles in condensed matter systems. MZMs has generated significant interest in recent years, mostly because they are anticipated to obey non-Abelian statistics and thus can be potentially exploited in topological quantum computation. Among various proposals for realizing MZMs, semiconductor nanowires with strong spin-orbit coupling and proximity induced superconductivity is a promising platform. Although several experiments have already reported the possible signature of MZMs in such a system, a conclusive proof of MZMs is still an ongoing effort. Moreover, none of them verified the long-standing prediction that MZMs should emerge in pairs with one at each end of a topological region.

In this thesis, we first improved the required ingredients for generating MZMs. By optimizing the nanowire-superconductor interfaces as well as the NbTiN superconducting films, we achieved hard induced gaps and ballistic transport in InSb nanowires. We also optimized local bottom gates aimed to achieve better chemical potential control in nanowires.

With those improvements, in a two-terminal device, we found zero bias conductance peaks (ZBCPs) in agreement with the Majorana theories. We also mapped out a phase diagram of the ZBCPs in the magnetic field and chemical potential space. While this data favors the Majorana origin of the ZBCPs, non-Majorana ZBCPs emerge as ubiquitous features in similar devices. Due to the similarities between these ZBCPs, we conclude it is impractical to unambiguously prove MZMs in a two-terminal geometry.

In a three-terminal geometry, we gain the ability to probe the two ends of the nanowire-superconductor hybrid region by adding one more normal lead. We identified delocalized states near zero field, which emerged with correlated gate dependence on both ends. While the correlation between the ZBCPs on both ends at finite fields was not established, we

demonstrated three-terminal geometry is a powerful method of diagnosing localization of wavefunctions. Future experiments can thus use this method to identify MZMs from localized trivial states. Once MZMs can be deterministically established, braiding experiments in nanowire networks could open the gate to topological quantum computation.

Table of Contents

List of Figures

1.0 Introduction

1.1 History of Majorana Fermions

When Dirac derived the famous Dirac equation in 1928, in addition to captured the physical behavior of spin-1/2 massive particles, he also hypothesized a new type of particles—antiparticles that possess the opposite physical charges to their associated particles [2]. These two types of particles are both solutions of the Dirac equation and are related via complex conjugation. The hypothesis was confirmed by the observation of positron in cosmic rays several years later [3]. The simple concept that all half-integer spin particles should be different from their associated antiparticles, however, were challenged by Majorana with a real solution to the Dirac equation in 1937 [4]. The real solution to the Dirac equation implies the existence of another class of fermions that are their own antiparticles and own no charge. The hypothetical fermion was named after Majorana and the search for Majorana fermions started ever since. In particle physics, Neutrino is a candidate for Majorana fermion since the beginning and today particle physicists are still studying the possible Majorana property in neutrino propagating [5]. Due to its elusive characteristic, however, whether Neutrino is a Majorana fermion is still an unknown question. Moreover, no elementary particle has been proved to be Majorana fermions to date. In condensed matter, Majorana fermions are predicted to appear as zero-dimensional bound states in topological defects and exhibit non-Abelian statistics upon exchanging. The coveted non-Abelian statistic give Majorana fermions the ability to process quantum information robustly [6]. Furthermore, the topological origin may free Majorana fermion from dephasing when used for qubit [7]. Due to those fascinating properties, people are spurred to search Majorana fermions in condensed matter.

1.2 Majorana Fermions in Topological Superconductor

While the early proposal for Majorana fermions in condensed matter came almost two decades ago [8], it requires unconventional p-wave superconductivity, which is hard to be found in materials. It was until Fu and Kane suggested that instead of engineering the material, the p-wave paring can be effectively built by combining conventional superconductor to topological insulator [9], this area gathered increasing interest and many proposals were developed following the similar manner. And in 2010, two independent works [10, 11] lowered the requirement for creating Majorana fermions again by replacing topological insulator with topological superconductor. The proposed system consists of a one-dimensional semiconductor with spin-orbit coupling in contact with a conventional s-wave superconductor.

These two proposals fueled a significant amount of experiments since then, together with the development in materials science in searching for better semiconductors and superconductors. While the first signature of Majorana fermion in one-dimensional semiconductor was reported in 2012 [12], the fundamental questions of whether well-separated Majorana fermions, which are prerequisites for topological quantum computation, can emerge in such systems have not been answered unambiguously. Motivated by this question, we devoted to engineer the optimal platforms for Majorana fermions as well as to carefully distinguish Majorana signal from other similar phenomena.

1.3 Outline of the Thesis

The content of this thesis is as follow:

Chapter 2 introduces the background and theory of Majorana fermions in condensed matter.

Chapter 3 describes the materials, fabrication methods and measurement setups used in this thesis.

Chapter 4 presents the methods have been taken to improve induced superconductivity in the nanowires.

Chapter 5 studies the possible signals of Majorana fermions in two-terminal devices.

Chapter 6 demonstrates the existence of delocalized states in three-terminal devices and shows how to distinguish non-Majorana signals.

Chapter 7 concludes the thesis with a summary of the state of art and a future outlook.

2.0 Theory Introduction

2.1 Introduction

Majorana zero modes (MZMs) in condensed matter physics has been predicated to emerge as quasiparticles. They evoked significant interest in physics and material science mostly due to its great potential in topological quantum computing [6]. As effective zero-energy states, MZMs are predicted to obey exotic non-Abelian statistic [13, 14]. As the result, operations involving exchanging the position of MZMs lead to topologically protected nontrivial transformation, which can be exploited for a naturally fault-tolerant qubits [6, 7, 15].

Many platforms [16, 17, 18, 19, 20] have been proposed for realizing MZMs by engineering a proper Hamiltonian in edges or interfaces of topological insulators, magnetic atom chains and semiconductors with spin-orbit interaction. Among those proposals, one dimensional semiconductor nanowire with proximity induced superconductivity [10, 11]is one of the most promising candidates. Starting with the toy model proposed by Kitaev in 2001 [21], a huge amount of effort in both theory and experiment has been spent to dress the model with realistic ingredients and to obtain an unambiguous prove of the existence of MZMs. While the first signature of MZMs has been reported eight years ago [12] and tremendous advances has been achieved in this area since then, a deterministic observation of MZMs and their exotic properties is still an ongoing task.

2.2 Majorana Fermions in Condensed Matter

2.2.1 Majorana Operators

In condensed matter, Majorana zero modes can emerge as quasiparticles, which are equal superposition of electrons and holes. We use the term 'zero mode' as they are supposed to

be zero-energy excitations. Before introducing Majorana zero modes and discussing their properties in condensed matter context, it is beneficial to first introduce Majorana formalism based on fermionic creation and annihilation operators in the manner of second quantization.

In the simplest case of single fermionic site, the empty and occupied state can be described as $|0\rangle \equiv \begin{pmatrix} 1 \\ 0 \end{pmatrix}$ and $|1\rangle \equiv \begin{pmatrix} 0 \\ 1 \end{pmatrix}$.

The fermionic creation and annihilation operators can be defined as

$$c_1^+ = |1\rangle\langle 0| = \begin{pmatrix} 0 & 0 \\ 1 & 0 \end{pmatrix}, c_1 = |0\rangle\langle 1| = \begin{pmatrix} 0 & 1 \\ 0 & 0 \end{pmatrix} \tag{2.1}$$

Majorana operators can then be constructed by splitting fermionic operators:

$$\gamma_1 = c_1 + c_1^+ = \begin{pmatrix} 0 & 1 \\ 1 & 0 \end{pmatrix} = \sigma_x \tag{2.2}$$

$$\gamma_2 = -i\left(c_1 - c_1^+\right) = \begin{pmatrix} 0 & -i \\ i & 0 \end{pmatrix} = \sigma_y \tag{2.3}$$

with

$$c_1^+ = \frac{\gamma_1 - i\gamma_2}{2}, c_1 = \frac{\gamma_1 + i\gamma_2}{2} \tag{2.4}$$

Obviously Majorana creation operator and annihilation operator are identical: $\gamma_1 = \gamma_1^+$ and $\gamma_2 = \gamma_2^+$, which satisfies the Majorana definition: being its own antiparticle. We also have $\gamma_1^2 = \gamma_2^+ = 1$. That means a state remains the same after being changed by a Majorana operator twice, while $c^2 = \left(c^\dagger\right)^2 = 0$ for normal fermion operators. This also implies Majoranas do not obey Pauli principle. It is worth noting that the occupancy makes no sense for a Majorana state. Since $n_i^{\mathrm{MF}} = \gamma_i^\dagger \gamma_i = \gamma_i \gamma_i^\dagger = 1$, the Majorana state is empty and filled at the same time, which has no physical meaning.

Using Majorana operators, fermion number operators for single fermionic state can be written as

$$\hat{\mathcal{N}} = c_1^\dagger c_1 = \frac{1 - i\gamma_2\gamma_1}{2} \tag{2.5}$$

And the fermion parity operator for single site takes the form

$$\hat{\mathcal{P}} = 1 - 2c_1^\dagger c_1 = i\gamma_2\gamma_1 = \sigma_z = (-1)^{\hat{N}} \tag{2.6}$$

The parity number is then +1 for the unoccupied state $|0\rangle$ and -1 for the occupied state $|1\rangle$.

For a more general case with N fermion sites, $c_n^\dagger$ and c_n are the creation and annihilation operators for site n, where n = 1, 2 ,$\cdots$, N. They satisfy fermionic anti-commutation relations,

$$\left\{c_i, c_j^\dagger\right\} = \delta_{ij} \tag{2.7}$$

$$\{c_i, c_j\} = \left\{c_i^\dagger, c_j^\dagger\right\} = 0 \tag{2.8}$$

With N fermion operators, there are 2N Majorana operators

$$\gamma_{2n-1} = c_n + c_n^\dagger \tag{2.9}$$

$$\gamma_{2n} = -i\left(c_n - c_n^\dagger\right) \tag{2.10}$$

Following the fermionic anti-commutation relations, we can see Majorana operators obey a modified anti-commutation relation:

$$\{\gamma_i, \gamma_j\} = 2\delta_{ij} \tag{2.11}$$

The fermion number operator for site n can be written as

$$\hat{\mathcal{N}_n} = c_n^\dagger c_n = \frac{1 - i\gamma_{2n-1}\gamma_{2n}}{2} \tag{2.12}$$

And the total parity operator has the form

$$\hat{\mathcal{P}_{tot}} = i\gamma_{2N}\gamma_{2N-1}\cdots i\gamma_2\gamma_1 = (-1)^{\sum_{n=1}^{N}\hat{N}_n} \tag{2.13}$$

Now we introduced Majorana formalism and expressed fermionic number and parity operators with Majorana operators. The fact that Majorana operators are defined by splitting a fermion operator implies two paired Majorana fermions just behave like a Dirac fermion and possess no special properties. To show the exotic properties of Majorana fermions, we need to make them isolated from each other.

2.2.2 Majorana Fermions in One Dimensional Kitaev Chain

Before exploring more properties of Majorana fermions, we use a simple model to demonstrate how Majorana fermions can emerge in one dimensional (1D) system.

The story of Majorana fermions in 1D superconducting system starts with the so-called Kitaev model [21]. First introduced in 2001 by Alexei Kitaev, the model describes a N-site 1D tight binding chain occupied by spinless fermions with p-wave superconductivity.

The Kitaev chain has the Hamiltonian:

$$\mathcal{H}_{\text{chain}} = -\mu \sum_{n=1}^{N} \left(c_n^\dagger c_n - \frac{1}{2} \right) - \sum_{n=1}^{N-1} \left(t c_n^\dagger c_{n+1} + \Delta c_n c_{n+1} + h.c. \right) \tag{2.14}$$

where n represents the number of the site, μ is the chemical potential, t is the hopping amplitude between nearby sites and Δ describes superconducting gap in the chain. Superconducting pairing Δ and hopping amplitude t are treated as uniform across all the sites. The superconducting phase is set to be zero so that $\Delta = |\Delta|$. Note the p-wave superconductivity only pairs neighboring electrons with the same spin, therefore spin label can be omitted in the Hamiltonian and electrons in the model are effectively spinless. Because of Pauli exclusion principle, each site can only hold one electron. As discussed in the previous section, each fermion operator can be written as two Majorana operators and the Kitaev Hamiltonian can be written as:

$$\mathcal{H}_{\text{chain}} = -\frac{i}{2}\mu \sum_{n=1}^{N} \gamma_{n,1}\gamma_{n,2} + \frac{i}{2} \sum_{n=1}^{N-1} \left((t + |\Delta|)\gamma_{n,2}\gamma_{n+1,1} + (-t + |\Delta|)\gamma_{n,1}\gamma_{n+1,2} \right) \tag{2.15}$$

where $\gamma_{n,1}$ and $\gamma_{n,2}$ are the the first and second Majorana operators living on site n respectively. Without solving the full Hamiltonian, two special cases can illustrate the scenario with and without Majorana physics in this model.

First, consider the trivial case where $t = \Delta = 0$, i.e. no hopping and superconductivity, and $\mu < 0$, the Hamiltonian only keeps the first term:

$$\mathcal{H}_{\text{chain}} = -\frac{i}{2}\mu \sum_{n=1}^{N} \gamma_{n,1}\gamma_{n,2} \tag{2.16}$$

We call this trivial case since Majorana fermions pairs within each site and form normal Dirac fermions. This case is illustrated by Fig. 2.1(a).

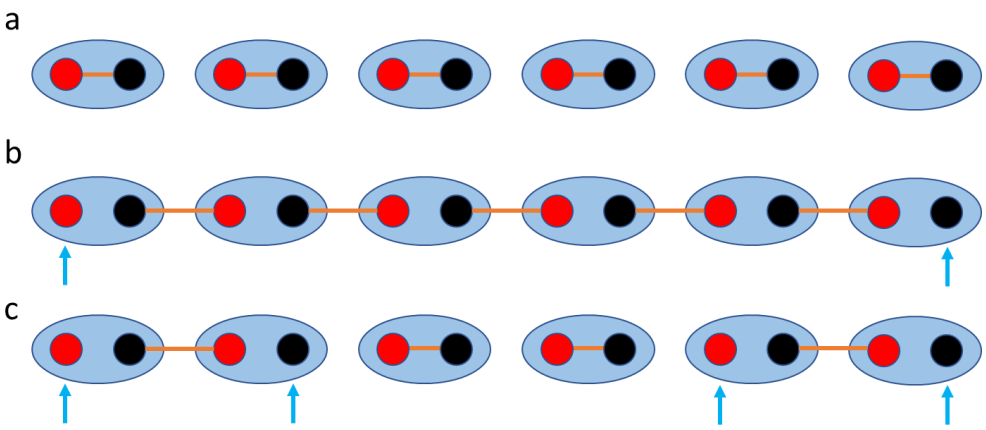

Figure 2.1: **A schematic of the Kitaev chain.** Each fermionic site is indicated by a blue oval. Isolated Majorana fermions are indicated by light blue arrows. **a**, trivial case where Majorana fermions from the same site are coupled. **b**, nontrivial case where tunnel coupling pairs Majoranas from different sites. **c**, the system has two separate topological regions with each region hosts a pair of Majoranas.

For the non-trivial case where $\mu = 0$ and $t = \Delta$ (Fig. 2.1(b), the full Hamiltonian also reduces to a very simple form:

$$\mathcal{H}_{\text{chain}} = -it \sum_{n=1}^{N-1} \gamma_{n,2}\gamma_{n+1,1} \tag{2.17}$$

In contrast to the trivial case, Majoranas from nearby sites are paired now. By combining the two neighboring Majoranas from two sites, we can define a new fermion operator:

$$\tilde{c}_n = \left(\gamma_{n+1,1} + i\gamma_{n,2}\right)/2 \tag{2.18}$$

with $-i\gamma_{i,2}\gamma_{i+1,1} = 2\tilde{c}_i^\dagger \tilde{c}_i = 2\tilde{n}_i$, Eq.2.17 can be written as

$$\mathcal{H}_{\text{chain}} = 2t \sum_{n=1}^{N-1} \tilde{c}_n^\dagger \tilde{c}_n - 1 \tag{2.19}$$

In Eq.2.19, those new defined fermions are a superposition of neighbor Majoranas from different sites. It may look trivial to just combine Majoranas into fermions, but the consequence is profound. As the first Majorana $\gamma_{1,1}$ and the last Majorana $\gamma_{N,2}$ in the chain are completely missing from Eq.2.19, adding or removing these two Majorana fermions thus requires no energy. And if we construct a new fermion using these two Majoranas, we will have a highly non-local operator combining the first and last Majoranas:

$$\tilde{c}_M = (\gamma_{1,1} + i\gamma_{N,2})/2 \tag{2.20}$$

Since this new nonlocal fermion operator is also missing from the Hamiltonian, no energy is required to occupy it. As the result, the ground state becomes two-fold degenerate, corresponding to with and without the nonlocal state being occupied. It should be noted that the two-fold ground state can have either even or odd parity. In contrast, a normal superconductor can only have a non-degenerate ground state with even parity due to the condensation of Cooper pairs.

In a more general cases with non-zero μ, t, Majorana zero modes appear as long as μ lies inside the gap set by t, namely $|\mu| < 2t$. To see this, we Fourier transformer the Kitaev Hamiltonian by first transforming the creation and annihilation operators:

$$c_{\mathrm{n}}^{\dagger} = \frac{1}{\sqrt{N}} \sum_{-\infty}^{\infty} e^{ik\cdot x_n} c_{\mathrm{k}}^{\dagger} \qquad c_{\mathrm{n}} = \frac{1}{\sqrt{N}} \sum_{-\infty}^{\infty} e^{-ik\cdot x_n} c_{\mathrm{k}} \tag{2.21}$$

Since we are studying a Hamiltonian with superconductivity, it is helpful to use the Bogoliubov-de Gennes formalism (More information about superconductivity and the formalism can be found in [22]). The resulting Hamiltonian is in k-space and has the Bogoliubov-de Gennes matrix form:

$$H = \frac{1}{2} \sum_{k=0}^{\infty} \left[C_k^{\dagger} \right] H_{\mathrm{BdG}} \left[C_k \right] \tag{2.22}$$

Where $C_k = \begin{bmatrix} c_{\mathrm{k}} \\ c_{-\mathrm{k}}^{\dagger} \end{bmatrix}$ and

$$H_{\mathrm{BdG}} = \begin{bmatrix} \mu - 2t\cos(k) & -2i\Delta\sin(k) \\ 2i\Delta\sin(k) & -\mu + 2t\cos(k) \end{bmatrix} \tag{2.23}$$

Using the Pauli matrices τ in particle-hole space, the Bogoliubov-de Gennes Hamiltonian can be expressed in a more compact form:

$$H_{\mathrm{BdG}} = (-2t\cos k - \mu)\tau_z + 2\Delta\tau_y \sin k \tag{2.24}$$

Diagonalizing the Hamiltonian yields the bulk energy spectrum:

$$E(k) = \pm\sqrt{(2t\cos(k) - \mu)^2 + 4|\Delta|^2 \sin^2(k)} \tag{2.25}$$

With chemical potential μ placed within the $2t$ energy gap, Majorana zero modes still emerge around the end of the chain. Their wavefunctions, in contrast to the $\mu = 0$, $t = \Delta$ case, are no longer localized exactly at the two edge sites. Instead, they have tails extended to the bulk, which decays exponentially away from the edge.

No Majorana zero modes appears any more once $|\mu|$ is larger than $2t$(Fig.2.1(b)). More specifically, $|\mu| = 2t$ is the topological phase transition point, while $|\mu| < 2t$ indicating a topologically nontrivial phase and $|\mu| > 2t$ corresponding to a topologically trivial phase. Moreover, for non-uniform μ, the system may have multiple regions satisfying $|\mu| < 2t$ and each topologically nontrivial region can host a pair of Majorana zero modes as shown in Fig. 2.1(c).

The trivial and nontrivial cases can also be illustrated in energy spectrum and wave function amplitude plots Fig. 2.2. For $t = \Delta$ and $\mu = 0$ (Fig. 2.2(a)), Majorana zero modes appear in the middle, i.e. zero energy, of the energy spectrum and are separated by an energy gap of $2t$ from excited states. Wavefunctions of Majorana zero modes (Fig. 2.2(b)) are perfectly localized at the end sites.

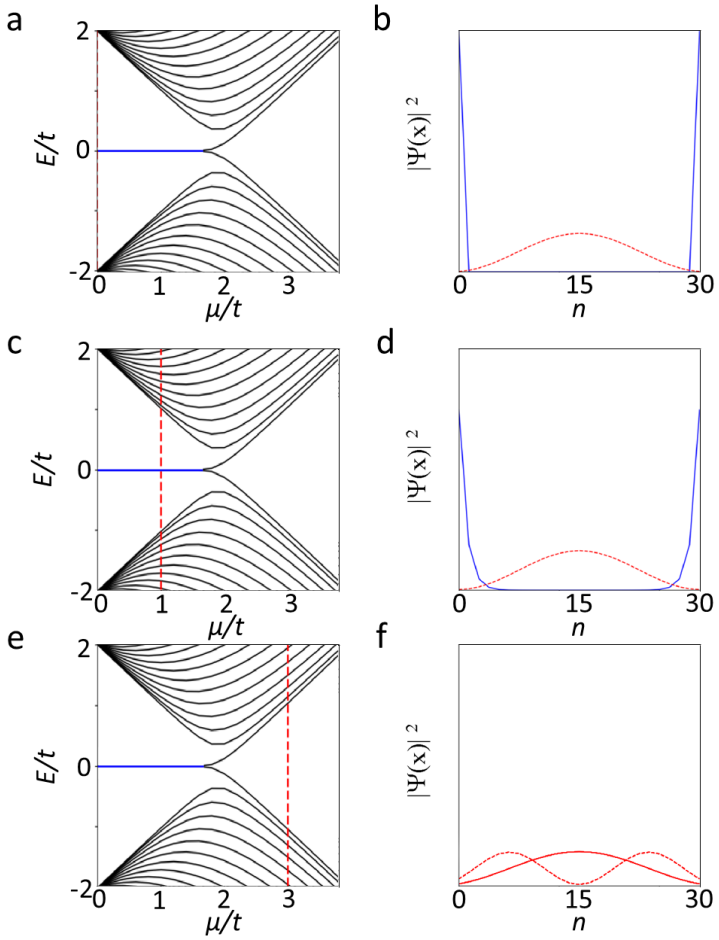

Figure 2.2: **Energy spectrum and wavefunction space dependence of the Kitaev model. a and b**, For $|\mu| = 0$, the system is topologically nontrivial with Majorana zero-energy modes and the bulk is gaped. The two Majorana wavefunctions (blue curve) localized exactly at the end site, while the first excited state (red curve) live in the bulk. The red dashed lines in panel **a, c and e** indicate the setting of $|\mu|$. **c and d**, For $|\mu| = t$, the system is still nontrivial and hosts Majorana zero modes, while the bulk gap is smaller and the Majorana wavefunctions have tails extended into the bulk. **e and f**, For $|\mu| = 3t$, they system is trivial without any zero-energy mode.

For $0 < |\mu| < 2t$, Majorana zero modes still remain at zero energy (Fig. 2.2(c)), but the energy gap shrinks and Majorana wavefunctions exhibit tails into the bulk sites (Fig. 2.2(d)). For $|\mu| > 2t$, the bulk energy gap is closed leaving no more zero-energy state (Fig. 2.2(e)(f)). It is worth noting that the two initially uncoupled Majorana wavefunctions are overlapping now. Actually, coupling the two Majorana modes is the only way to move their energy levels from zero. On the contrary, if the bulk is gaped and the two Majorana zero modes are not coupled, it is impossible to change the Majorana zero modes individually as it would break particle-hole symmetry. That protection, which gives Majoranas great potential in quantum computation, is an important property of those Majorana zero modes in the Kitaev chain. As a consequence, if we can use Majoranas to build a qubit, it should be immune to local perturbation.

While mathematically beautiful, Kitaev chain model has several unrealistic assumptions. First, it works with spinless fermion, which does not exist in real life. Second, superconducting pairing in the Hamiltonian couples electrons from different sites, which means the pairing is proportional to the first power of momentum. Such an exotic superconducting pairing only exists in p-wave superconductor and is still out of reach in experiments. We will discuss how to solve those problems and have a more realistic model in section 2.4.

2.3 Properties of Majorana Fermions

Before introducing a more realistic Majorana model, we will talk about some important properties of Majorana fermions that make them so fascinating. First, we discuss the Hilbert space of a set of Majorana fermions and its degeneracy. Assuming we have N pairs of Majorana fermions in a Kitaev chain with the condition $|\mu| < 2t$, we can neglect the excited states in the bulk since they are gaped and irrelevant to the zero energy Majorana edge states. As shown in Eq.2.17, two Majorana zero modes are missing from the Hamiltonian, so there must be some degenerate quantum states. Also since Majorana zero modes always appear in pairs, we can only assign quantum states to a pair of Majorana.

To assign quantum states to Majoranas, it is intuitive to pair them into fermionic modes.

And for each fermionic mode, there can be two degenerate quantum states $|0\rangle$, $|1\rangle$ corresponding to an empty or an occupied fermionic mode. Generalizing, for a system with N pairs of Majoranas, the ground state will be 2^N fold degenerate.

Now consider the occupation number a_n of the n-th fermionic mode, where a_n is 0 if the site is not occupied and +1 if the site is occupied. All those number states make a complete basis of the Hilbert space of the system.

Those states are also eigenstates of the fermion parity operator: $P_n \equiv 1 - 2c_n^\dagger c_n \equiv i\gamma_{2n-1}\gamma_{2n}$, for example:

$$P_1|0,\ldots\rangle = \left(1 - 2c_1^\dagger c_1\right)|0,\ldots\rangle = +|0,\ldots\rangle \tag{2.26}$$

$$P_1|1,\ldots\rangle = \left(1 - 2c_1^\dagger c_1\right)|1,\ldots\rangle = -|1,\ldots\rangle \tag{2.27}$$

Since different Majorana operators obey the modified anti-commutation relation (Eq.2.11), products of two Majorana operators commute with each other when no Majorana operator is shared by the two pairs, for example:

$$(\gamma_1\gamma_2)(\gamma_3\gamma_4) = (\gamma_3\gamma_4)(\gamma_1\gamma_2) \tag{2.28}$$

However, if a Majorana appears in both pairs, then they no longer commute with each other. In fact

$$(\gamma_1\gamma_2)(\gamma_2\gamma_3) = -(\gamma_2\gamma_3)(\gamma_1\gamma_2) \tag{2.29}$$

Since each $P_n \equiv i\gamma_{2n-1}\gamma_{2n}$ only involve Majorana operators from the same site and no Majorana is shared by different P_ns , all P_ns commute with each other. The eigenstates of $|a_1, a_2, \ldots, a_N\rangle$ thus spans the Hilbert space of a set of N pairs of Majorana modes. And the state $|\Psi\rangle$ for N pairs of Majorana modes can be written as:

$$|\Psi\rangle = \sum_{a_n=0,1} \alpha_{a_1 a_2 \ldots a_N} |a_1, a_2, \ldots, a_N\rangle \tag{2.30}$$

where $\alpha_{a_1 a_2 \ldots a_N}$ is a complex coefficient.

It is worth noting that while the total electron number in a superconducting Hamiltonian can vary due to the creation and annihilation of Cooper pairs, the parity in the system is conserved. Because a closed Majorana system has fixed parity, we actually need N+1 pairs of Majoranas to achieve 2^N degenerate states, e.g. for a qubit with two levels, two pairs of Majoranas are the minimum requirement.

The total fermion parity can be obtained by multiplying all the single fermion parity operator P_n:

$$P_{\text{tot}} = P_1 \cdot P_2 \cdot \ldots \cdot P_N = i^N \gamma_1 \gamma_2 \ldots \gamma_{2N} \tag{2.31}$$

It has an eigenvalue of ± 1, depending on the total occupation number is odd or even. Generally, the above consideration only applies to closed systems. An open system or a subsystem of a closed system may not have conserved parity numbers.

2.3.1 Non-Abelian Exchange Statistics

One of the most important properties of Majorana fermions is they are predicted to obey the exotic non-Abelian exchange statistic in two-dimensional or effective two-dimensional systems[14, 13, 8, 23, 24]. Together with the fact that Majorana fermions are the simplest non-Abelian particles, Majorana fermions are considered to have great potential in fault tolerant quantum computation [6].

In quantum mechanics, anyons are predicted to exist only in two dimensions and can have fractional quantum value, e.g. fractional charge. Due to their two-dimensional (2D) origin, they have less restricted properties than three-dimensional particles like bosons and fermions.

Their special properties also emerge upon particle exchange. In space of three or higher dimensions, particle exchange can only result in a phase shift to the initial quantum state. For bosons, the phase shift is 0 and the initial state is thus multiplied by 1. For fermions, the initial state is multiplied by -1 due to the phase shift of π. But for anyons, particle exchange can multiply the initial state by a unitary operator instead of just multiplying by ± 1. Based on their behavior upon exchange, anyons follow either Abelian statistic or non-Abelian statistic. Abelian anyons still obtain a phase factor upon particle exchange, but

the phase is no longer restricted to 0 or π.

In general, a system with non-Abelian anyons has some degenerate states that have the same particle positions and it is possible to send the system to a different state by exchanging the particles. In other words, the subspace of these degenerate states must have more than one dimensions, and then the linear transformations corresponding to particle exchange need not commute. As mentioned at the beginning, Majorana fermions in 2D or effective 2D, i.e. 1D network, are predicted to be non-Abelian anyons. The two-particle exchange process is often called braiding.

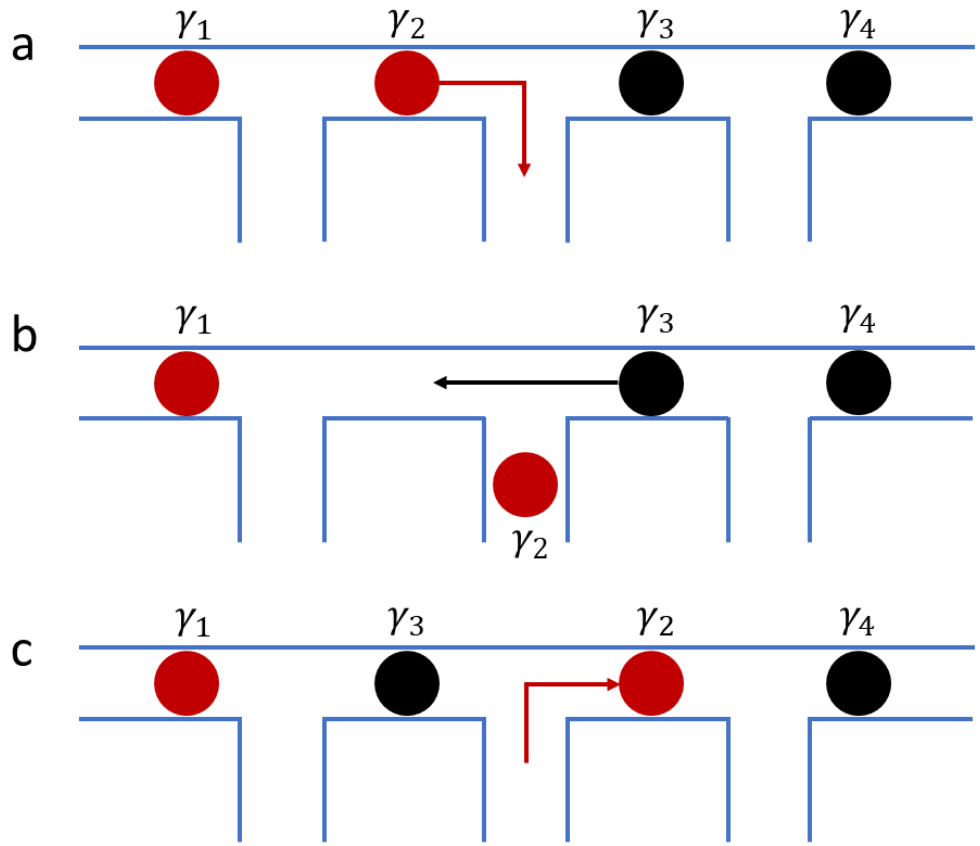

Figure 2.3: **Illustration of Majorana braiding operation.** In a 1D network with two pairs of Majoranas, positions of nearby Majoranas can be exchanged using the T junction. A topologically nontrivial braiding operation alters the initial state by swapping the positions of two Majoranas from different pairs. The final state is degenerate with the initial state.

To illustrate the idea of braiding, assume we have built a network of N pairs of Majorana fermions with T junctions and each Majorana can be moved independently to swap positions with nearby Majoranas as shown in Fig.2.3,

Let us suppose that the exchange process happens within a time T. It can be described by a time-dependent Hamiltonian $H(t)$. Since the final configuration of the system is identical to the initial one, i.e. the final system has the same topological phase boundaries as the initial system, we should have $H(t) = H(0)$, i.e. the exchange process brings the system back to the initial condition. And to ensure the system will not leave the degenerate ground state, the process should be slow enough to obey the adiabatic theorem. With the adiabatic condition, we can use a unitary operator U to connect the initial and final quantum states, such that

$$|\Psi_f\rangle \to U\,|\Psi_i\rangle \tag{2.32}$$

where $|\Psi_f\rangle$ is the final state and $|\Psi_i\rangle$ is the initial state. Because the ground states of N pair of Majoranas are 2^N fold degenerate, the operator U should be a $2^N \times 2^N$ unitary matrix. It is worth noting that the total particle number cannot be changed due to an adiabatic process, so U must commute with the total parity operator. Since U should only depend on the two Majoranas exchanged in process and the process needs to preserve the fermion parity, it can be shown U has the form [18]

$$U = \exp\left(\pm\frac{\pi}{4}\gamma_n\gamma_m\right) = \frac{1}{\sqrt{2}}\left(1 \pm \gamma_n\gamma_m\right) \tag{2.33}$$

The sign in the Eq.2.33 depends on how we choose the exchange direction. In the following discussion, we assume the exchange always happens in a counter-clockwise manner and pick the + sign. This exchange process of two Majoranas is just the braiding operation we introduced before:

$$B = U = \frac{1}{\sqrt{2}}\left(1 + \gamma_n\gamma_m\right) \tag{2.34}$$

In a closed system with only one pair of Majoranas, braid operator can only multiply the fermion number states $|0\rangle, |1\rangle$ by a phase factor:

$$B_{12}|0\rangle = \frac{1}{\sqrt{2}}(1+i)|0\rangle \tag{2.35}$$

$$B_{12}|1\rangle = \frac{1}{\sqrt{2}}(1-i)|1\rangle \tag{2.36}$$

We see the braiding process only introduces a phase factor to the initial state. That is because the parity is fixed for a closed system, the braiding process cannot change the initial state to a new state with different parity, e.g from $|0\rangle$ to $|1\rangle$.

To have a nontrivial effect from the braid operator, we need to have at least two pairs of Majoranas. The system with two pairs of Majoranas has four degenerate ground states:

$$|00\rangle, |11\rangle, |01\rangle, |10\rangle \tag{2.37}$$

where $|00\rangle$, $|11\rangle$ possess even parity and $|01\rangle$, $|10\rangle$ have odd parity.

The corresponding wavefunction has the general form:

$$|\Psi\rangle = s_{00}|00\rangle + s_{11}|11\rangle + s_{01}|01\rangle + s_{10}|10\rangle \tag{2.38}$$

which can also be presented as $|\Psi\rangle = (s_{00}, s_{11}, s_{01}, s_{10})^T$. Now the braiding operator can be computed explicitly using Eq.2.34, and we have

$$U_{12} = \exp\left(\frac{\pi}{4}\gamma_1\gamma_2\right) \equiv \begin{pmatrix} e^{-i\pi/4} & 0 & 0 & 0 \\ 0 & e^{i\pi/4} & 0 & 0 \\ 0 & 0 & e^{-i\pi/4} & 0 \\ 0 & 0 & 0 & e^{i\pi/4} \end{pmatrix} \tag{2.39}$$

$$U_{23} = \exp\left(\frac{\pi}{4}\gamma_2\gamma_3\right) \equiv \frac{1}{\sqrt{2}} \begin{pmatrix} 1 & -i & 0 & 0 \\ -i & 1 & 0 & 0 \\ 0 & 0 & 1 & -i \\ 0 & 0 & -i & 1 \end{pmatrix} \tag{2.40}$$

$$U_{34} = \exp\left(\frac{\pi}{4}\gamma_3\gamma_4\right) \equiv \begin{pmatrix} e^{-i\pi/4} & 0 & 0 & 0 \\ 0 & e^{i\pi/4} & 0 & 0 \\ 0 & 0 & e^{i\pi/4} & 0 \\ 0 & 0 & 0 & e^{-i\pi/4} \end{pmatrix} \tag{2.41}$$

Apply those operators to the state $|00\rangle$, we have

$$B_{12}|00\rangle = \frac{1}{\sqrt{2}}(1+i)|00\rangle \tag{2.42}$$

$$B_{23}|00\rangle = \frac{1}{\sqrt{2}}(|00\rangle + i|11\rangle \tag{2.43}$$

$$B_{34}|00\rangle = \frac{1}{\sqrt{2}}(1+i)|00\rangle \tag{2.44}$$

We can see after exchange Majorana 2 and 3, the initial state $|00\rangle$ turns into a new state, which is a superposition of $|00\rangle + i|11\rangle$. That shows the non-Abelian nature of Majorana fermions: apart from adding a phase factor, it actually changes the initial state to a new superposition state. The nontrivial braiding process is illustrated in Fig.2.3. More generally, braid operators commute with each other when no single Majorana involved in both operators, such that: $[B_{12}, B_{34}] = 0$. That is reasonable because the exchange of a pair of Majorana fermions should be independent of whether another pair of Majorana fermions have been exchanged. However, when the a single Majorana is involved in both exchange, then the two exchanges no longer commute, i.e. $[B_{n-1,n}, B_{n,n+1}] = \gamma_{n-1}\gamma_{n+1}$. Overall, the form of the braid operator $B_{n,n+1}$ contains information about the exchange process. Only when $B_{n,n+1}$ is non-diagonal, the particle follows non-Abelian statistics.

In the previous discussion, we see a system with N pairs of well-separated Majoranas has 2^N fold ground state degeneracy. However, as soon as the overlap between Majorana zero modes present, a term with the form [18] of

$$\frac{i}{2}t\gamma_{2n-1}\gamma_{2n} = t\left(\hat{\mathcal{N}}_n - \frac{1}{2}\right) \tag{2.45}$$

appears in the new Hamiltonian, where t describes the coupling strength and $\hat{\mathcal{N}}$ is the fermionic number operator (2.12). With this new term, the ground state is no longer degenerate. As the result, a finite energy is required to occupy the corresponding fermionic state when $t > 0$. While Majorana coupling causes trouble for Braiding operation as it requires degenerate ground states, it can be useful in determining the parity of the system. That can be done by inducing overlap between two Majorana fermions and then measure the corresponding energy [6]. That process is formally called fusion.

2.3.2 Majorana Based Topological Quantum Computation

Because of the non-Abelian statistic nature of Majorana fermions, Majoranas can be used to build a robust quantum computer. More detailed discussion can be found in [7, 6, 15]. Here we just introduce some basic concept of Majorana based quantum computation.

Quantum computation harness quantum phenomena to process information. Similar to classical computation uses bits to encode information, Quantum computation encode information in quantum bits (qubits). Generally, a qubit can be constructed on a two-level quantum system. For instance, spin up and spin down states of individual electrons can be used to build a spin qubit. While a classical bit can only be in one of the two states, a qubit can posses a superposition of the two states due to its quantum origin. With a large number of entangled qubits, quantum algorithms can then take advantage of quantum superposition and entanglement to outperform classical algorithms in certain difficult tasks.

As we discussed in the previous sections, although a pair of non-overlap Majorana fermions can give two generate ground states, these two states cannot be changed by braiding process due to fixed parity. To have a two-level system that can be used as a qubit, we need a minima of two pairs of Majoranas fermions. With four Majorana zero modes, a qubit can then be defined using the two degenerate states with same parity.

Here we only consider the two even states: $|00\rangle$ and $|11\rangle$. We can the define $|00\rangle$ as $|\hat{0}\rangle$ and $|11\rangle$ as $|\hat{1}\rangle$ for the qubit states.

In this qubit basis $\{\hat{0}, \hat{1}\}$, Pauli matrices can be expressed with Majorana operators,

$$-i\gamma_1\gamma_2 = \sigma_z \quad -i\gamma_3\gamma_4 = \sigma_z \tag{2.46}$$

$$-i\gamma_2\gamma_3 = \sigma_x \tag{2.47}$$

$$-i\gamma_1\gamma_3 = \sigma_y \quad -i\gamma_2\gamma_4 = \sigma_y \tag{2.48}$$

We can then set $|0\rangle$ as the north pole of the Bloch sphere and $|1\rangle$ to be the south pole, then braid operations can only rotate a single qubit by an angle of $\pi/2$ as

$$B_{12} = B_{34} = e^{-\frac{i\pi}{4}\sigma_z} \tag{2.49}$$

$$B_{23} = e^{-\frac{i\pi}{4}\sigma_x} \tag{2.50}$$

Algorithms can be executed with different sequences of braiding process. However, since the rotation introduced by braiding is fixed for a certain angle, braiding itself cannot satisfy the requirement of universal quantum computation, where arbitrary rotation is required. To realized universal quantum computation, non-protected operations must be included [6, 7]. A schemes to compensate the non-universality of Majorana braiding is to combine Majorana qubits with conventional qubits [25]. Although braiding operations have limits on manipulating qubit states, Majorana qubits have a big advantage comparing to other 'conventional' qubits. Since the information of the qubit is encoded in well-separated Majorana zero modes, local perturbations cannot change the qubit states. Thus Majorana qubit is predicted to have good performance against decoherence [21].

Another big advantage of Majorana qubits is the algorithm accuracy. Since each braiding process rotates the qubit state by an exact angle, algorithm as a sequence of braiding processes also give an exact result. In the adiabatic limit, this operator is independent of the braiding trajectory and timing. Consequently, the final result is supposed to be very accurate and reliable.

While Majorana qubits are immune to local perturbations, they can still be the victim of decoherence when the fermion parity of the state is changed due to the tunneling of an extra quasiparticle. That harmful quasiparticle tunneling process is often referred as 'quasiparticle poisoning'. In real experimental systems, one possible cause of quasiparticle poisoning is the

so-called 'soft' gap problem. Due to the presence of disorder, interface inhomogeneity, finite temperature and dissipation [26] in experimental systems, the actual topological energy gap is often soft, meaning a gap with non-zero subgap density of states, comparing to the ideal gap, which has absolute zero density of states within the gap and is often referred as the 'hard' gap. The fermionic states within the soft energy gap could hybridize with Majorana zero modes and induce quasiparticle poisoning [15]. While poisoning set a upper limit to the coherence time of Majorana qubits, recent works have already shown various methods to greatly suppress quasiparticle poisoning [27]. Another challenge for realizing Majorana qubits in 1D system is probably the finite system size. As Majorana modes will overlap when the separation between Majorana modes is smaller than the Majorana coherence length, which leads to the loss of topological protection, the size of the topological region needs to be larger than the Majorana coherence length. Development in materials could possibly increase the separation of Majorana modes as well as improve the topological energy gap, eventually leading to the realization of Majorana qubits.

2.4 Majorana Zero Modes in One Dimensional Semiconductors

For the Majorana-like quasiparticles in 1D systems, people often refer them as Majorana Modes. In the following discussion, we will use Majorana zero modes (MZMs) to refer to localized, zero-energy edge states. First, we write the Kitaev chain Hamiltonian in momentum space using Bogoliubov-de Gennes formalism:

$$H_{\text{Kitaev}} = (-2t\cos k_x - \mu)\,\tau_z + 2\Delta\tau_y \sin k_x \tag{2.51}$$

Here, we assume the main axis of the 1D wire and the momentum k are both in the x direction. τ_i are the Pauli matrices acting on particle hole space. μ, t and Δ are the chemical potential, inter-site hopping and the superconductivity respectively. As we saw before, $|\mu| < 2t$ corresponding to a topologically nontrivial phase with Majorana bound states appearing at the boundaries of the topological region. Since we want to have a tunable chemical potential μ, semiconductor system with low electron density is preferable.

On the contrary, the electron density is too high to be tuned in a superconductor. It will be convenient to re-define the chemical potential regarding the bottom of the band:

$$\mu \to \mu - 2t \tag{2.52}$$

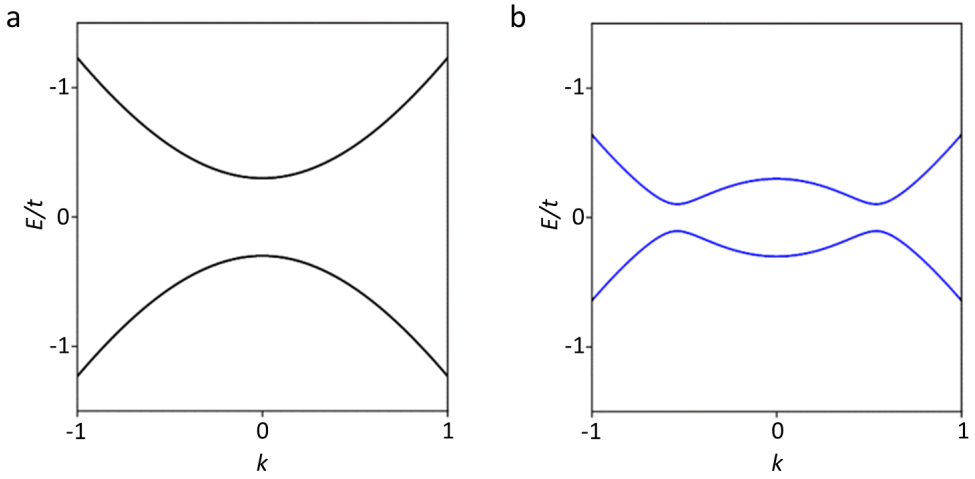

Figure 2.4: **Band structure of a Kitaev chain.a**, For a Kitaev chain with $\Delta \ll t$ and $\mu \ll 2t$. $\mu > 0$ corresponding to the topologically trivial phase. **b**, the system is nontrivial and harbors Majorana bound states when $\mu < 0$.

The transition point between trivial and non-trivial states shifts to $\mu = 0$ and $\mu < 0$ corresponds to the non-trivial phase. In a semiconductor system, superconductivity can be induced by proximity effect. Generally, the proximity effect happens when a normal-type conductor is brought in contact with a superconductor. Consequently, superconducting order can leak into the normal conductor through the interface and induce pairing correlations together with an induced superconducting gap. The strength of the induced superconductivity depends on the superconductivity in the parent superconductor, the interface transparency as well as the electronic band structure of the normal conductor. We assume the superconducting pairing Δ is uniform here inside the system. Proximity-induced superconductivity is weak compared to the kinetic energy, so we have $\Delta \ll t$. And μ can be tuned to be

small compared to the bandwidth, so $\mu \ll 2t$. With these two conditions, Kitaev chain Hamiltonian can be modified by expanding the $\cos k$k term and take the continuum limit:

$$H_{Kitaev} = \left(\frac{k_x^2}{2m} - \mu\right)\tau_z + 2\Delta\tau_y k_x \tag{2.53}$$

Here m represents the effective electron mass and is also used as the coefficient of the expansion.

Now we have a controllable system with the band structure shown in Fig. 2.4. For $\mu < 0$, we have the topologically nontrivial phase with zero energy Majorana bound states.

Another obvious problem for Kitaev chain is that it works with some hypothetical spinless fermions and therefore each site can only be occupied by one fermion. Such spinless fermion does not exist in nature and we still need to add spin to realize the model in experiments.

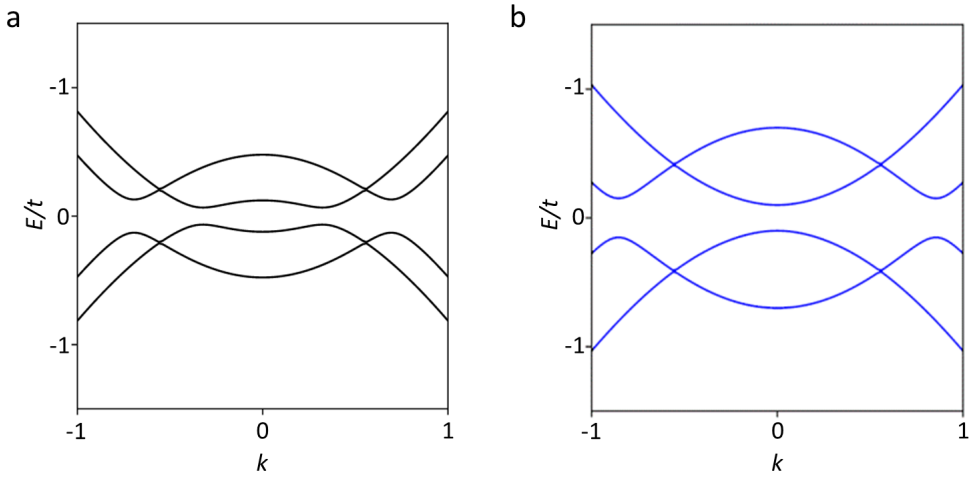

Figure 2.5: **Band structure of one dimensional system with spin and Zeeman field.a**, After introduced spin and Zeeman field to the Kitaev model, the system is topologically trivial when $\mu > E_z$. **b**, With $\mu < E_z$, the system is nontrivial with Majorana bound states.

After introducing spin degeneracy into the system, the band structure keeps the same and we still have zero energy states at the end of the chain. However, due to the extra degeneracy introduced by spin, each state is now two-fold degenerate. As the consequence,

two Majoranas now appear at one edge site, which just equals to a regular fermion with zero energy. To remove the extra degeneracy from spin, it is intuitive to add a Zeeman field. Then the Hamiltonian takes a Zeeman term and reads:

$$H = \left(\frac{k_x^2}{2m} - \mu - E_z\sigma_x\right)\tau_z + 2\Delta\tau_y k_x \tag{2.54}$$

where $E_z = \frac{1}{2}g\mu_B B$ is the Zeeman energy. The Zeeman field is chosen to be parallel to the momentum to break the spin degeneracy.

With the Zeeman term, we can make one spin species trivial by setting $\mu - E_z > 0$ and the other spin species non-trivial by setting $\mu - E_z < 0$. The new topological condition is $\mu < E_z$. Single MZM appears at the end of the chain whenever the topological condition is satisfied. The band structures for $E_z < \mu$ and $E_z > \mu$ are shown in Fig. 2.5. Apart from remove the spin degeneracy, Zeeman splitting also opens the topological gap at k = 0, which has importance since it determines the thermal protection of MZMs and the accessibility of MZMs in the experiment. Actually, the size of that gap in 1D semiconductor system is a big advantage over other systems [7]. More details about that gap can be found in [28].

The last difficulty we have in Kitaev chain is its special superconductivity. It pairs electrons from neighboring sites. In momentum space, that means the superconducting pairing is proportional to Δk. Only P-wave superconductivity has a such form of pairing. While p-wave pairing is predicted to exist for decades and some experiment evidence suggests p-wave superconductivity in S_2RuO_4 [29] and iron based superconductors [30], so far it is still hard to reach in a 1D system.

The solution is to still use conventional s-wave superconductor. The the Bardeen-Cooper-Schrieffer (BCS) theory explaining the conventional superconductivity can be found in [22]. Since s-wave pairing is singlet:

$$H_{\text{pair}} = \Delta\left(c_\uparrow c_\downarrow - c_\downarrow c_\uparrow\right) + h.c. \tag{2.55}$$

With s-wave superconductivity, the Hamiltonian reads:

$$H = \left(\frac{k_x^2}{2m} - \mu - E_z\sigma_x\right)\tau_z + \Delta\tau_x \tag{2.56}$$

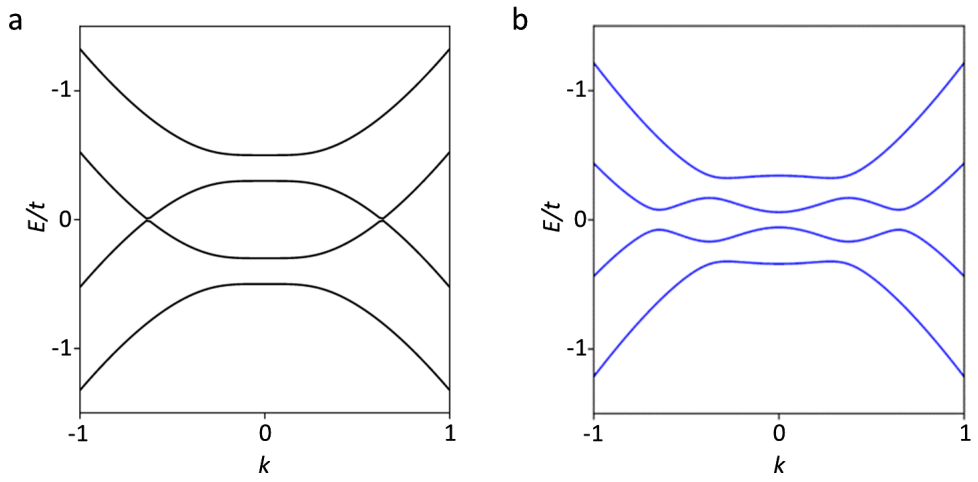

Figure 2.6: **Band structure of one dimensional system with s-wave superconductivity.a**, After switch to s-wave superconductivity, the system is topologically trivial when there is no spin-orbit field. **b**, With finite spin orbit field perpendicular to the Zeeman field, the system is nontrivial when $E_z^2 > \Delta^2 + \mu^2$.

The new problem now is that since the superconducting pairing has no more momentum dependence and only σ_x appears in the Hamiltonian, spin conservation prevents the appearance of Majorana bound states in the system. This can also be seen from the band structure as shown in Fig. 2.6(a), without momentum dependence in the pairing, the gap is always closed at finite k when $E_z > \Delta$.

To open the gap at finite k, we need a term in Hamiltonian that depends on momentum and also couples to spin differently than the Zeeman term.

Spin-orbit interaction (SOI) is a good choice. The SOI in 1D system can be expressed by the Rasba SOI Hamiltonian:

$$H_{SO} = -\alpha_{so}\sigma_y k_x \tag{2.57}$$

where α_{so} is the spin-orbit strength that incorporates the electric field. The spin-orbit interaction needs to have some component that is perpendicular to the Zeeman field to

break degeneracy at finite k (Fig. 2.6(b)).

In the simplest case. We just choose the spin-orbit field to be orthogonal to the Zeeman field, which is in x direction. The final Hamiltonian is:

$$H_{BdG} = \left(\frac{k_x^2}{2m} - \mu - \alpha_{so}\sigma_y k_x - E_z\sigma_x \right) \tau_z + \Delta\tau_x \tag{2.58}$$

In the Bogoliubov-de Gennes matrix formalism, it has the form:

$$H_{\mathrm{BdG}} = \begin{bmatrix} H_0 & \Delta \\ \Delta^\dagger & -\mathcal{T}H_0\mathcal{T}^{-1} \end{bmatrix} \tag{2.59}$$

Where

$$H_0 = \begin{bmatrix} \frac{k_x^2}{2m} - \mu & E_z + i\alpha_{so}k_x \\ E_z - i\alpha_{so}k_x & \frac{k_x^2}{2m} - \mu \end{bmatrix} \tag{2.60}$$

$$\Delta = \begin{bmatrix} 0 & \Delta \\ -\Delta & 0 \end{bmatrix} \tag{2.61}$$

and $\mathcal{T}$ is the time reversal operator.

Since a finite spin orbit field orthogonal to the Zeeman field always open the gap at finite k for constant Δ and μ, the topological phase condition is purely decided by the energy spectrum at $k = 0$. By having $k = 0$ in Eq.2.59, topologically nontrivial phase and Majorana bound states emerge when

$$E_z^2 > \Delta^2 + \mu^2 \tag{2.62}$$

while $E_z^2 < \Delta^2 + \mu^2$ corresponding to trivial phase and the topological phase transition happens when $E_z^2 = \Delta^2 + \mu^2$.

It is worth noting that while spin-orbit interaction also has spin dependence, it can not replace Zeeman field. That can be seen by considering the energy spectrum at $k = 0$. Without Zeeman field, zero energy is always doubly degenerate.

That can also be understood by noticing spin-orbit interaction does not break time-reversal symmetry. And Kramers theorem states that half-integer spin states is at least doubly degenerate under time-reversal symmetry. In experiments, the direction of the spin-orbit field might be unknown due the presence of complicated local electric fields from

superconductor and local gates. It is thus more convenient to control the direction of the magnetic field. More details about the magnetic field direction are discussed in next section.

It is also good to know that while the spin-orbit interaction does not determine the topological phase condition, the topological gap at finite k does depend on the spin-orbit interaction. Generally, the topological gap has a non-monotonous dependence on both spin-orbit coupling and Zeeman field due to the complicated band structure, e.g. the band has several local minima at different k.

That topological gap is important since it separates Majorana zero energy states from the first excited fermion state and thus determine the topological protection of the Majorana zero energy states.

To sum up, we have modified Kitaev model to a more realistic model and shown following ingredients are required to realize Majorana bound states in a 1D system:

1. One dimensional semiconductor system with controllable chemical potential.
2. Superconductivity induced by proximity effect, which introduces particle-hole symmetry into the system.
3. The spin-orbit interaction, which breaks spin conservation and open a gap at finite k.
4. The Zeeman field, which breaks the time reversal symmetry and opens a gap at $k = 0$.

2.4.1 Majorana Zero Modes in Quasi-1D Nanowires

While we already have a modified Hamiltonian that describes real physics phenomena and supports Majorana bound states in section 2.4, the conditions and requirements are still assumed ideal there. Here, to realize Majorana bound states in experiments, we need to work with a non-ideal system, i.e. a quasi-1D semiconductor nanowire with finite length. In this section, we will discuss the effect due to those non-ideal conditions and how to tune the experimental parameters.

In the previous section, we see in a 1D semiconductor system coupled to a conventional s-wave superconductor, topological phase emerges when Zeeman field exceeds the critical field

$$E_c = \sqrt{\Delta^2 + \mu^2} \tag{2.63}$$

Consequently, the superconducting phase is topologically nontrivial only when $E_z > E_c$. The lowest E_c is achieved when $\mu = 0$.

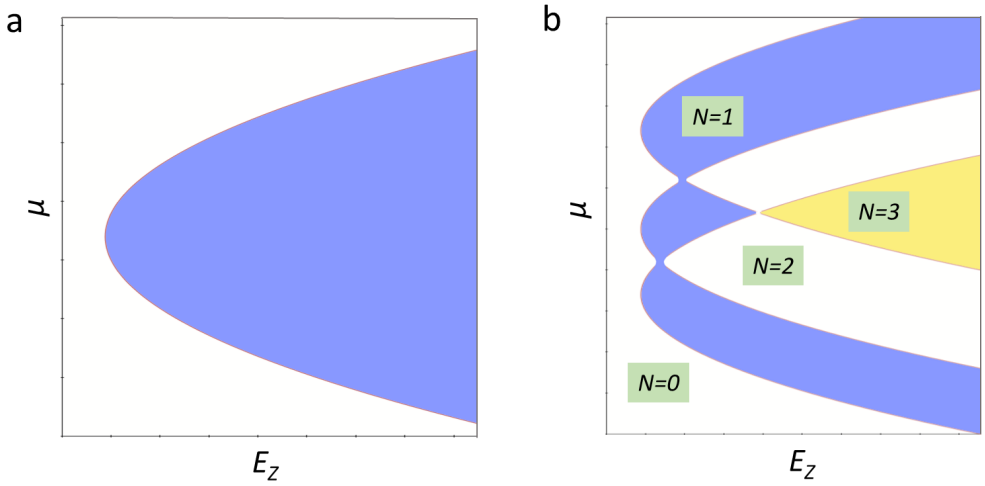

Figure 2.7: **Topological phase diagrams in one dimensional wire.** **a**, Topological phase diagram for single band occupation. The topological phase (blue region) first emerges at $\mu = 0$. **b**, Topological phase diagram for multiband occupancy. The topological phase is indicated by low–energy modes number N. For N odd, the system is nontrivial (blue and yellow regions).

For the superconductivity, it can be induced by proximity effect as we mentioned before. The induced gap Δ is determined by the parent superconductor, the semiconductor superconductor interface and the semiconductor band structure and it is safe to treat it as a fixed quantity if there is only one band. When the two parameters we can control is the chemical potential and Zeeman energy. As determined by Eq.2.62, the topological phase has a parabola shape in Zeeman energy and chemical potential space as shown in the topological phase diagram Fig. 2.7(a).

For the controlling of chemical potential, electrostatic coupled local gates can do the work. And the Zeeman energy can be induced by applying a magnetic field. Note the magnetic field needs to have some component orthogonal to the spin-orbit field as shown before. While the direction of the spin-orbit field might be hard to measure, it should be perpendicular to the nanowire main axis since the momentum is along the nanowire and

spin-orbit coupling is the vector product of momentum and spin. Then it is safe to have the magnetic field in parallel with the nanowire to induce the necessary Zeeman energy. More generally, for a fixed magnitude field magnitude, tilting the magnetic field to increase the non-orthogonal component regarding the spin-orbit can destroy the topological phase [31]. The specific value of the non-orthogonal component depends on E_z, Δ and spin-orbit strength of the system.

In the previous discussion, we assume the semiconductor wire is strictly one-dimensional so that there is only one band. However, it is challenging to have strict 1D system [32] and in practice we need to deal with quasi-1D condition, i.e. nanowires with finite diameters, under multiband occupancy.

In a quasi-1D system, if the the subband energy spacing is much larger than the induced Zeeman energy, the previous picture still apply, except that μ has to be re-defined regarding the top–most occupied subband, i.e. $\mu = 0$ at the bottom of the top-most subband. However, if the induced Zeeman energy reaches the same order of magnitude of the subband spacing, then the change is nontrivial [20].

In principle, with multiband occupancy, the system can enter topologically trivial and non-trivial phase alternatively upon increasing Zeeman energy at a fixed μ. The topological phase transition is manifested by the closing of the bulk energy gap as well as the varying of low–energy modes number N at each end of the wire [33]. For N odd, the system is non-trivial hosting Majorana bound states. While for N even, the system has a trivial phase and end modes with finite energy. Moreover, the multiband topological phase diagram (Fig. 2.7(b)) shows each subband supports a topological phase and at some critical points nearby topologically nontrivial phases meet together. The phase diagram may also be affected by the induced superconductivity [33] and orbital effect of the magnetic field [34].

Another non-ideal condition we need to consider is that a wire cannot be infinitely long. In experiment, we always have wires with finite lengths and thus a finite superconducting nanowire section. As the result, the two Majorana bound states couples to each other and hybridize into Bogoliubov quasiparticle with non-zero energy. Due to that coupling, the energy of the two Majorana bound states split symmetrically regarding zero energy. As

shown in [35], the Majorana wavefunction shows an exponential tail:

$$\Psi_l(x) \propto e^{-x/\xi} e^{\pm i k_{F,eff} x} \tag{2.64}$$

With $k_{F,eff}$ the effective fermi wavevector for the top-occupied subband, x the distance from the wavefunction center, i.e. wavefunction amplitude maximal, and ξ the effective superconducting coherence length. This relation is valid as long as $x \gg \xi$, i.e. only the tails of the wavefunctions overlap. The energy splitting can also be approximately expressed as [35]:

$$\Delta E \approx \hbar^2 k_{F,eff} \frac{e^{-2L/\xi}}{m\xi} \cos\left(k_{F,eff} L\right) \tag{2.65}$$

Where L is the distance measured between the center of the two Majorana wavefunctions and m is the effective electron mass in the wire. As long as $L \gg \xi$, the energy spitting increases with a decreasing wire length and decreases with decreasing coherence length. Due to the cosine dependence in Eq.2.65, the energy oscillates with varying $k_{F,eff}$. Since the applied magnetic field can increase the coherence length by increasing the effective Fermi-velocity and suppressing the superconductivity and $k_{F,eff}$ depends on chemical potential, the oscillatory energy is supposed to be controllable with varying chemical potential and magnetic field in experiments.

We notice in the short wire limit, Majorana bound states become meaningless as they are now strongly coupled to each other and behave like a Dirac fermion. Near-zero-energy states, however, may still emerge for a wire length close to the superconductor coherence length [36]. Those near-zero-energy states are considered as the remnant of the long-wire topological phase. In a short wire, continuous energy spectrum within a subband turns into discrete energy levels, resulting in a more complicated topological phase diagram in chemical potential and magnetic field space [36].

2.5 Detection of Majorana Zero Modes in 1D Nanowires

For the 1D system we discussed above, Majorana bound states emerge with one at each end of the wire when the topological phase condition is reached. As the next step, signatures need to be obtained to prove the existence of Majorana bound states. Since Majorana bound states have zero charge and zero effective spin, detecting them is a challenging task. Based on theoretical proposals and current experiment conditions, two methods are mostly used: detecting the Majorana induced zero-bias conductance peaks (ZBCPs) in tunneling spectroscopy and measuring the 4π-Josephson current in a Josephson junction. The latter one, which relies on the observation of Majorana modified Josephson current-phase relationship, is less relevant to this thesis.

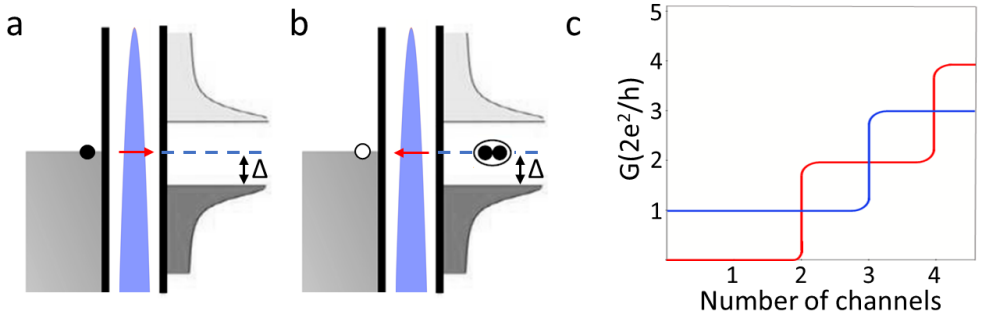

Figure 2.8: **Tunnel process through Majorana bound states and Majorana conductance quantization. a and b**, Illustration of the resonant Andreev reflection process due to the presence of Majorana bound states. **c**, Zero-bias conductance map at finite magnetic field with quantum point contact as the tunnel probe. With Majorana bound states (blue curve), the first plateau is quantized at $2e^2/h$ and the subsequent plateaus are at half-integer multiples of $4e^2/h$. For trivial case, all the plateaus are quantized at integer multiples of $4e^2/h$. This schematic plot is based on [1].

The main method we used to detect Majorana signal is searching the so-called ZBCPs in tunneling measurements. With a normal metal lead connected to one end of the wire and a tunnel barrier placed between the normal lead and the topological region, electrons

can tunnel into the topological region through resonant Andreev reflection. As shown in Fig. 2.10(a). Andreev reflection happens when an electron (hole) at energies less than the superconducting gap enters a superconductor from a normal state material. A hole (electron), which has opposite spin and velocity to the incident electron (hole), is reflected as the incident electron (hole) creates (eliminates) a Cooper pair in the superconductor. The tunnel process through Majorana bound states is depicted in Fig. 2.8(a)(b). Here the Andreev reflection is resonant, i.e. with unit probability, since the incident electron and the reflected hole tunnel through the same barrier and share the same normal lead, i.e. the lead serves as both the electron lead and the hole lead. As Majorana is equal superposition of electrons and holes, it couples to 'both' leads equally, and thus leads to a resonant tunneling similar to the resonant tunneling through a double barrier junction with equal barriers. Since Majorana bound states have zero energy, the resonant Andreev reflection results in a conductance resonance at zero bias. With each incident electron transports a Cooper pair into the superconductor, which serves as the other tunnel lead, the conductance of the ZBCP is supposed to be quantized at $2e^2/h$.

The resonant Andreev reflection can also be seen by calculating the scattering matrix of the tunnel process. The scattering matrix can be presented using the probabilities of normal reflections (r_{ee} for electrons and r_{hh} for holes) and the probabilities of Andreev reflection (r_{eh} for electron and r_{he} for holes) as

$$\boldsymbol{r} = \begin{bmatrix} r_{\mathrm{ee}} & r_{\mathrm{he}} \\ r_{\mathrm{eh}} & r_{\mathrm{hh}} \end{bmatrix} \tag{2.66}$$

The conductance caused by tunneling into the superconductor is related to the scattering matrix by [37]:

$$G = \frac{2e^2}{h} \operatorname{Tr}\left(rr^{\dagger}\right) \tag{2.67}$$

Considering the scattering matrix is unitary and the requirement of particle-hole symmetry at zero energy, we have

$$r_{\mathrm{ee}} r_{\mathrm{eh}}^{*} + r_{\mathrm{he}} r_{\mathrm{hh}}^{*} = 0 \tag{2.68}$$

Which implies $r_{he} = 1$ or 0. Since the probabilities of Andreev reflection cannot be zero due to the presence of Majorana bound states, we must have $r_{he} = 1$ with $\det(r) = -1$. As

the result, $G = \frac{2e^2}{h}$ as given by Eq.2.67, i.e. the tunneling is resonant regardless the barrier strength.

The behavior of the Majorana induced resonant Andreev reflection is in sharp contrast to the normal Andreev reflection in a metal- superconductor junction, in which the amplitude decreases with decreasing coupling strength. Moreover, when a quantum point contact (QPC) is used as the tunnel probe, the resonant Andreev reflection can modify the conductance quantization plateaus at zero bias as shown in Fig. 2.8(c). The first plateau is quantized at $2e^2/h$ with the presence of Majorana bound states (blue curve) instead of $4e^2/h$ for the topologically trivial case. Even with disorder, the first $2e^2/h$ due to Majorana induced resonant Andreev reflection always persist, while all the other plateaus for both topologically trivial and non-trivial cases may disappear[1].

For the discussion above, we assume ideal conditions, i.e. zero temperature and an infinite long topological region. The quantized ZBCP may still be accessible for finite temperature and finite size system when tunnel coupling dominates over both temperature and Majorana splitting[1].

It is worth noting the method we discussed above, i.e. searching a $2e^2/h$ ZBCP at finite field in local tunnel measurement, may not unambiguously prove the existence of Majorana bound states. Recent development of theories and experiments show topologically trivial states can also produce ZBCPs at finite field even with conductance close to $2e^2/h$ [38, 39, 40].

As the solution, three-terminal measurement with one more normal lead added to the other side of the topological region might be a more powerful method to study Majorana signal. As Majoranas should always emerge in pairs with one at each end of the topological region, correlated ZBCPs should be observed at the two ends. Moreover, observation of a splitting of the ZBCP simultaneously at the two ends may serve as the smoking gun evidence of the existence of Majorana bound stats [35]. In the end, we emphasize the observation of the non-Abelian exchange statistics, which inevitably requires braiding of Majorana bound states, can unambiguously prove the existence Majorana bound states.

2.6 Andreev Bound States in 1D System

In the area of MZMs in 1D systems, one highly related concept is Andreev bound states (ABSs). On one hand, they are distinct from MZMs as topologically trivial states, while they can also emerge in topologically non-trivial regime. On the other hand, ABSs signal shares many similarities with the signal of MZMs [41, 42, 43, 40, 38], e.g. generating pinning ZBCPs at finite magnetic fields. In fact, a pair of overlapping MZMs can form a ABS or a partially-separated Andreev bound state (ps-ABS) depending on the degree of Majorana overlapping [43]. How to experimentally distinguish MZMs from ABSs is thus a non-trivial problems involving a lot of interest and effort. In this section, we introduce the general origin and properties of ABSs in 1D system.

In the simplest but also experimental related system, where a single quantum dot (QD) coupled to a superconducting lead and a normal lead. Due to proximity effect, superconducting order can be induced inside the dot and the Hamiltonian can be described by a single spin-degenerate level coupled to a superconducting reservoir:

$$H = H_{\mathrm{S}} + H_{\mathrm{N}} + H_{\mathrm{QD}} + H_{\mathrm{t}} \tag{2.69}$$

Where H_{QD} represents the QD, H_t defines the coupling between the QD and the coupled superconductor and H_S, H_N are the superconducting lead and normal lead respectively. There are two important effects here: Coulomb interaction in the QD and superconductivity. First we consider two extreme cases: (I) when Coulomb interaction is dominating over the superconductivity, the system is close to a normal QD with charging energy E_c. (II) when coupling between the QD and superconductor is strong so that the induced superconductivity is much stronger than the charging effect, the quantum dot becomes a part of the superconductor, which favors of electron pairing. In a more general case, Coulomb interaction competes with the induced superconductivity. Since superconductivity pairs opposite spins and favors even number of electrons while Coulomb interaction tends to fill electrons one by one, the ground states of the system is either a spin singlet $|S\rangle$ or a spin doublet $|D\rangle$ depending on different scales of energies. The relevant energies here are: Δ, the induced superconducting gap in the QD, E_c, the charging energy, Γs, QD-superconductor tunnel

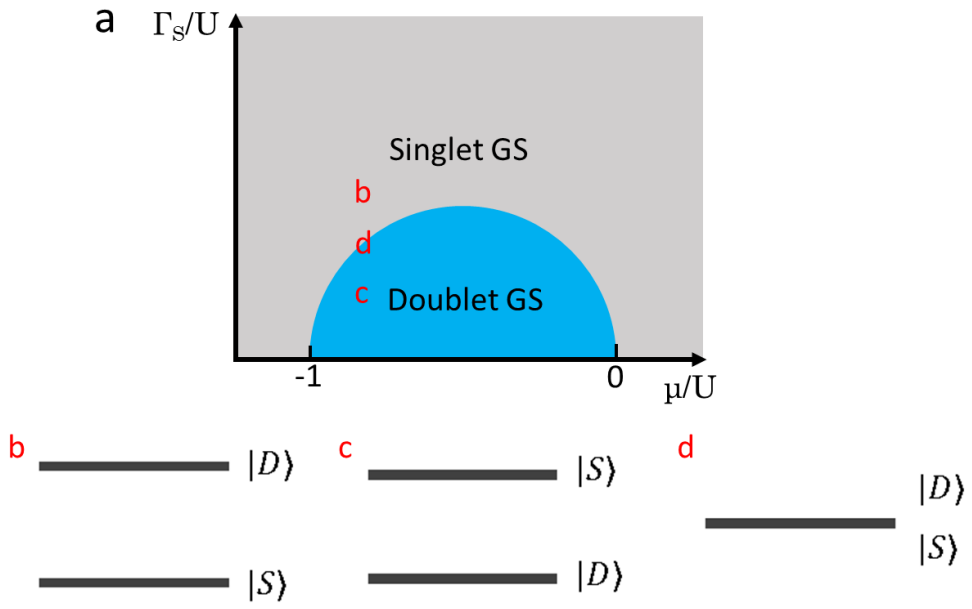

Figure 2.9: **Phase diagram of a two-level quantum dot coupled to a superconductor.** The ground state of the QD system can be altered by varying chemical potential and QD-superconductor coupling. In side the spin singlet ground state phase (grey region), the ground state is a spin singlet and the excited state is a spin doublet. At he phase boundary, two spin states are degenerate. For weak QD-superconductor coupling, the ground state is a spin doublet when the system has odd parity.

coupling, and chemical potential μ of the QD relative to the Fermi level of the superconductor. When E_c is much larger Δ, i.e. it is a small QD, a qualitative phase diagram of the two spin states are shown in Fig. 2.9(a). When the QD-superconductor coupling $\Gamma s = 0$ (along the horizontal axis in Fig. 2.9(a)), the ground state is a doublet for odd occupation and the ground state is a singlet for even occupation. As Γs increases, the phase of doublet ground state shrinks in chemical potential space since now the enhanced induced superconductivity favors electron pairing. With further increased Γs, eventually singlet becomes the ground state for the entire μ/U range. It should be noted that at the boundary

of the two phases, singlet and doublet are degenerate. Transitions between the ground state and the excited state lead to discrete energy levels $\pm|\zeta|$, which are the eigenstates of the QD-superconductor system. Andreev bound states can form in that system due to Andreev reflection(Fig. 2.10(a)).

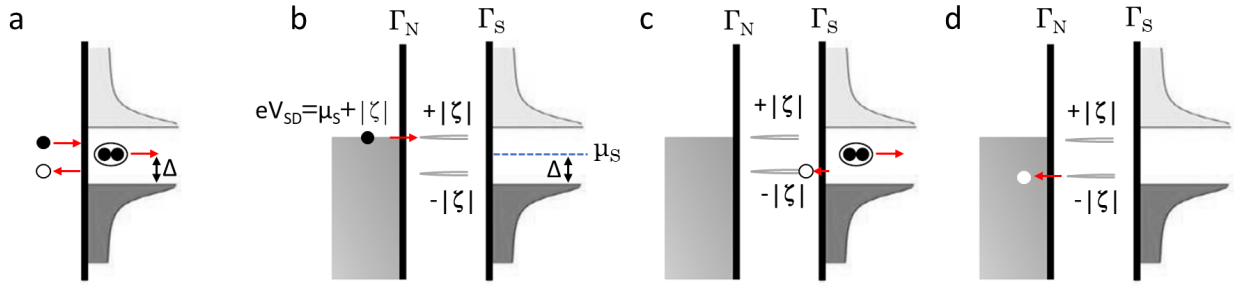

Figure 2.10: **Andreev bound states induced transport.** **a**, Schematics of Andreev reflection. **b-d**, Transport cycle through Andreev bound states.

Experimentally, Andreev bound states can give rise to conductance resonances in electron transport. The general transport cycle is illustrated in Fig. 2.10. When the chemical potential of the normal lead aligns with the transition energy $+|\zeta|$, an electron can tunnel into the energy level $+|\zeta|$. This electron induces an Andreev reflection on the interface between the QD and the superconducting lead. As the result, a Cooper pair is generated inside the superconductor while a hole is reflected into the QD with energy $-|\zeta|$. In the end, the hole tunnel into the normal lead and the system returns to the ground state with two electrons transport into the superconductor and $2|\zeta|$ energy dissipated. Similar, when the chemical potential of the normal lead aligns with the transition energy $-|\zeta|$, a transport cycle that eliminates a Cooper pair can happen.

As indicated by the phase diagram(Fig. 2.9(a)), the transport resonance $\pm|\zeta|$ can be tuned by varying chemical potential as well as the QD-superconductor coupling. In Fig. 2.11, we illustrate the tuning of $\pm|\zeta|$. In a InSb nanowire based device, we can tune the chemical potential of the QD using an electrostatic gate (FG1) and the QD-superconductor coupling can be varied by another gate (BG1). For a weak QD-superconductor coupling, ground state of the system can be tuned alternatively with varying FG1 voltages (Fig. 2.11(b)). The

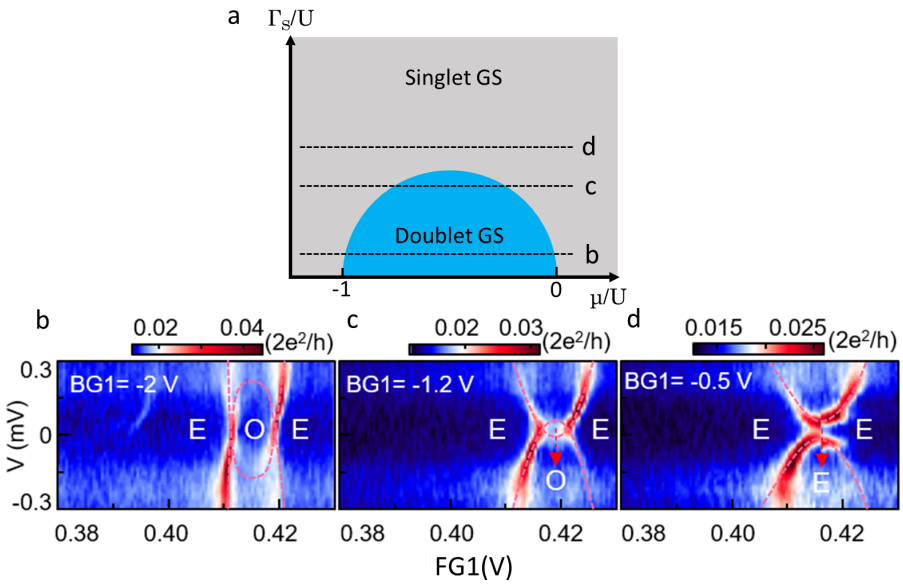

Figure 2.11: **Tuning of Andreev bound states energy.** **a**, QD ground state phase diagram. **b-d**, differential conductance as a function of source drain voltage and FG1 voltage.

energy levels crosses zero source drain voltage, i.e. $|\zeta|$ goes to zero, when the two spin states are degenerate. With increased QD-superconductor coupling (Fig. 2.11(c)), the region with doublet ground state(odd parity) shrinks. A further increased QD-superconductor coupling could totally eliminate the odd parity and the energy levels can no longer cross zero energy (Fig. 2.11(d)) without the influence of magnetic field.

At finite magnetic fields, the two doublets, $|\uparrow\rangle$ and $|\downarrow\rangle$, acquire Zeeman energies of $-\frac{1}{2}g\mu_B B$ and $+\frac{1}{2}g\mu_B B$ respectively, Landé g-factor and μ_B is the Bohr magneton, while the singlet state is not affected. In the case with doublet ground state, $|\zeta|$ increases with increasing magnetic field as illustrated in Fig. The linear increase of $|\zeta|$ might be suppressed if the the induced gap shrinks with increasing magnetic field[41]. In the case with singlet ground state (Fig), two transitions could happen at finite fields: One with increasing transition energy ($\xi_\downarrow$) and the other one with decreasing transition energy ($\xi_\uparrow$). It is worth noting that the transition with decreasing energy ($\xi_\uparrow$) could cross zero bias when the doublet $|D\rangle$ is degenerate with the singlet state $|S\rangle$ and thus create a ZBCP at finite fields. Although

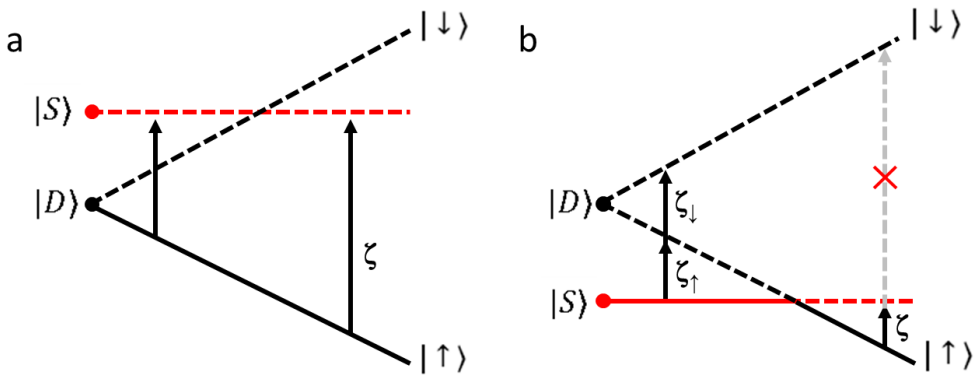

Figure 2.12: **Magnetic field dependence of Andreev bound states.** **a**, Field dependence of a single QD with a doublet ground state. **b**, Field dependence of a single QD with a singlet ground state.

the ZBCP should only appear in a Zeeman energy scale comparable to the ZBCP width for single level systems, level repulsion with other higher energy states in multiple level systems can lead to extended ZBCPs in field, which resemble the ZBCPs due to MZMs. Moreover, ABSs induced ZBCPs may also exhibit magnetic field angle anisotropy, owing to the g-factor anisotropy [41], and conductance quantization [40]. Distinguishing MZMs from ABSs is thus a difficult task to date. Our efforts to distinguish MZMs from trivial states are presented in chapter 5 and 6.

3.0 Experimental Methods

3.1 Introduction

In this chapter, we introduce the fabrication and measurement methods that have been used in our experiments. As discuss in chapter 2, several essential elements need to be engineered to create Majorana bound states in semiconductor nanowires. For the induced superconductivity, we need to make a nanowire in good contact with a s-wave superconductor. To control the chemical potential inside the nanowire, local electrostatic gates need to be fabricated. To have MBSs fully developed, devices need to be cooled down in a dilution refrigerator equipped with superconducting magnets to provide the desired Zeeman fields. And to detect the zero energy MBSs, filters and AC lock-in techniques have to be applied to increase the signal-noise ratio. All those aspects will affect the experimental results and thus need to be handled properly and carefully.

3.2 Device Fabrication

Our devices can be categorized based on their number of terminals. For the study of normal conductance quantization in quantum point contact, induced superconductivity and topological phase diagram, we focused on two-terminal geometry. A typical two-terminal device on local bottom gates is imaged using scanning electron microscopy (SEM) and shown in Fig. 3.1(a). It has a InSb nanowire contacted by two metal leads at the ends.

For the study of delocalized states and correlated MBSs, we fabricated three-terminal devices. Fig.3.1(b) shows a typical three-terminal device, which has a superconducting contact in the center and two normal contacts at the ends. The reason for adding one more normal lead is to measure the two ends of the nanowire-superconductor hybrid region simultaneously.

As can be seen in Fig. 3.1(a)(b) and it is also depicted in the side view sketch in Fig. 3.8(a), several thin metal bars underneath the nanowire serving as the bottom electrostatic

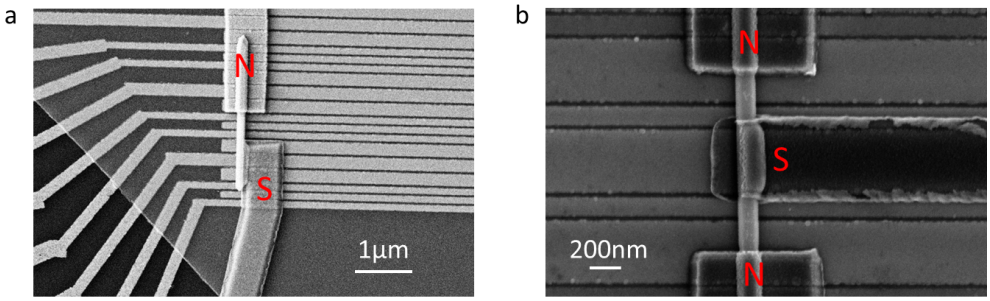

Figure 3.1: **Device images.a**,A typical two-terminal device on bottom gates, N indicates the normal contact while S indicates the superconducting contact. **b**, A Three-terminal device

gates, which give us the ability of creating tunnel barriers and varying the chemical potential inside the nanowire. Above the metallic gates, a thin layer of dielectric is placed to separate the gates from the nanowire and metal contacts. As the electric field will be induced through the dielectric layer, its quality and dielectric constant directly determine the effectiveness of the gates. Nanowires will be settled on the dielectric layer and be contacted by normal or superconducting materials. For three-terminal devices, superconducting contact will be placed in the middle of the nanowire, while two normal contacts are deposited at the two ends. While the processes vary for different types of devices, generally all the fabrication processes in this thesis include the following steps:

1. Fabricating of alignment markers and local gates.
2. Nanowire transferring.
3. Defining contact patterns using electron beam lithography (EBL).
4. Removal of PMMA residue and native oxide from nanowires.
5. Contact deposition.
6. Lift-off of the deposited film.

The general fabrication processes were developed by [12, 44, 45]. Each of those steps is critical to the final quality of the device. In the following sections, we will discuss them in

detail.

3.2.1 Optical Lithography and Electron Beam Lithography

Optical lithography is used in our process to define big patterns without demanding accuracy and alignment. Using a SUSS mask aligner, patterns can be created on photoresist in several seconds with a pre-fabricated photomask. Since the alignment in our optical lithography process relies on an optical microscope and the best alignment accuracy is around one μm, optical lithography is only used for large patterns like wire bonding pads or long contact leads, which could cost several hours to pattern with Electron beam lithography.

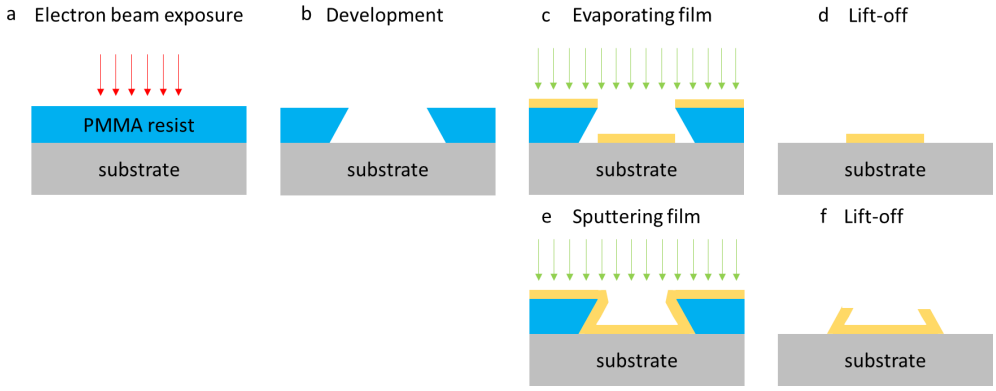

Figure 3.2: **Schematics of electron beam lithography and contact deposition. a-d**, EBL process followed by a thermal evaporation. **e-f**, Sputtering process results in 'dog ears' on the boundaries of the deposited film

Due to its great accuracy and flexibility, Electron beam lithography (EBL) is widely used in nanofabrication. In our experiments, we have utilized EBL to define patterns of alignment markers, local gates and contacts leads with standard EBL process using PMMA as the resist and MIBK/IPA as the developer. Fig. 3.2 shows schematics of a typical EBL process. A layer of PMMA is first coated on the whole sample. For both normal and superconducting contacts, PMMA 950 A4 resist is used to form a layer with thickness around 200 nm. For local gates fabrication, we use PMMA 950 A2 resist which results in a much thinner 60

nm layer. Electron beam exposure will change PMMA's solubility and thus enable the removal of the exposed area after development in MIBK/IPA solvent. EBL dose needs to be carefully tested before exposure as underdose or overdose could cause film lift-off problems. After development, a mask with desired patterns will be created on the sample. It is worth noting that oxygen plasma is usually necessary to remove the PMMA residue on the sample surface. The oxygen plasma needs to be calibrated carefully to avoid over-etching to the PMMA mask. Contact materials are then deposited on both the resist and the exposed area. In the last step, acetone is used to remove all the PMMA resist layer together with the deposited materials attached to it, leaving only the designed patterns. For most of our experiments, we used a Raith EBL system with a maximum acceleration voltage of 30 KV at the University of Pittsburgh. By fine-tuning the exposure dose and development process, we achieved sub-20 nm resolution.

3.2.2 Markers and Local Gates Fabrication

As the first step, different kinds of alignment markers need to be fabricated using EBL and thermal metal deposition. With those markers, we can establish a coordinate system to help computer-aided design (CAD) and further EBL patterning. Fig.3.3 shows an image of our chip design. Wire bonding pads (yellow patterns) and optical markers are fabricated us-ing optical lithography and thermal evaporation. These pads enable the connection between the device and the measurement setups. Big markers and bonding pads are required by any kind of device and we usually make a batch of them once in a while. After that, alignment markers (blue patterns) are patterned by EBL followed by deposition of 5 nm Ti and 50 nm Au. The next step is to make electrostatic gates that give us the ability to tune the chemical potential inside the nanowire. For the simplest devices, we just use the p-doped Si substrate as a global gate and a layer of 285 nm SiO_x serves as the dielectric. While global gate is convenient to use, it lacks the ability of local control.

For Majorana related experiments, local chemical potential control is crucial. We fabricated more sophisticated local bottom gates to have local electric field control. The details

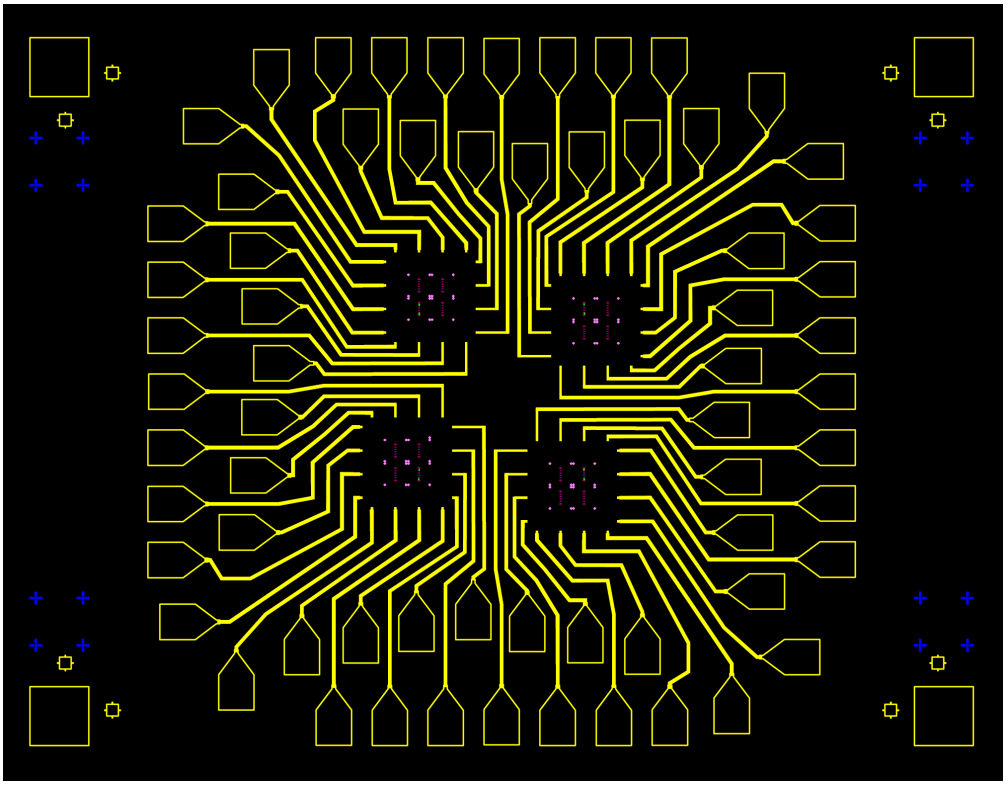

Figure 3.3: **Overall device chip design.** An image of the various patterns on the device chip. Yellow patterns (optical markers and wire bonding pads) are defined by optical lithography. Blue crosses (alignment markers) and pink patterns (local bottom gates) are patterned by EBL process. Device are fabricated on local bottom gates.

of the bottom gates fabrication are described in appendix A. Typical local gates (Fig. 3.4) consist of thin metal bars whose width varies from 100 nm to 600 nm. The width of the gates is determined by their purpose. In early experiments, we used a kind of mixed gates which includes repeating patterns of three 200 nm gates and three 100 nm gates. 200nm gates are usually called big gate (BG) and are used to tune the chemical potential of the nanowire segment underneath the superconducting contact. 100nm gates are usually called fine gate (FG), which is used to make tunnel barriers. Due to the concern that the gap between gates could result in nonuniform electric fields, we developed another type of mixed gates, which have repeating patterns of one 400 nm gate (as BG) and one 100nm or 300nm gates (as FG).

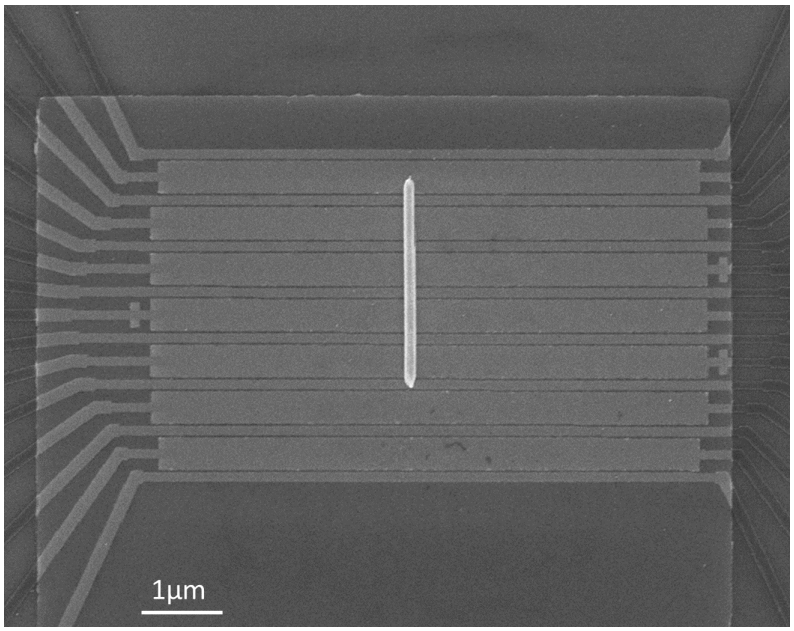

Figure 3.4: **SEM image of a well-aligned nanowire on local bottom gates.** The gates patterns consist of 100 nm wide fines gates and 400 nm wide big gates. A thin layer of HfO_2 (the bright transparent square over the gates) serves as the dielectric layer.

With that new type of gates, we only place one 400nm gate underneath the superconducting contact to achieve a more homogeneous electric field control. The gaps between nearby gates were chosen to be around 30 nm. While smaller gaps are achievable, we find small gap size may increase the risk of leaking between nearby gates at low temperature. A layer of 10 to 12nm HfO_2 is deposited on to the gates pattern as dielectric layer using an atomic layer deposition (ALD) system with the recipe described in appendix A. The HfO_2 film has a dielectric constant k around 20. While higher temperature is preferred for making good HfO_2 layer, we worked at 120°C due to the limitation of EBL resist. The resulting HfO_2 film has a breakdown voltage over 9 V, which is sufficient for our experiments.

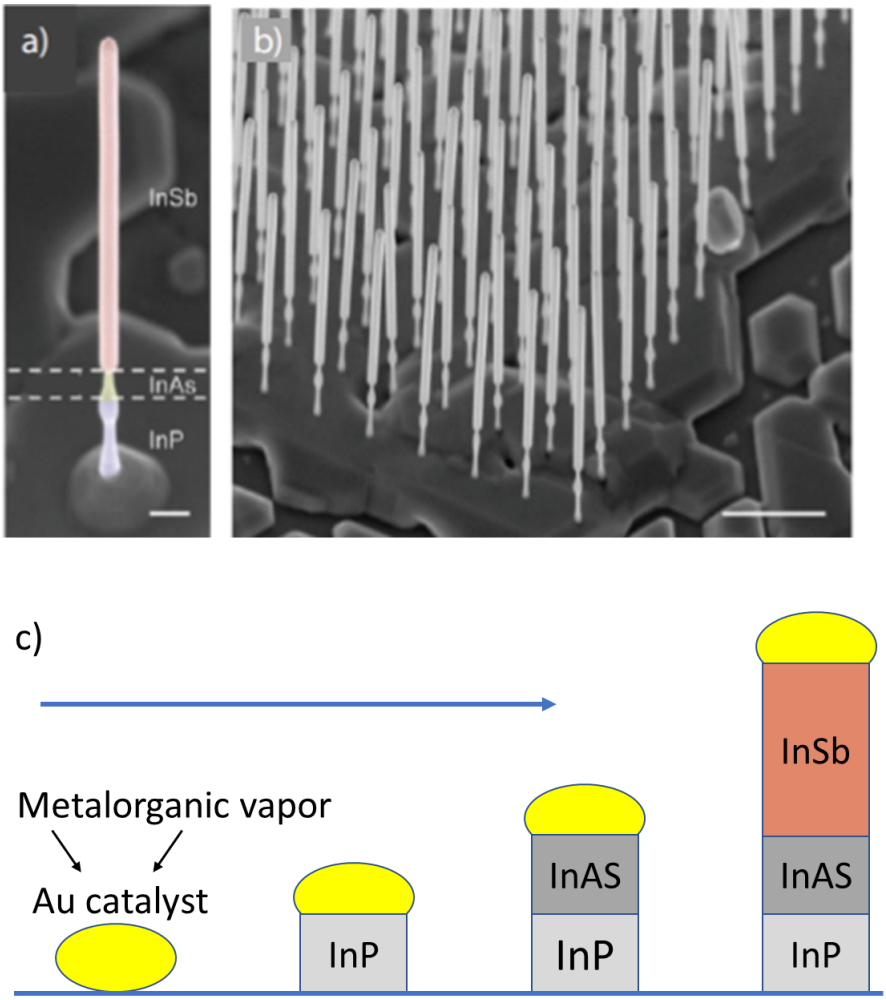

Figure 3.5: **InSb nanowires and the growth process. a-b**, SEM images of the InSb nanowires on growth chips. **c**, Schematics of the InSb nanowire growth process.

3.2.3 Nanowires Growth and Transferring

For Majorana fermions experiments, InSb nanowires (Fig. 3.5) have been widely used due to their great properties. First, their g-factor is quite large (30 - 70) [46, 47], which leads to a large Zeeman energy at finite magnetic fields. As a result, topological phase transition could happen below 0.5 T with a induced superconducting gap of 500 μeV and the chemical potential placed at the bottom of a one-dimensional subband. Since that field is far below

the critical field of NbTiN thin films [48], we have large freedom to study Majorana ZBCPs, which should appear after the topological phase transition. Second, it manifests high electron mobility, which ensures the ballistic transport inside the nanowire [49, 50]. Third, strong spin-orbit coupling strength (the spin-orbit length is about 200 nm) [51] helps open the gap at finite k as discussed in section 2.3.

Our InSb nanowires were grown at Eindhoven University of Technology by Diana Car, Sebastien R. Plissard, Sasa Gazibegovic, Ghada Badawy and Erik P.A.M. Bakkers using metalorganic vapor phase epitaxy (MOVPE) technique[52, 46].

The growth process is shown in Fig. 3.5(c), InP, InAs and InSb will grow in sequence under Au catalyst droplets. The InP stem facilitates nucleation, while InAs section is used for reducing the lattice mismatch between InP and InSb. During the growth of InSb, the evaporation of arsenic results in the thinning and eventually breaking of the InAs stem. That limits the aspect ratio to around 35 (100 nm in diameter and 3.5 μm in length), which means diameter needs to be increased together with the length of the nanowire. More details about the nanowire growth can be found in[46]. To solve the limited aspect ration due to the stem, stemless InSb nanowires are developed later with the help of a selective-area mask[53]. In this thesis, we only used InSb nanowires with stems. While longer nanowires are easier to make contacts with, we have other concerns regarding the nanowire diameter. From our experiments, we found extreme thin (<80 nm) nanowires may not be conducting, while thick nanowires (>150nm) are often hard to be pinched off at low temperature. So we normally choose nanowires with diameters between 100-150 nm and 3.5-4 μm in length. We also noticed not all the batches of nanowires gave good results. So once we find a good batch of nanowires, we will continually use it until we have problems finding more nanowires on the mother chip.

After we get the mother chip with nanowires, we need to first transfer nanowires to pre-fabricated gate chips. We utilized a customized manipulating system based on [54]. A micro-manipulator is used to control a thin needle in three dimensions with sub-micrometer accuracy. The needle itself can be made from a molten Indium droplet or be manufactured by commercial companies out of Tungsten. With a diameter of several hundred nanometers at the tip, the needle is thin enough to pick up a single nanowire and drop it to the device

chip. Due to the larger contact area between the nanowire and the device chip substrate than the needle, the nanowire will easily stick to the substrate. Position and orientation of the nanowire can be further adjusted by the needle. As the result, nanowires are able to be transferred onto a bottom gates array of several square micrometers and aligned to the desired angle with a deviation of several degrees (Fig. 3.4).

The control of the nanowire direction is important as we need to align the magnetic fields with the nanowire during measurement. After nanowire transferring, Acetone and IPA washing are necessary to remove unstable nanowires and other residues. Eventually, Van der Waals force fixes the nanowire tightly on the chip, following fabrication processes including coating of PMMA and sulfur passivation usually will not change the position of the nanowires. With nanowires carefully placed on the desired area, we are ready to make the contact patterns using EBL.

3.2.4 Surface Cleaning and Contact Deposition

Contact transparency is crucial for our experiments, since the induced superconductivity in nanowire, which is a prerequisite for topological phase and Majorana bound states, is largely determined by contact transparency. Transparent contacts can ,in general, reduce the inhomogeneity inside the device and thus reduce undesired trivial states, e.g. Andreev bound states. The fabrication of normal and superconducting contacts, however, is not straightforward and the biggest obstacle towards transparent contact is the native oxide on the nanowires. As studied in [55], a native oxide layer will be rapidly formed on the surface of InSb nanowire once they expose to oxygen. Most of the oxide is In_2O_3 and accompanied by less Sb_2O_5.

While the initial oxidation process happens in a timescale of seconds and results in a native oxide layer of several nanometers, further oxidation and rearrangement of the oxide are induced by diffusion and can last for months, which eventually terminates due to dense In_2O_3 [55]. Although we always keep nanowires in low pressure to slow down the oxidation, the final insulting oxide layer can be as thick as 10-20 nm and removal methods must be taken to get highly transparent ohmic contact on InSb nanowires.

Several methods have been tested to get rid of the native oxide. One straightforward method is sputter cleaning, which is a physical etching process using Argon ions to bombard the sample surface. While sputter cleaning is convenient and efficient method, it is hard to precisely remove only the oxide as the thickness of oxide is different for each nanowire. As over-etching could damage the nanowire and insufficient etching could leave a layer of oxide on the nanowire, both of which are bad for a transparent nanowire-metal interface, we only used that method in early devices. Hydrofluoric (HF) acid etching is another method we tested ,but could not get good induced superconductivity. The reason is possibly that the native oxide on InSb surface may not be completely removed by HF etching due to F-termination, which passivated the surface and prevents further reaction [56]. Comparing to using only sputter cleaning or HF etching, we found a combination of sulfur passivation and gentle sputter cleaning gave the best result, leading to eventually highly transparent interface and hard induced superconducting gap inside the nanowire. Our sulfur passivation process is developed based on [57, 50]. The biggest advantage of sulfur passivation comparing to other etching methods is that a thin layer of sulfur atoms will be formed over the nanowire after the oxide has been removed. This layer will prevent the nanowire from re-oxidizing for as long as several hours and give us enough time to transfer the sample into the vacuum chamber and pump to low pressure before contact deposition. Sulfur passivation also etches the oxide more gently comparing to the previous methods. With suitable solution concentration, the etching process can automatically terminate once the oxide has been removed, preventing further damage to the nanowire. While sulfur passivation itself is enough to make ohmic contact, a following gentle sputter cleaning process is helpful to further clean the nanowire surface. While strong sputter cleaning could result in damage of the nanowire surface , we optimized the sputter cleaning power and time to balance between the damage and cleaning. More details of those etching methods and results are discussed in chapter 4 and appendix A. We notice in-situ hydrogen cleaning could also give very good results [58, 59], while it has not been used in this theiss.

Since superconducting films may has positive stress that could often result in the missing of nanowire after film lift-off, superconducting contact is preferred to be made after the normal contacts, which help fix the nanowire. We found sulfur passivation may etch the

SiO_x substrate and results in a floating PMMA film, which eventually causes the film to deposit on the wrong area. To solve this problem, we made the outer contact leads in a separate step before transferring nanowire and contacting the nanowire. By doing this, sulfur passivation will only affect the area near the nanowire, which is mostly covered by $SiHfO_2$, avoiding etch the SiO_x substrate.

Once the oxide has been removed, contact materials will be deposited on the nanowire as soon as possible. We generally use electron beam evaporation to deposit normal materials like Ti, Au and Pd. Superconducting materials are sputtered in an AJA sputtering system using Argon RF plasma. Comparing to thermal or electron beam evaporation, sputtering could deposit materials with high melting points and chemical compounds from multiple sources, e.g. deposition of NbTiN from a NbTi target using argon-nitrogen plasma. Due to resputtering process, which cause re-emission of previous deposited materials in the vacuum chamber, a dedicated system is necessary.

NbTiN has been used as our primary superconductor partly due to its high critical field, which is typically above 15 T. NbTiN is also easy to make ohmic contact with InAs and InSb nanowires [44, 12, 49]. For all the NbTiN films in this thesis, we used several NbTi targets with 70% atomic percentage of Nb. Sputtering parameters such as power, N_2 flow and sample distance from the target are optimized to ensure the highest critical temperature, which could directly affects the induced superconductivity in the nanowire. More details of NbTiN film optimization are presented in chapter 4 and appendix A.

During sputtering, sputtered atoms ejected from the target could ballistically fly from the target to the substrates or collide with the Argon gas atoms that act as a moderator and diffusively deposit on the substrate after undergoing a random movement. In our process, sputtering pressure is set to several mTorr, which results in a combination of the two deposition mechanisms. As the result, films could deposit on the PMMA sidewall due to diffusive deposition and cause lift-off problems as shown in Fig. 3.2(e)(f). Since the films deposited on the sidewall can connect to the film on the PMMA, the lift-off might be more difficult and "dog ears" may form on edges of the film. In our practice, however, we had NbTiN film with positive stress for most of the time and lift-off process is actually much easier than evaporated normal metals. While stress in the NbTiN film facilitates the lift-off,

it could result in the displacement of nanowires. Considering the fact that we usually have asymmetric half-cover NbTiN film (as shown in Fig. 3.1(a)) on the nanowire to reduce the screening effect to the bottom gate, the stress from the NbTiN film could push the nanowire away or even break it if the nanowire is already fixed by normal contacts. Although that issue could be mitigated by reducing film thickness, displacement of nanowires after sputter NbTiN film is often a cause of low yield in our fabrication process. It is worth noting that one particular problem for normal contact deposition is overheating due to long deposition time. Because Au and Pd deposition require high beam current, which lead to high temperature, PMMA may melt and deform. Due to that reason, we sometimes had unsuccessful lift-off. We thus carefully monitor the temperature during deposition and pause the process if the beam current is abnormally high.

To get good induced gaps in the nanowire, wetting layers and sticking layers are also necessary. We have tested different combinations of Ti, Al and NbTi layers as the wetting/sticking layers and more details could be found in chapter 4.

After film deposition, the device chip is left in Acetone for at least two hours to remove the PMMA resist. We then image each device with scanning electron microscopy and keep the chip in a vacuum desiccator until being loaded into a dilution refrigerator.

3.3 Measurement Setups

All the data in this thesis are obtained at low temperature in a dilution refrigerator. The necessities of low-temperature measurement lie in several aspects. Since finite temperature leads to thermal broadening of quantum states, the lower the temperature the better the state will be resolved. Low temperature also results in stronger superconductivity with harder gaps, while also help suppress thermal excitation and quasiparticles in the superconductor. All those aspect directly affect the measurement of quantum states, e.g. Majorana signatures such as zero bias conductance peaks will be more prominent and better resolved with stronger superconductivity and suppressed thermal broadening.

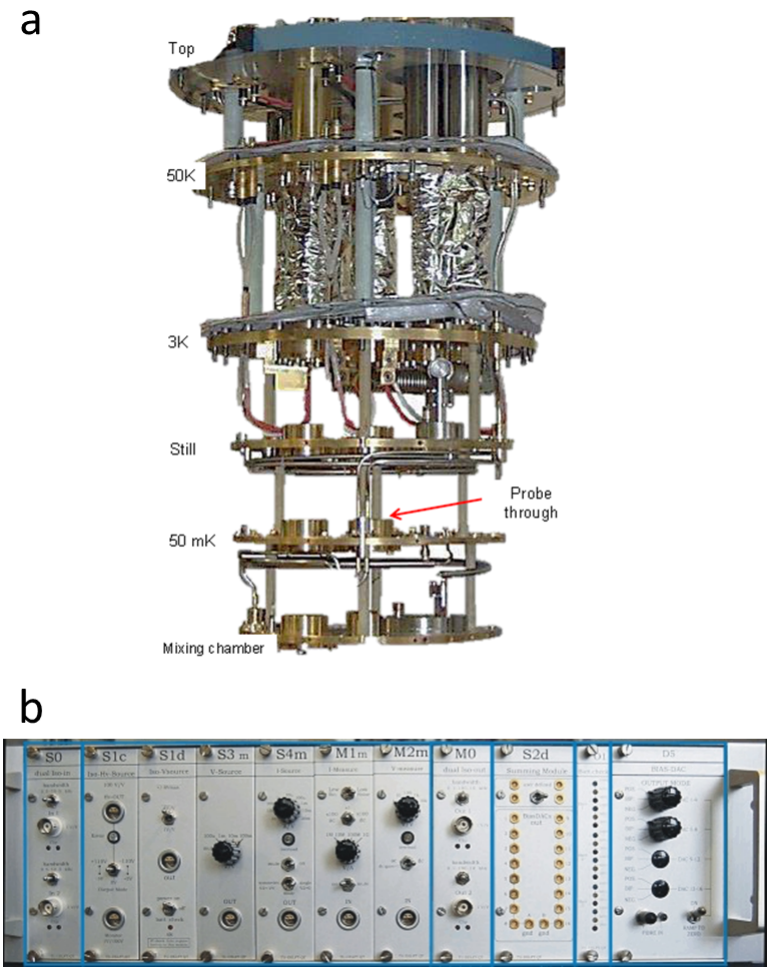

Figure 3.6: **Dilution refrigerator and IVVI rack.** **a**, Inside look of the multiple plates of a dilution fridge, the sample will settle around the mixing chamber to get lowest temperature. **b**, IVVI rack that includes current/voltage sources and current/voltage amplifiers.

Our measurement setup is shown in Fig. 3.6, the IVVI rack is developed and manufactured by Qutech at the Delft University of Technology. It is controlled by a computer through optical fiber, which gives galvanic isolation from the electrical interference from city electricity and computers. The IVVI rack has 16 Digital-to-analog converters (DACs) to provide different control signals. Current and voltage sources on the IVVI rack could convert DAC signals to input signals and different amplification modules are used to enhance the output signals. From the IVVI rack, signals need to go through a matrix box with 24 lines that directly connect to the measurement probe, which will be inserted into the refrigerator during measurement. The 24 lines out of the matrix box eventually lead to the pins on the chip carrier, where the device chip is attached and connected. The device chip is glued to the chip carrier and quantum devices are connected to the pins by wire bonding. All the controlling and data recording are manipulated by the QT lab software, which reads output measurement signals through GPIB interfaces.

The low temperature measurement is performed in our dilution refrigerators. We have two Leiden cryogen-free dilution refrigerators equipped with top-loading probes in our lab. The top loading probe enables quick cooling, which can cool down a sample from room temperature to base temperature within 8 hours. The internal structure of one of our refrigerators is shown in Fig. 3.6(a). It consists six plates. From top to bottom, temperature drops from room temperature to base temperature, which is the lowest temperature in the refrigerator. The base temperature corresponds to the lattice temperature and is achieved at the mixing chamber, where ^{3}He-rich mixture is diluted in ^{4}He-rich mixture in a closed cycle to provide continuous cooling. The cooling mechanism is based on a thermodynamic phase transition in the ^{3}He and ^{4}He mixture. More details about dilution cooling can be found in [60].

Our refrigerator can reach a base temperature of 10 mK without inserted probe. With probe inserted and heat load due to wire connection from the room temperature measurement setup, base temperature is inevitably higher and we usually have a base temperature around 40-50 mK during measurement.

The device chip, which is mounted on the cold finger of the probe, is thermally connected to the mixing chamber and in principle can reach the same lattice temperature of the the

mixing chamber. The real concern here, however, is the effective electron temperature, which can be much higher due to the electrical noise from the room temperature setup. To reduce the influence from room temperature electronics, a series filters need to be applied.

At room temperature side, a π filter is first applied to each DC line to reduce noise between 10MHz to 100 MHz. At the low temperature side near the sample, two more types of filters are used: copper powder filters to filter high-frequency noise around several GHz; Low-pass RC-filters with a cut-off frequency of 10 KHz can further reduce high frequency noise.

Measurement signals and control signals are provided by Digital-to-analog converters (DACs) at the room temperature side. In a typical current measurement, a DAC provides a bias voltage that crosses the sample, while the outcoming current is amplified to a scale of mV and measured by digital multimeters and standard AC lock-ins. Apart from the AC lock-ins, all the measurement parts are powered by DC batteries to avoid interference from the power grid.

As a magnetic field perpendicular to the spin-orbit field is critical to induce the topologically nontrivial phase and Majorana bound states, our refrigerators are equipped with superconducting magnets. One of the refrigerators has a solenoid magnet capable to reach a field of 9 T. The other refrigerator has a 2D vector magnet, which gives us the ability to explore field anisotropy of Majorana ZBCPs. 2D magnet is also helpful to compensate the misalignment of the nanowires.

3.3.1 Tunneling Measurement in the Two-terminal Geometry

In almost all the experiments, we performed tunneling spectroscopy to study different quantum states. With the help of bottom gates, a tunneling barrier is created to separate the metal lead, which serves as the probe, and the region to be investigated, which in most cases is the nanowire-superconductor hybrid region. As the metal lead and nanowire section have their own density of states (DOS), the tunneling process can be treated as a perturbation

noise and the tunneling current is given by

$$I = \frac{4\pi e}{\hbar} \int_{-\infty}^{\infty} [f(\epsilon + eV) - f(\epsilon)] \rho_S(\epsilon + eV) \rho_L(\epsilon) |T|^2 d\epsilon \tag{3.1}$$

where f is the Fermi-Dirac distribution and V is the bias voltage applied across the tunnel junction, ρ_S and ρ_L are the DOS of the sample and lead, respectively, and ϵ is the energy with respect to the Fermi level. With the assumptions that the transmission matrix T is independent on the bias voltage and that the lead DOS is approximately a constant, we can differentiate Eq. 3.1 under the low-temperature limit to have

$$\frac{dI}{dV} \propto \rho_S(eV) \tag{3.2}$$

This result shows that the differential conductance across the tunnel barrier is directly proportional to ρ_S. And thus we can study the DOS of the sample by measuring the differential conductance. Differential conductance can be obtained by taking a numerical derivative of the current I curve, which is usually noise for a small signal. An alternative method to measure the differential conductance is using lock-in techniques, which apply a small AC bias voltage ΔV_{ac} to the stationary source-drain voltage. The measured quantity of $\Delta I_{\text{ac}}/\Delta V_{\text{ac}}$ is a good approximation to the differential conductance dI/dV when ΔV_{ac} is small. Since lock-in amplification can be used with the AC signal, noise can be greatly filtered. As a trade off, however, the longer integration time is required for each data point.

Fig. 3.7(a) present a sketch of a typical two-terminal configuration. Due to the presence of a series of resistance in the measurement circuit, we must correct the measured differential conductance from the lock-in removing the contribution from the measurement circuit. Apart from the resistance from the RC filters, current amplifiers and lock-in amplifiers also have non-negligible impedances. These impedances are treated as R_{im} in the circuit and vary for different amplification settings. Generally, the resistance from amplifiers and filters is in the range of 10 - 50 $k\Omega$ in total and cannot be neglected compared to the device resistance in the tunneling regime, which is around 10 - 100 $k\Omega$.

Besides those resistances that can be measured with a dummy sample, contact resistance may exist at the interface between different materials. For example, between the superconductor and the normal metal lead or the nanowire and the normal contact. Those contact

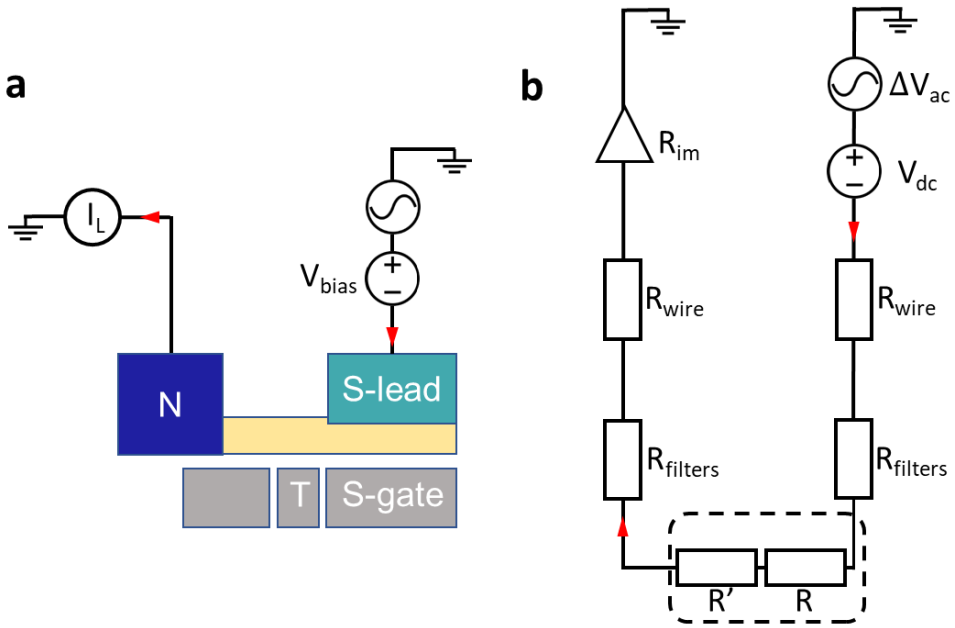

Figure 3.7: **Two-terminal measurement.** **a**, Schematics of the two-terminal device and measurement setups, where a bias voltage is applied through the superconducting lead. Bottom gate tunnel gate T is used to create the tunnel barrier and S-gate is used to tune the chemical potential inside the nanowire. **b**, Simplified measurement circuit diagram representing all elements of the circuit as resistors. The device is represented by two resistors inside the dashed line box, where R is the device resistance and R' is the contact resistance.

resistances could vary with each device, but usually on the order of several $k\Omega$ and does not affect the results and conclusions as strong as other series resistances. Only when we care about the exact differential conductance value, e.g. when measure the quantized Majorana ZBCPs, we estimate and substrate the contact resistance.

3.3.2 Tunneling Measurement in the Three-Terminal Geometry

To better distinguish MBSs from other trivial states and verify the prediction that MBSs appear in pairs, we made three-terminal devices that could be used to probe the two ends of the topological regime simultaneously. As shown in Fig. 3.1(b), two normal contacts connect

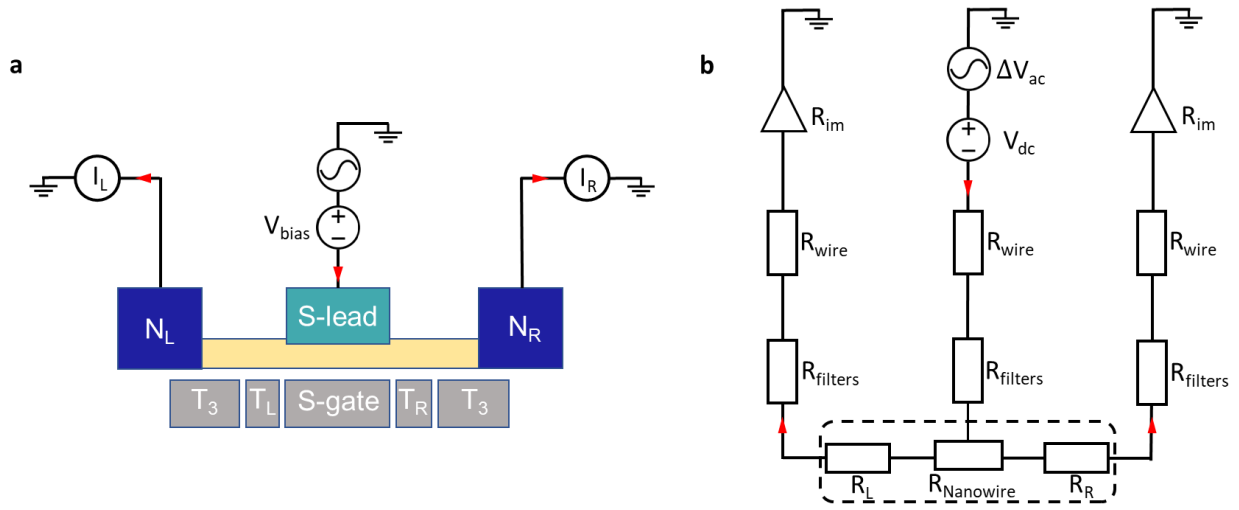

Figure 3.8: **Three-terminal measurement. a**, Schematics of the three-terminal device and measurement setups, where a bias voltage is applied through the middle superconducting contact and two normal contacts serve as the probes. Bottom gate T_L and T_R are used to create the tunnel barriers and S-gate is used to tune the chemical potential inside the nanowire region. **b**, Simplified measurement circuit diagram representing all elements of the circuit as resistors. The device is described as $R_{Nanowire}$ plus two contact resistances R_L and R_R.

the nanowire at the two ends, while the superconducting contact is placed in the middle. A three-terminal measurement can be considered as two two-terminal tunneling measurements. Two methods have been used to measure our three-terminal devices. The first method is alternatively biasing the two normal leads and measuring current and different conductance from the superconducting lead. That can be done automatically by using a special module in our IVVI rack, which can apply bias voltage through one normal lead while floating the other normal lead. The advantage of this method is the measurements on the two sides can be considered as two independent tunneling measurements. However, alternative measurement of the two sides is much slower comparing to the second method.

The second method we used only bias the superconducting terminal and measuring from

the two normal terminals simultaneously. To obtain the actual differential conductance dI/dV on both sides, we must correct the measured differential conductance from the lock-in removing the contribution from the measurement circuit. First, we need to subtract the series resistances of the wiring, the RC filters and the input impedance of the amplifier. As indicated in Fig. 3.8(b), the AC lock-in voltage $\Delta V_{\rm ac}$ drops across the $\rm R_{wire}$ and the $\rm R_{filters}$ of the voltage bias line.

This voltage drop is $\Delta V_{\rm s} = (\Delta I_L + \Delta I_R)(R_{\rm wire} + R_{\rm filters})$, where ΔI_L and ΔI_R are the AC current passing through the left side and the right side of the device respectively. For the left side, the AC voltage drops across the second set of RC filters of the normal contact line, the DC wires and the impedance of the amplifier. This voltage drop is given by $\Delta V_{\rm n} = \Delta I_L (R_{\rm wire} + R_{\rm filters} + R_{\rm im})$.

Then the AC voltage applied to the nanowire device on the left side is $\Delta V_L = \Delta V_{\rm ac} - \Delta V_{\rm s} - \Delta V_{\rm n}$ and the corrected G'_L for the left side is:

$$\begin{aligned} G'_L &= \frac{dI_L}{dV_{\rm L}} = \frac{dI_L}{dV_{\rm ac}}\frac{dV_{\rm ac}}{dV_L} = G_L\left(\frac{1}{1-\frac{\Delta V_{\rm S}}{\Delta V_{\rm ac}}-\frac{\Delta V_{\rm n}}{\Delta V_{\rm ac}}}\right) \\ &= G_L\left(\frac{1}{1-(G_L+G_R)(R_{\rm wire}+R_{\rm filters})-G_L(R_{\rm wire}+R_{\rm filters}+R_{\rm im})}\right) \end{aligned} \tag{3.3}$$

where $G_L = \frac{dI_L}{dV_{\rm ac}}$ and $G_R = \frac{dI_R}{dV_{\rm ac}}$ are the measured differential conductances from the lock-ins connected to the left side and the right side respectively. Similarly,

$$G'_R = G_R\left(\frac{1}{1-(G_L+G_R)(R_{\rm wire}+R_{\rm filters})-G_R(R_{\rm wire}+R_{\rm filters}+R_{\rm im})}\right) \tag{3.4}$$

We used that method in Chapter 6 where we study three-terminal devices and have verified it can give accurate results when the resistances of the two sides are in the same order.

Apart from the correction above, contact resistance may also need to be subtracted when accurate conductance is desired, e.g. in the searching of conductance quantization of Majorana ZBCPs. Contact resistance can be roughly estimated by tuning the device to saturated regime and measuring the saturation resistance. When there are multiple conductance plateaus from different subbands, contact resistance can also be chose to fit the

actually plateaus to quantized values. That kind of estimation is often used in the study of quantum point contact.

The study of Majorana quantization, however, is a different story. Actually, a unique difficulty in unambiguously establishing quantized Majorana conductance is methodological in nature. Quantized Majorana conductance is predicted to occur even when the tunnel barrier transmission is non-monotonic and does not exhibit quantized conductance plateaus [1]. However, under realistic conditions in nanowire devices featuring some degree of disorder it is more likely that only a single quantized Majorana appears, but no higher quantized plateaus. As a consequence, the absolute value of conductance cannot be calibrated accurately, as only a single value of known conductance (i.e. the presumed quantized Majorana conductance) is present, which needs to be corrected for series resistances inevitably present in the measurement circuitry and the device. Since the contact resistances caused by metal-semiconductor interfaces can only be roughly estimated, but not measured independently, This methodological challenge actually hurdles accurately verifying the exact conductance at a supposed quantized plateau due to a Majorana.

4.0 Optimization of the NbTiN Contact

4.1 Introduction

As discussed in chapter 2, a prerequisite for generating Majorana bound states in semiconductor nanowires is induced superconductivity. Apart from determine the formation of Majorana bound states, the induced superconductivity also affects the detection of Majorana bound states and non–trivial physics associated with them, e.g. non–Abelian statistics, as the zero energy Majroana bound states is separated from the trivial excited states by the topological gap and the topological gap scales with the induced superconducting gap [20]. As the consequence, improvements lead to better induced superconductivity are always coveted.

As introduced in chapter 3, we use niobium titanium nitride (NbTiN) as our primary superconductor due to its high critical temperature, high critical field as well as it is relative easy to be contacted with InSb nanowires [12, 49]. Since the induced superconductivity inside the nanowire is induced by proximity effect, its quality is largely determined by the parent superconductor, i.e. NbTiN, the nanowire-superconductor interface and the electronic band structure in the nanowire. Among these parameters, we mainly focus on the optimization of the quality of the parent superconductor and the nanowire-superconductor interface as they can be greatly determined by the fabrication processes.

In this chapter, we introduce the methods we have used to improve the induced superconductivity, mostly based on the shape and size of the superconducting gap. In section 4.2, we discuss the optimization of the NbTiN film. In section 4.3, results of different InSb etching processes are reviewed. The effect of sticking layers and angle deposition technique are presented in section 4.4 and 4.5. In the last two sections 4.6 and 4.7, data on hard induced gaps and quantized conductance are presented as the result of improved contact recipe.

4.2 Critical Temperature Optimization of NbTiN Films

Superconducting niobium titanium nitride (NbTiN) has been widely used in many areas, including photodetectors [61], narrow band filters [62] and microwave parametric amplifiers [63] and most relevantly circuit quantum electrodynamic experiments.

In our experiments, we choose NbTiN mainly because of its three outstanding properties. First, it has a high critical temperature (up to 15 K [64]). Second, the NbTiN film is stable against oxidization as a oxide layer is naturally formed to stop further oxidization, so no capping layer is needed. Third, contact recipe with nanowires has already been widely studied [12, 49] and it is relatively easy to achieve ohmic contact based on those recipes. While the interface between the nanowire and the superconductor greatly determines the induced superconductivity, the quality of the superconductor itself also plays an important role. In this section, we discuss the methods we tested to get improved NbTiN films.

Our NbTiN film is deposited using reactive DC magnetron sputtering from a NbTi target under a stable N_2 flow. During the sputtering process, target materials are ejected from the target due to the bombardment of argon and nitrogen plasma. Because of the relative high gas pressures (several mTorr) during sputtering, apart from flying ballistically, sputtered ions will also collide with Argon ions and move diffusively toward the sample, resulting in an isotropic deposition.

The sputtering target we used is a Nb0.7Ti0.3 (by atomic percent) metal plate with a diameter of 3 inches.The sputtering system can reach a background pressure below 1×10^8 mbar. Comparing to other deposition methods like molecular beam epitaxy or chemical vapor deposition, sputtering does not require high substrate temperatures and thus gives us more freedom on device fabrication. The resulting NbTiN film is polycrystalline with morphology.

Out of many parameters that could affect the quality of the sputtered film, we have tested the effect of N_2 flow, sputtering pressure, sputtering temperature, sample holder distance from the target, film thickness and different targets.

Generally, the critical temperature remains constant when the film exceeds a certain thickness and decreases rapidly when the film is less than 50 nm. As analyzed in [64], for

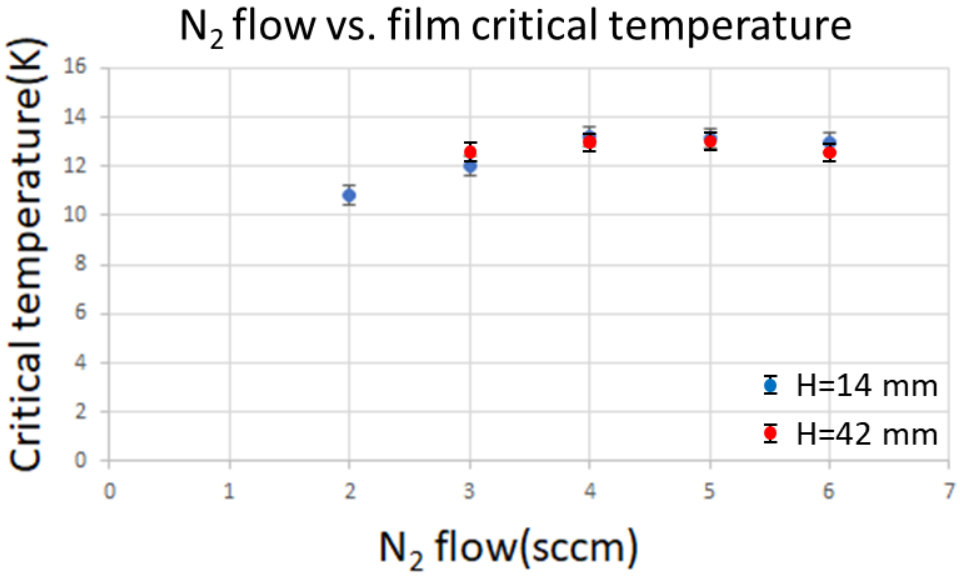

Figure 4.1: **Effect of N_2 flow on the NbTiN critical temperature.** Critical temperature of NbTiN film is sensitive to the N_2 flow during deposition. Here we vary N_2 flow from 2 sccm to 6 sccm while other parameter are fixed and measuring the critical temperature of those films. Best critical temperature 13.2K is achieved with 4 sccm N_2 flow.

an 80 nm thick NbTiN film, there could be three layers with different composition in the NbTiN film: a 10-nm-thick surface layer that rich in oxygen due to the natural oxidation of the surface, a 50-nm-thick inter layer with uniform nitridation of NbTi, and a 20-nm-thick initial layer that could be affected by the substrate materials. To make sure we have a stable and constant NbTiN film, we always deposit NbTiN film to be thicker than 60nm. Among other parameters, we found N_2 flow is the most sensitive variable to the film critical temperature.

We did several tests on the effect of N2 flow with different sample-target distances and the most recent test is summarized in Fig. 4.1. The test films were deposited on clean SiO_x substrate under 4 mTorr pressure at room temperature. We tried to keep the same film thickness ($\sim$ 100nm) for each chip and deposition times were adjusted based on the deposition

rate for different N2 flow. A 5 nm layer of NbTi was deposited first as the sticking layer. To evaluate the film, we used four-terminal current measurement to determine the critical temperature, which is directly related to the film quality. The measurement was done in a liquid H^4 system at temperature around 3.5 K.

During measurement, the device temperature was controlled by a heater and passed the critical temperature twice from high to low and low to high to get accurate critical temperatures. Under a constant 10 meV bias current, the resistance of each film is usually several hundreds of ohm in normal status and vanishes when the film becomes superconducting. The residual-resistance ratio of the film with highest T_c is 1.07, which is comparable to other results in literature [64].

As Fig. 4.1 presents, for a sample-target distance of 14 mm, the critical temperature increases from 9 K to over 13.3 K when the N_2 flow increases from 2 sccm to 4 sccm. From 4 to 6 sccm, the critical temperature remains around 13K. For a sample-target distance of 42 mm, which is the closest distance to the target, the highest T_c also reaches over 13 K. But the film usually has a lot of cracks probably due to the high stress in the film, which is not favorable in device fabrication.

Comparing to N_2 flow, other parameters have much smaller effect on the critical temperature. We thus set N_2 flow to 4 sccm and used the parameters described above for most of our experiments.

4.3 Etching Methods for Removal of the Native Oxide on InSb Nanowires

As analyze by Takei et al [26], nanowire-metal interface inhomogeneity is the most possible cause of soft induced gap in early experiments such as [12]. Since the induced gap directly affect the detection of Majorana zero modes and their topological protection, improvement of the interface is always a priority for our experiments.

In the optimization of nanowire-superconductor interface, the biggest obstacle that prevents us to get transparent interface is the native oxide layer formed on the nanowire surface. As studied in [55], a thin layer of several nm can form almost instantly when the nanowire

is exposed to air and the oxide layer can reach as thick as 10-20 nm eventually.

As the native oxide will act as an insulating layer, it must be removed before depositing any normal or superconducting materials. Several methods have been used to remove oxide. Based on their etching mechanisms, they can be categorized as physical and chemical etching. Physical methods include argon sputtering cleaning and ion milling, while chemical methods include Hydrofluoric acid (HF) etching, hydrogen cleaning and sulfur passivation. While those methods could all remove the native oxide, the resulting interfaces vary greatly due to their etching mechanisms. Since insufficient etch would leave native oxide and overetch that damage the nanowire could introduce new source of inhomogeneity, the optimization of the etching process is thus a tricky task. In this section, we will discuss those methods one by one.

4.3.1 Argon Plasma Etching

The most straightforward way to remove the oxide is physically striking the oxide away, which can be done in-situ using sputter cleaning or ion milling. Both sputtering cleaning and ion milling use ion beams to bombard the sample surface and thus can remove native oxide layer as well as the nanowire material.

During those processes, ions that strike the sample surface transfer their energy to surface atoms and make them escape from the surface. Our sputter system is capable of doing sputter cleaning and our electron beam evaporation system is equipped with an ion milling source. Both of them are using argon ions to polish the sample surface. Since our main purpose of improving the contact is to get good induced superconductivity, we focused more on sputtering cleaning as it can be done in-situ in the sputtering chamber.

Although sputter cleaning is very convenient as it can be done in the same vacuum chamber for depositions and no pre-treatment to the sample is required, their side effects are often undesirable and inevitable. These side effects include overheating, gas incorporation and contamination, and surface roughening. While the impacts of other side effects might be hard to estimate, the surface roughening effect can be clearly seen by atomic force microscopy (AFM) as shown in Fig. 4.2(a). Here we used argon plasma with the power of 100 watt and

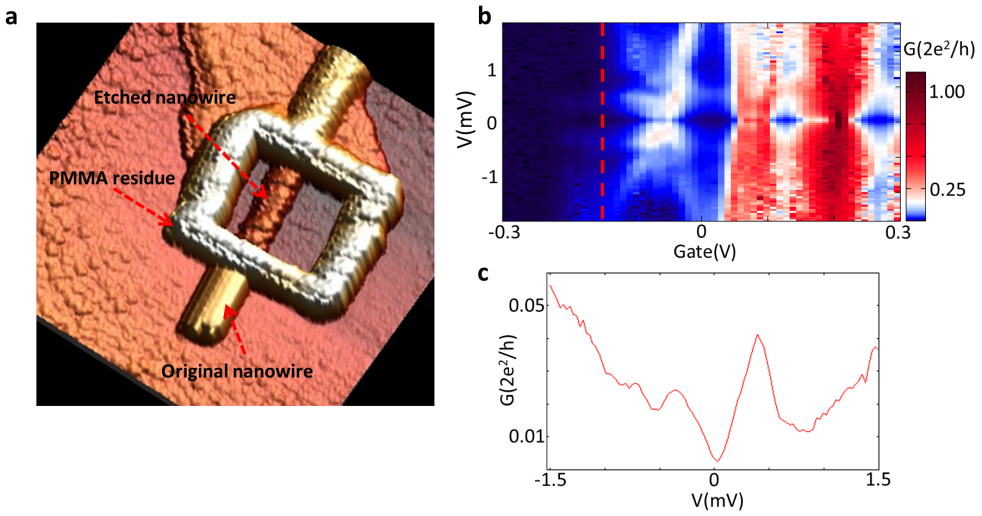

Figure 4.2: **Results of high power sputter cleaning.** **a**, Atomic force microscopy image of a sputter cleaned nanowire. The sputter cleaned the section of the naonwire (within the square) is damaged comparing to the intact section. **b**, Scan of differential conductance as a function of bias voltage and global gate voltage. A soft induced gap appear near the pinch of regime. **c**, linecut taken from panel b at the -0.14 V(indicating by red dashed line) shows the V shape of the induced gap.

pressure of 3 mTorr to clean the nanowire for 300 seconds. To selectively sputter clean a section of the nanowire, we first used E-beam lithography to open a window on the PMMA resist and then sputter cleaning the sample. After removing the PMMA resist, we see the nanowire becomes much thinner due to the etching. More importantly, the nanowire surface is significantly roughened within the window while the nanowire surface outside the window remains intact. Actually, after the sputter cleaning, even the PMMA resist degenerated and coull not be removed by Acetone, which results in the standing wall around the window. Another side effect of sputter cleaning is that ions may prefer to kick out lighter atoms. In the case of InSb, an indium rich layer might be formed on the nanowire surface, which may also induce superconductivity. This is not favored in the case only normal conductivity is needed, e.g. the normal contact.

The resulting induced gaps with high power sputter cleaning are presented in Fig. 4.2(b)(c). While the device resistance is as low as 3-5 KΩ using only high energy sputter cleaning, the damaged nanowire surface hinders the realization of good induced superconductivity. The superconducting contacts are made with 5 nm NbTi and 120 nm NbTiN. We measured the device in a dilution refrigerator and did tunneling spectroscopy to resolve the induced gap. This kind of two-terminal device and tunneling spectroscopy is our standard method to test nanowire and contact recipes. After e-beam lithography, the sample was sputter cleaned for 200 seconds using 100 watt power under an argon gas pressure of 3 mTorr. As we can see from the linecut (Fig. 4.2(c)), the gap shows a V-shape, which means a significant density of states within the energy gap. That kind of V-shape gap is often referred as 'soft gap' in literature. On the contrary, an ideal superconducting gap should have a U-shape due to minimal density of states within the gap. While the device resistance is pretty low ($\sim$3 kΩ) in the open regime, which indicates little native oxide remaining, we believe the roughness and thus inhomogeneity caused by sputter cleaning lead to such a soft gap.

We point out some of the problems caused by argon sputter cleaning might be mitigated by lowering the plasma power. The relatively thick (10-30 nm) native oxide on InSb nanowires, however, makes it impractical to use low energy argon plasma to clean the whole native oxide as the suitable etching time is hard to determine giving the oxide thickness may vary for each nanowire.

4.3.2 Wet Etching Methods

Wet etching is typically done using chemical reactions to remove the native oxide. We have tested two wet etching methods: Hydrofluoric acid (HF) etching and sulfur passivaton.

For HF etching, as studied in [56], native oxides on InSb surface may not be completely removed due to F-termination mechanism, which passivated the surface and prevents further reaction. In our practice, with various HF concentrations and etching time tested, we never get contact resistance as low as we had with sputter cleaning ($\sim$3 kΩ) or sulfur passivation ($\sim$1 kΩ). Typical device resistance using HF etching is around 10 kΩ at low temperature,

which indicates a layer of oxide or other reaction residue due to HF etching.

We suspect apart from the incomplete etching of the native oxide, re-oxidization may also happen during transferring the sample into the deposition chamber and before the deposition chamber reaching high vacuum, which can take 2-3 minutes. As InSb nanowires could oxide in seconds, the re-oxidization is hard to prevent in this case.

Comparing to previously tested etching methods, sulfur passivation yielded best results in our experiments.

Sulfur passivation is a chemical etching and passivation process based on ammonium polysulfide, $(NH_4)_2 S_x$, water solution. As studied in [57, 45], sulfur passivation with diluted $(NH_4)_2 S_x$ solution could be self-terminating after removing the native oxide and thus minimize the etching of the InSb nanowires. That means sulfur passivation could in principle maintain the nanowire crystalline structure while effectively removing the native oxide. Sulfur passivation could also passivate the InSb surface, resulting in monolayer sulfur atoms that could significantly slow down the re-oxidization process.

During our testing, we developed several recipes based on sulfur passivation and achieved good results. The general steps are described below. First, We add 0.29 g elemental sulfur into 3ml $(NH_4)_2 S$ solution to get ammonium polysulfide, $(NH_4)_2 S_x$, solution. After elemental sulfur is fully dissolved, the solution is diluted by deionized water with a ratio between 1:200 to 1:500. Samples will be immersed into the diluted solution for 30 mins at 60°C. After sulfur passivation, the sample will be transferred into the deposition chamber as soon as possible. Since oxidation reaction could be accelerated by absorbing energy from photons, screening light during passivation and sample transferring is helpful to reduce possible oxidization. Due to this reason, our sulfur passivation is done with minimal exposure to light as well as oxygen. With only sulfur passivation, 2-3 KΩ device resistance has been easily achieved with both normal and superconducting materials.

For superconducting contact, however, we found only sulfur passivation is not enough to achieve a hard induced gap. The reason probably lies in two aspects. Firstly, the monolayer sulfur atoms due sulfur passivation will remain on the nanowire surface and potentially induce inhomogeneity on the nanowire-metal interface. Secondly, the original surface layer of the nanowire might be damaged by the oxidation reaction and need to be removed to

provide an intact crystalline surface.

To further clean the nanowire surface, we apply an in-situ gentle Argon sputter cleaning after sulfur passivation and before depositing superconducting materials. With a power of 20 watt and 10 seconds etching time, we estimate 1-2 nm of the top layer of the nanowire could be etched away and results in a pristine InSb surface. The sputter cleaning power and time we apply here is much smaller and shorter than the high energy sputter cleaning we used previously. As the result, we are not worried about the surface roughening here. The resulting induced gaps from sulfur passivation based recipes will be shown in section 4.6 and 4.7.

Films deposited	Low temperature resistance	Induced gap yield	Gap width(4Δ)
Sputtered NbTiN 120 nm	2-10Kohm	10%	500-600 μeV
Evaporated Ti 5 nm + sputtered NbTiN 120 nm	2-6Kohm	40%	500-750 μeV
Evaporated Ti 5 nm + sputtered NbTi 5 nm+NbTiN 120 nm	2-6Kohm	75%	500-750 μeV
Evaporated Ti 4 nm + Al 4 nm + sputtered NbTiN 120 nm	2-6Kohm	No gap features observed	NA
Evaporated Ti 4 nm + Al 8 nm + sputtered NbTiN 120 nm	2-5Kohm	40%	500-800 μeV

Figure 4.3: **Results of different wetting layers.** Here we compare the results of different wetting layers. While all the combinations of wetting layers give low saturated resistance at low temperature, the effect of wetting layers is significant in increasing the yield of induced gaps.

4.4 Effect of Wetting Layers

It is known that a thin wetting layer could greatly improve not only the contact resistance but also induced superconductivity [45]. Similar to sticking layers that help normal metal films to attach on the sample surface, wetting layers help sputtered films uniformly deposit on the sample. Wetting layers could also reduce lattice mismatch and thus improve the quality of thin NbTiN films [65]. As shown in Fig. 4.3, we tested different wetting layers and used induced gap yield and low temperature resistance as the benchmarks.

The samples tested in Fig. 4.3 are first processed by sulfur passivation with 1 : 500 diluted $(NH_4)_2 S_x$ solution and followed by a gentle sputtering cleaning to further clean the nanowire surface. Wetting layers are then deposited in-situ before the deposition of 120 nm NbTiN film. Out of those wetting layers, we found a combination of 5 nm evaporated Ti and 5 nm sputtered NbTi gives the best result. The characterization of those devices is shown in section 4.6. As the results shown in Fig.4.3 were obtained in 2015, we later improved our recipe based on [45, 66]. The new recipe only use 5nm sputtered NbTi as the wetting layer and also get similar results. More details will be presented in section 4.7.

4.5 The Angle Deposition Technique

Due to the hexagonal shape of the InSb nanowire, we found gaps between the NbTiN films deposited on the nanowire and the NbTiN films deposited on the substrate, if the deposition angle is perpendicular to the substrate. Although sputter deposition can be isotropic, the gap did not filled in our case as shown in the TEM image (Fig. 4.4(c)). That could cause severe problems if the deposited NbTiN film is not thick enough to cover the gap. Actually, we found tunneling junctions between the weak connected NbTiN films in some testing devices with thin NbTiN film($\sim$90 nm), while the nanowires have diameters between 120-150 nm. With such a tunnel junction forms between different pieces of NbTiN films, we may accidentally observed the superconducting gap of NbTiN film due to this kind of junctions (See Fig. 4.12 for details).

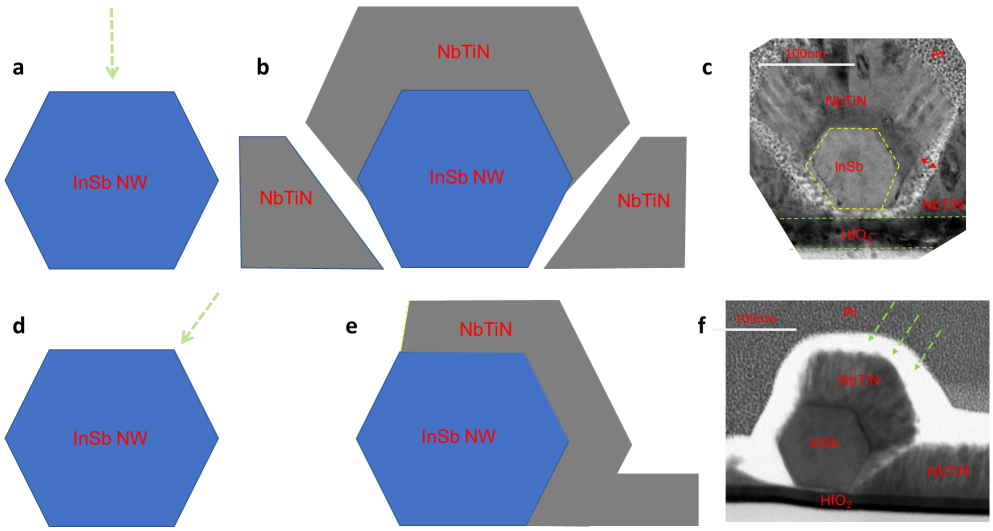

Figure 4.4: **The angle deposition technique. a-b**, Illustration of perpendicular deposition. A clear gap has formed as shown in the TEM image(panel c). **d-e**, Illustration of angle deposition. The gap is significantly reduced with a deposition angle of 60° (panel f).

The unfilled gap may still cause problems even if a thick enough NbTin film cover the top of the gap, since the resulting film is not uniform. To solve this problem, we developed an angle deposition technique. The idea is illustrated in Fig. 4.4(d)(e). By using a customized sample holder, which can hold the sample with a fixed angle against the original sample holder, ideally NbTiN can enter the space underneath the nanowire and the gap can be thus filled up. We tried angles of 45° and 60°. As shown in Fig. 4.5(f), a 60° deposition angle significantly reduced the gap. Although a small gap may still form, we have not encountered undesired tunneling junctions anymore after using this technique. Another advantage of this technique is that we can reduce the thickness of NbTiN film. Even a 60 nm thick film is enough to cover the nanowire when the deposition angle is 60° and a thinner film usually could lead to smaller film strain and easier film lift-off.

4.6 Improved Induced Gaps in InSb Nanowires

In this section, we will show the improved induced gaps from optimized recipes. For device A, we used recipe 1 (see appendix A), which relies on sulfur passivation and gentle sputter cleaning to remove the native oxide from the nanowire. The sulfur passivation uses a 1:500 diluted $(NH_4)_2 S_x$ water solution. A 10 seconds gentle sputter cleaning with a power of 20 watt under 10 mbar argon pressure is applied to further clean the nanowire in situ. After that, 5 nm evaporated Ti, 5 nm sputtered NbTi and 120 nm sputtered NbTiN were deposited in sequence. Fig. 4.5(b) shows the scanning electron microscope (SEM) image of the device A. We used a global back gate to create a tunneling barrier between the two superconducting contacts and characterized the device with tunneling spectroscopy.

As presented in Fig. 4.5(a), differential conductance scan as a function of bias voltage and the global back gate (BG) voltage reveals plentiful features. At the open regime when BG $>$ 2V, multiple conductance peaks appear at finite bias and are symmetric regarding zero bias. We attribute those features to multiple Andreev reflection between the two nanowire-superconductor interfaces. As described in chapter 2, Andreev reflection could happen when an electron at energies less than the superconducting gap enters a superconductor from a normal state material. The incident electron forms a Cooper pair in the superconductor with the retroreflection of a hole, which has opposite spin and velocity to the incident electron. Multiple Andreev reflection could happen when there are two semiconductor-superconductor interfaces. As shown by the sketch in Fig. 4.6(b), electrons could be reflected several times between the two interfaces which results in extra conductance peaks within the superconducting gap. In Fig. 4.6(a), a zoom-in scan of the open regime in device A shows the symmetric conductance peaks due to multiple Andreev reflection and we identified peaks at Δ and $2\Delta/3$ as the results of multiple Andreev reflection.

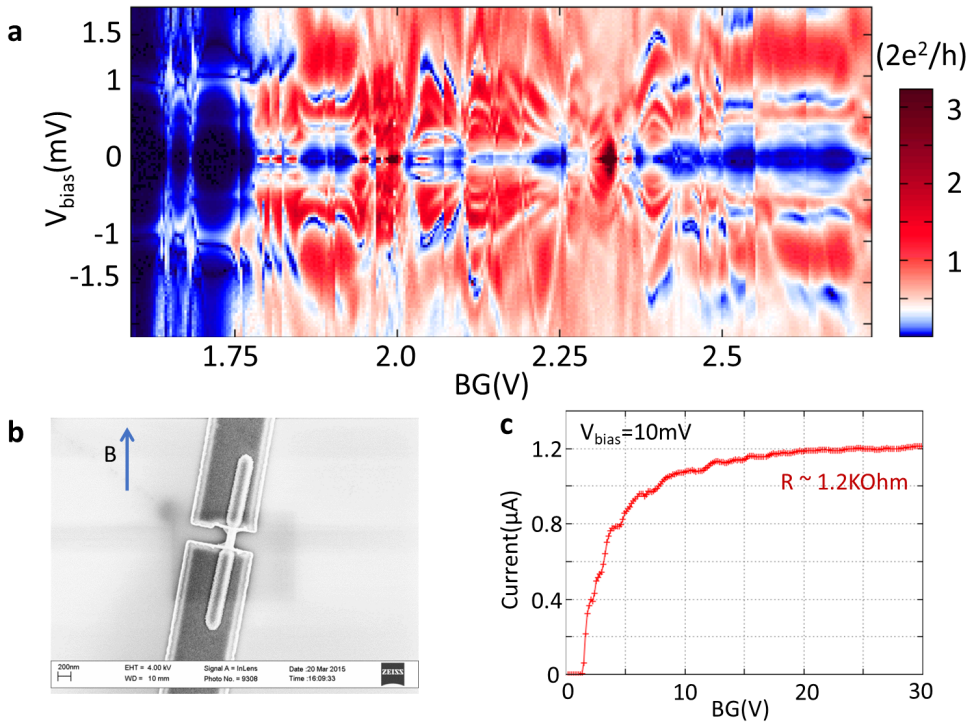

Figure 4.5: **Results from device A. a**, Differential conductance as a function bias voltage and BG voltage. In the open regime, Multiple Andreev reflection results in multiple peaks within the energy gap. Near the pinch off regime, hard induced gaps appear accompanied by Coulomb peaks. **b**, SEM image of device A. **c**, pinch off trace shows a smooth pinch off and a saturated resistance of 1.2 kΩ.

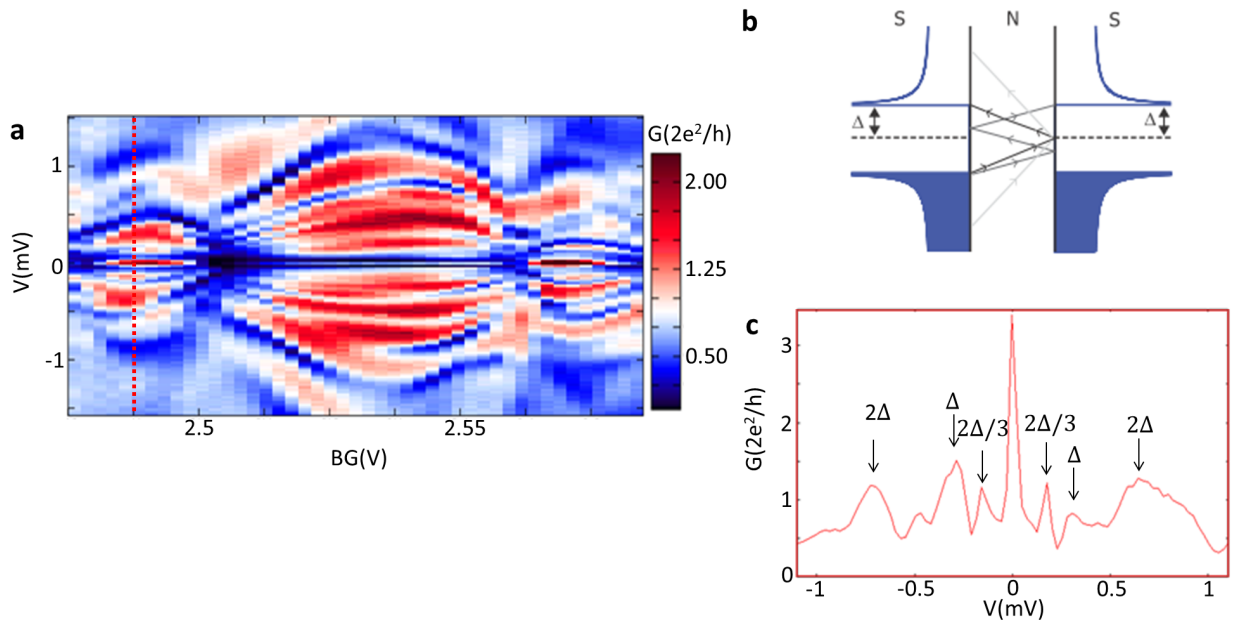

Figure 4.6: **Multiple Andreev reflection in device A. a**, Zoom in scan on the multiple Andreev reflection features. As the results of Multiple Andreev reflection, symmetric conductance peaks regarding zero bias appear within the gap. **b**, Sketch of Multiple Andreev reflection. **c**, Bias linecut taken from panel **a** at the red dashed line. Resonance peaks due to Multiple Andreev reflection are indicated by black arrows.

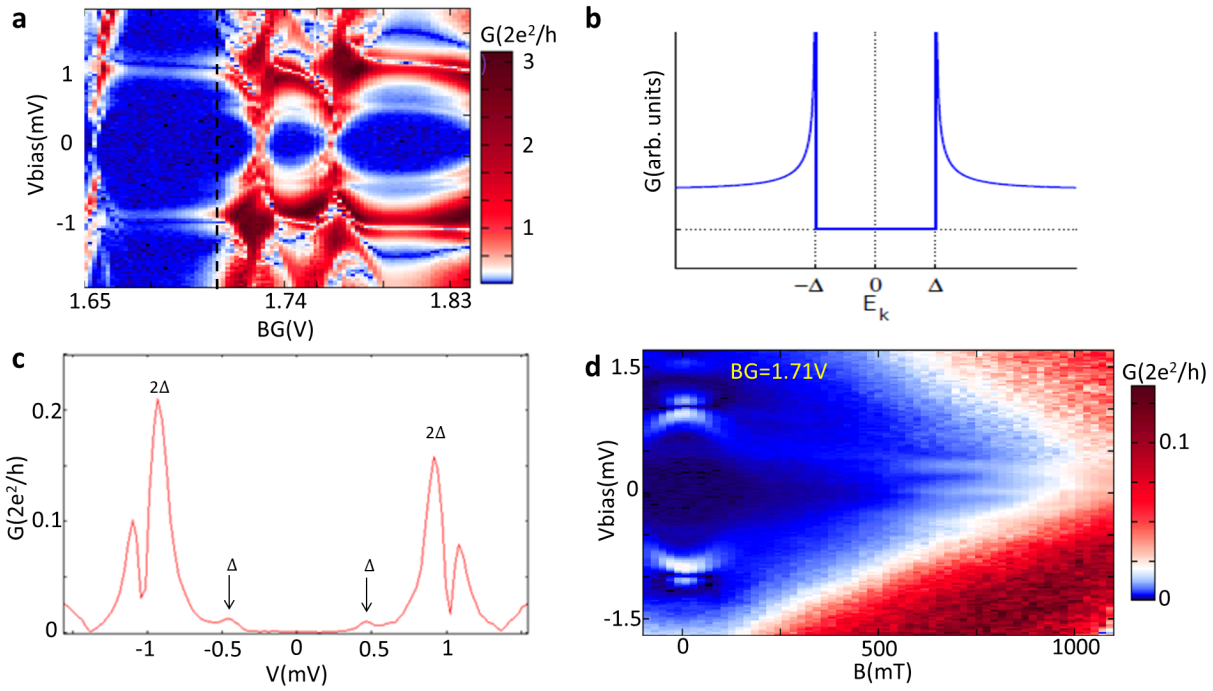

Figure 4.7: **Hard induced gaps in device A. a**, Zoom in scan of the near pinch off regime of device A. **b**, ideal BCS superconducting gap.**c**, bias linecut taken from panel **a** along the black dashed line. The magnitude of the gap is about 500 μeV. **d**, Field dependence of the induced gap at BG = 1.71 V, which shows induced gap remains open to at least 0.5 T.

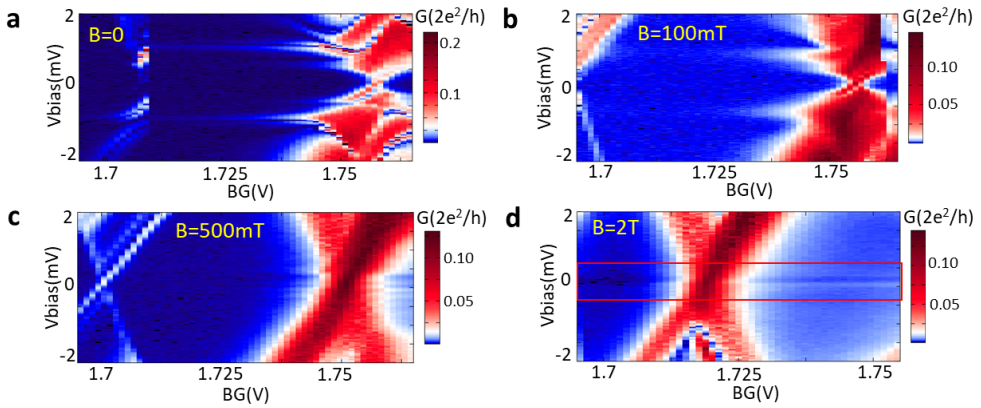

Figure 4.8: **Extended field dependence of the induced gap.** While the hard gap only appear at low fields and becomes invisible around 0.5 T, a tiny gap remains visible even at 2 T.

In BG $<$ 1.8 V regime, a hard induced gap appears and accompanied by quantum dot features (Fig. 4.7(a)). As can be seen from the linecut (Fig. 4.7(b)) taken at BG = 1.71 V, the magnitude Δ of the gap is about 500 μeV and the conductance is suppressed by more than 100 times inside the gap comparing to outside the gap, indicating a low density of states within the gap and very strong coupling between the nanowire and the superconductor. The gap also exhibits a U-shape with sharp edges that are similar to an ideal BCS gap (Fig. 4.7(b)). Within the gap, two additional peaks appear at $+\Delta$ and -Δ, indicating a non-zero density of states within the gap. Near BG = 1.74 V, loops that similar to the Andreev bound states in a quantum dot appear between two Coulomb peaks. Since we are using a global back gate to create the tunnel barrier, quantum dots are common near the pinch-off regime. The coulomb peaks can be seen more clearly in scans with a larger bias voltage (Fig. 4.9(a)).

In Fig. 4.7(d), we present the magnetic field dependence of the induced gap in device A. The magnetic field is applied within the plane of the sample substrate and with a 15° angle regarding the nanowire. As we can see, the strong gap edges gradually shrink with the increasing magnetic field. The hard induced gap only appears at low fields and becomes soft above 0.3 T. It is worth noting that the gap does not fully close even above 0.5 T. In some BG regimes, a tiny gap remains visible even at 2 T as shown in Fig. 4.8.

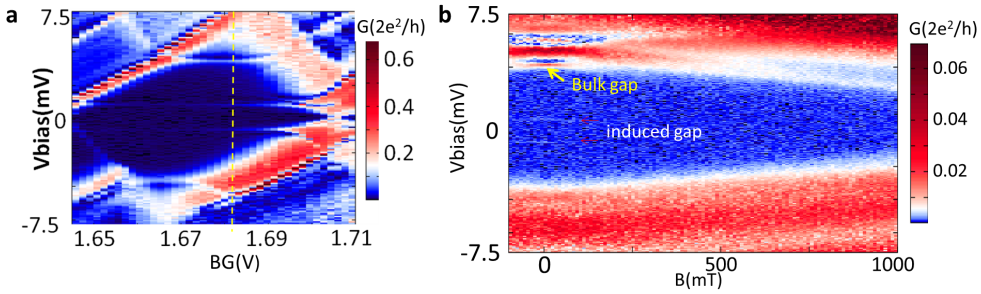

Figure 4.9: **Bulk gap of NbTiN. a**, Bulk gaps are observed within the Coulomb diamonds with amagnitude of 5 mV. Yellow dashed line indicates the BG setting for panel **b**. **b**, Field dependence of the bulk gap shows the gap remains hard to above 1T.

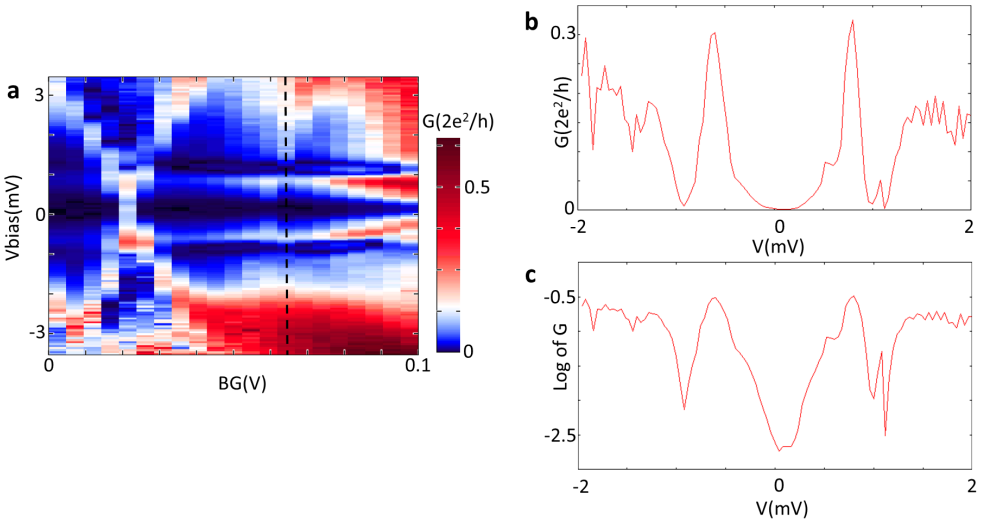

Figure 4.10: **Induced gaps in device B. a**, Differential conductance scans as a function of bias voltage and BG voltage. **b**, Linecut taken from panel **a** along the black dashed line. The induced gap shows a desired U-shape. **c**, Logarithm of the panel **b**.

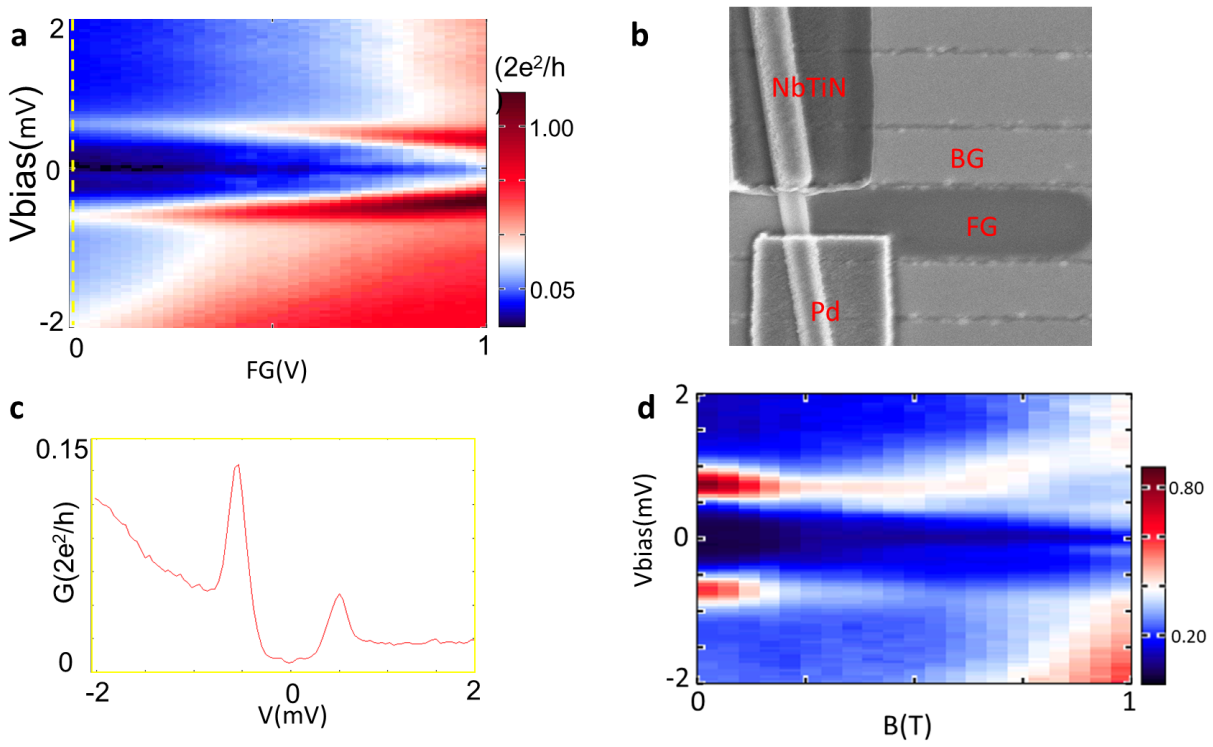

Figure 4.11: **Induced gaps in device C. a**, Differential conductance scans as a function of bias voltage and BG voltage shows a hard and uniform gap. **b**, SEM image of the device C. **c**, Lincut taken from panel **a** at FG = 0 V. **d**, Mangetic field dependence of the induced gap in device C. The gap persists to above 1 T.

With the help of the Coulomb blockade, which suppresses the conductance within the Coulomb diamonds regime, we also observed a much larger gap that could be the bulk gap of NbTiN (Fig. 4.9). That gap has a magnitude of 5 mV and persist to much bigger field.

In device B and C, which used recipe 2 (see appendix A for details), which is modified to etch slightly more of the nanowire due to the concern that the top layer of the nanowire may have degenerated after oxidation reaction and is based on [45].

Device B is a two-terminal device that has a similar configuration to device A. A global back gate is used to tune the chemical potential inside nanowire and create tunnel barrier. The resulting induced gaps is shown [Figs. 4.10(a)(b)] shows a U-shape with the magnitude Δ = 500 μeV. By taking Logarithm of the differential conductance, we can see the conductance is suppressed by over 100 times inside the gap compared to the conductance outside the gap (Fig. 4.10(b)).

We also tested the recipe 2 in a hybrid Majorana device (device C Fig. 4.11(b)), which has both normal contact and superconducting contact. The same recipe has been used for both normal and superconducting contacts. While the first time sulfur passivation may leave some residue on the nanowire and thus may affect the contact made later, we found a gentle sputter cleaning could clean the residue and the sequence of making normal and superconducting contacts does not affect the quality of the contacts. Without the gentle sputter cleaning, however, we found the contact made later usually has poor quality indicated by large low temperature resistance (>8 kΩ). The nanowire of device C was placed on local bottom gates to get better control of the tunneling barrier. The induced gap in device C near the pinch-off regime also shows U shape with highly suppressed conductance within the gap(Figs. 4.11(a)(b)). More importantly, the magnetic field dependence of that gap(Fig. 4.11(d)) is better than what we have in device A. The gap remains open to at least 1 T, which gives us more freedom to search for the signal of Majorana zero modes.

It is worth noting that we also observed NbTiN bulk gap (Fig. 4.12) in some testing devices, where we did not use the angle deposition technique. In those devices, we believe the NbTiN film (90 nm) is not thick enough to cover the gap as discussed in Section 4.5. As a result, tunnel barriers were formed between the two parts of the NbTiN films. bias voltage thus mostly drops on that junction instead of the nanowire. Consequently, those devices

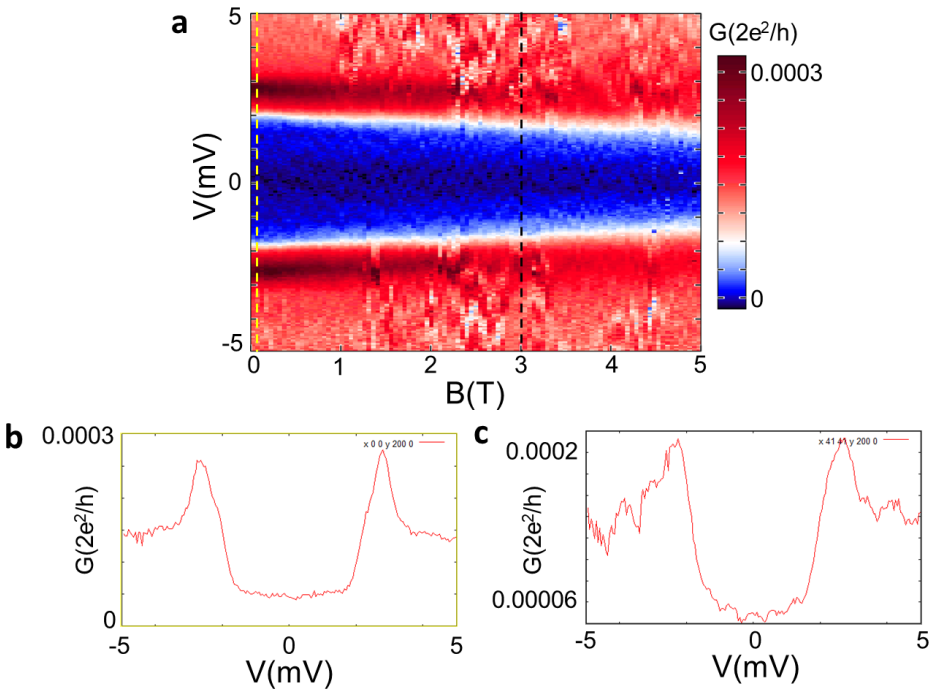

Figure 4.12: **Bulk gaps in a device with tunnel junctions between NbTiN films. a**, Field dependence of the bulk gap. **b and c**, field linecuts taken from panel **a** at 0 T and 3 T respectively.

showed very high resistance and limited gate effect. Field dependence of that bulk gap is presented in Fig. 4.12(b). As we can see, the bulk gap has a magnitude of 1.25 meV at zero field and remains hard and open to at least 5 T.

In summary, we developed two recipes based on combinations of sulfur passivation and gentle sputter cleaning. recipe 1 and recipe 2 can both result hard induced gaps in InSb nanowires. Due to recipe 2 generally gives a higher yield of hard gaps and works better in hybrid devices, we used it for the experiments in chapter 6. For the experiments in chapter 5, which had been done before recipe 2 was developed, we used recipe 1.

4.7 Conductance Quantization in Quantum Point Contacts

When measuring the conductance of a quantum point contact, each spin degenerate subband gives a conductance of $G_0 = \frac{2e^2}{h}$ if the transport is ballistic, meaning the probability for transmitting is unity. While it is relatively easy to see conductance quantization in gate defined quantum point contacts in two-dimensional electron gases (2DEG) [67, 68], quantized conductance in one-dimensional nanowires is more challenging to achieve. In a quasi 1D nanowire, impurities and imperfections in the crystal lattice, inhomogeneities due to surface states, and Schottky barriers between nanowires and metals could all result in backscattering of electrons that smears out the quantized conductance plateaus. With magnetic field, backscattering on defects that causes interference minima and maxima in conductance and obscures plateaus is suppressed. As the result, quantized conductance in nanowires can be more easily observed at high fields [69]. With further improved surface cleaning recipe, conductance quantization has also been reported at zero field with normal contact material [50]. Due to the requirement of ballistic transport, conductance quantization is a good criterion to evaluate the quality of the nanowires and nanowire-metal interfaces. With our improved contact recipes 2, we observed quantized conductance in both two-terminal and three-terminal hybrid devices in three devices.

As presented in Fig. 4.13, we observed quantized conductance at zero magnetic field in a two-terminal device D using recipe 2. The nanowire is contacted by two superconducting contacts, which consist of 5 nm NbTi and 60 nm NbTiN film sputtered at a 60° angle. The contact spacing is around 300 nm and the chemical potential inside the nanowire is controlled by a global back gate. Fig. 4.13(a) plots the differential conductance as a function of the global gate voltage and bias voltage at zero field. While two plateaus are visible, the measured differential conductance is lower than the quantized value. We attribute that to the existence of the contact resistance from the nanowire-superconductor interface. Typical contact resistance can range from 2-6 kΩ and usually insensitive to electrostatic gates [50]. This problem also happens in other similar experiment and people usually fit the measured conductance to quantized value based on the observed plateaus [50].

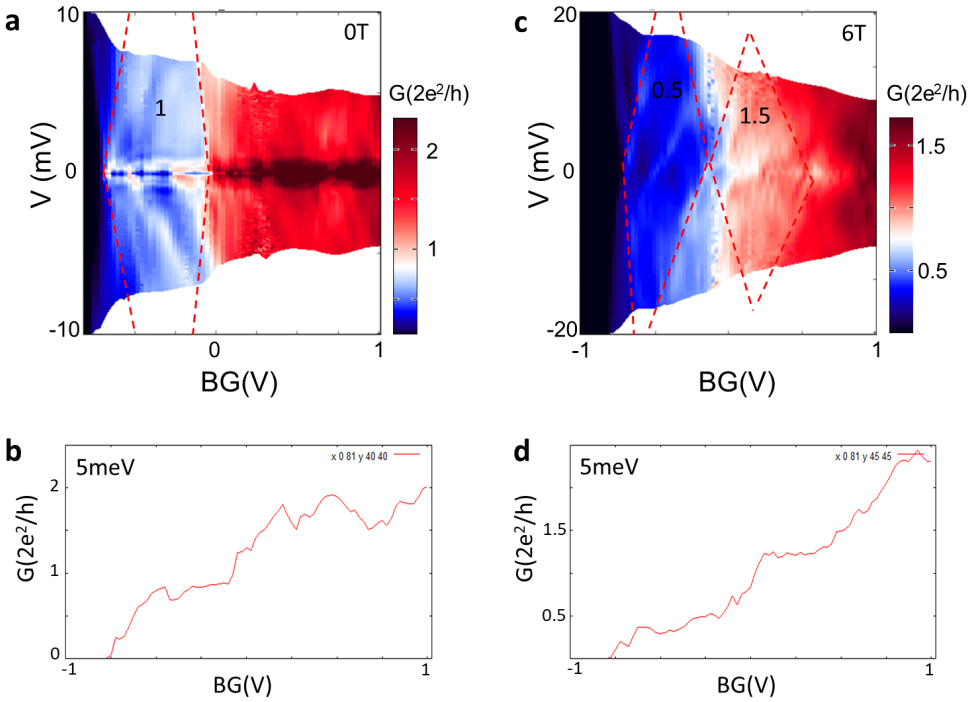

Figure 4.13: **Conductance quantization in device D. a**, Differential conductance scans as a function of bias voltage and BG voltage at zero magnetic field. The red dashed lines indicate the region with flat conductance plateau. **b**, Bias linecut taken at 5 meV from panel **a**. **c**, Differential conductance scans as a function of bias voltage and BG voltage at 6 T. The red dashed lines indicate the region with flat conductance plateau. **d**, Bias linecut taken at 5 meV shows two conductance plateaus. The mismatch between the conductance of the plateaus and quantized value is due to the presence of contact resistance.

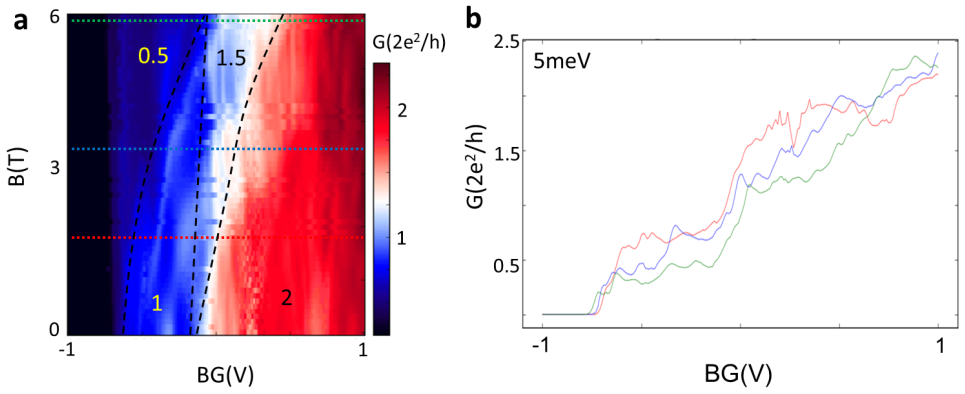

Figure 4.14: **Field evolution of the conductance plateaus.** **a**, Differential conductance scans as a function of magnetic field and BG voltage at zero bias voltage. The G_0 plateau split into 0.5 G_0 and 1.5G_0 with increasing fields. **b**, Field linecuts taken from panel **a** at 1.5 T (red curve), 3.2 T (blue curve) and 6 T (green curve) show the development of half integer plateaus.

Since conductance is quantized when the two leads occupy the same subband, diamond shape regions appear with relatively flat conductance (indicated by red dashed lines in Figs. 4.13(a)(c)). With recognizable diamond regions, it is possible to identify subband-resolved transport even if quantization is not clearly visible due to residual scattering.

At zero magnetic filed, only integer conductance plateaus exist. After a field of 6T is applied in parallel to the nanowire, half-integer conductance plateaus fully developed as the magnetic field breaks the time-reversal symmetry and lifts spin degeneracy of subbands (Fig. 4.13(c)). The full evolution of the conductance plateaus is shown in Fig. 4.14. While set bias voltage to 5 meV, differential conductance is measured as a function of global gate voltage and magnetic fields. As the magnetic field lifts the spin degeneracy, the G_0 and $2G_0$ plateaus split into 0.5 G_0, G_0, 1.5G_0 and $2G_0$ plateaus.

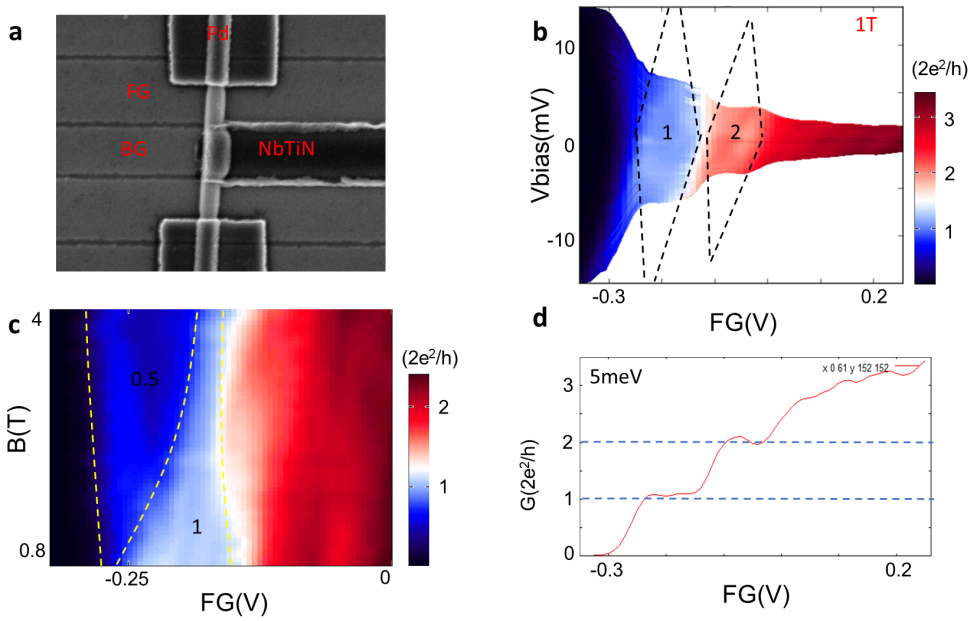

Figure 4.15: **Conductance quantization in device E. a**, SEM image of device E. **b**, Differential conductance as a function of bias voltage and FG voltage at 1 T. The quantized conductance regions are indicated by black dashed lines. **c**, Field evolution of the conductance plateaus. The $0.5G_0$ plateau is full developed at 4 T. **d**, Bias linecut taken from panel **b** at 5 meV.

By measuring the tip of the diamond shape region with G_0 conductance in Fig. 4.13(a), we estimate the energy spacing between the first and second subband is about 15-20 meV, which is consistent with the previous results in InSb nanowires [69, 50]. We also extract the lever arm η of the global back gate to be $\frac{15-20meV}{0.6V}$ using the relation $\eta \mathrm{V_{gate}} = \Delta \mathrm{E_{subband}}$.

In three-terminal hybrid devices with one superconducting contact in the middle and two normal contacts at the ends, the quality of the contact is supposed to be lower as more fabrication steps are involved. However, we still observed clear quantized conductance in one of such hybrid devices (Device E). The device E is fabricated using the same recipe (recipe 2 in appendix A)of the device D . The normal contact was made after the superconducting contact with 10 nm Ti and 120 nm Pd. As shown in Fig. 4.15, G_0 and $2G_0$ plateaus emerge at finite fields and we extract the energy spacing between the first and second subband to be 15 meV. The splitting of the subbands with magnetic fields is presented in Fig. 4.15(c). As the Zeeman splitting is giving by $E_{\mathrm{Zeeman}} = g\mu_B \mathrm{B}$, where μ_B is the Bohr magneton and g is the Landé g-factor, we extract a g-factor of 50-55 with the magnetic field in parallel to the nanowire. It is worth noting that the contact resistance from interfaces is much smaller here comparing to device D, resulting the conductance plateaus to be closer to the quantized values.

4.8 Conclusions

In conclusion, we have developed robust contact recipes for InSb nanowires. By optimizing the etching process, contact deposition methods, and wetting layers, transparent interfaces have been achieved with both normal and superconducting contact materials. Quantum point contact and Andreev reflection, which signal the high transparency of the nanowire-metal interface, have been observed. Hard induced gaps have also been observed in different kinds of devices. The induced gap remains open to at least 1 T in devices fabricated using recipe 2, giving us enough freedom to study for Majorana bound states and other excited states at finite fields. We notice hard induced gaps can also be achieved with thin Al film (∼10 nm) on InAs and InSb nanowires using selective-area epitaxy and shadow mask

technique [70, 59, 71]. Since the epitaxy is in-situ, the Al-nanowire interface is free of native oxide and results in ballistic transport and hard induced gaps. While the in-plane critical field is high for thin Al film, its low out-plane critical field limits the study of field angle dependence of Majorana bound states. Recently, tin film has also been epitaxial grown on InSb nanowires and produced promising results [72]. More new techniques and new materials may provide better platforms in the future.

5.0 Tunneling Spectroscopy in Two-Terminal Devices

5.1 Introduction

Majorana fermions could emerge as quasi-particles in a superconductor possessing non-trivial properties including pinning to zero energy, quantum state delocalization and non-abelian statistics [14, 13, 7]. They have generated great interest in recent years due to their potential to be used as the building block of a fault-tolerant quantum computer [6, 7]. In this chapter, we present our results from two-terminal measurement. To further study possible Majorana zero modes (MZM) signal and distinguish MZMs from other mechanisms, we fabricate two-terminal superconductor-semiconductor hybrid nanowire devices. With enhanced electrostatic coupling of gates to the nanowire and improved nanowire-metal interface, we find ZBCPs possibly due to overlapped MZMs and establish a experimental phase diagram of the ZBCPs. Splitting behavior and magnetic field anisotropy of ZBCPs are also observed. While those observations are consistent with Majorana theories, non-Majorana ZBCPs are observed as ubiquitous features in superconductor-semiconductor hybrid devices as the results of inhomogeneity in the system. Although devices with further improvement in gate configuration and nanowire-metal interface provide a clearer picture of ZBCP and its magnetic field evolution, we claim it is difficult to unambiguously distinguish MZMs from other mechanisms in a two-terminal measurement, as those mechanisms also generate very similar ZBCPs at finite fields.

5.2 Majorana Signal in Two-Terminal Measurements

As discussed in chapter 2, generating Majorana zero mode (MZM) needs four ingredients [10, 11]: a one-dimensional quantum wire, with spin-orbit interaction, and induced superconductivity,under external magnetic field B. MZMs arise as zero energy states one at each

end of the topological regime once the topological phase condition is satisfied:

$$E_Z > \sqrt{\Delta^2 + \mu^2} \tag{5.1}$$

where $E_Z = g\mu_B B$ is the Zeeman energy, with g the effective Landé g-factor, μ_B the Bohr magneton. Δ is the induced superconducting gap at $B = 0$, and μ is the chemical potential in the quantum wire, with $\mu = 0$ set to coincide with the lowest energy of a one-dimensional subband at $B = 0$. A closing of the induced gap at $E_Z = \sqrt{\Delta^2 + \mu^2}$ manifest the transition between trivial phase to topological phase and MZMs should be robust as long as the topological phase condition Eq. 5.1 is maintained. Despite the zero charge and energy property, MZMs can be detected by tunnel spectroscopy as midgap zero bias conductance peaks (ZBCPs) [37, 73].

It is worth noting that the signal of Majorana, i.e. ZBCPs, from a pair of well separated Majorana is predicted to be quantized at exactly $2e^2/h$ [73, 37, 74] at zero temperature. In realistic systems with finite size and finite temperature, an approximate quantized ZBCP may still observable if tunnel coupling dominates over both temperature and Majorana splitting[1].

Following the prescription [10, 11], the first several experiments focused on Majorana bound states in hybrid superconductor-semiconductor nanowire devices showed some anticipated phenomenon [12], i.e. zero bias conductance peaks appearing at finite magnetic fields in tunneling spectroscopy, with reasonable controlling gate dependence and magnetic field angle dependence.

While the early observations are generally consistent with the Majorana theories, discrepancies and missing parts do exist, which include: (I) Missing of gap closure and reopening, which indicate the topological quantum phase transition. (II) Missing of quantized ZBCPs. (III) Oscillatory behavior of ZBCPs due to MZMs interaction is not observed. (IV) No established topological phase diagram, which makes it possible to predictably tune nanowire segments in and out of the topological phase.

The first three missing parts, which are special features of topological phase or MZMs, prevents an unambiguous prove of the existence of MZMs, while knowledge of the topological

phase diagram allow us to control the positions and couplings of multiple Majorana bound states.

Apart from those missing predictions, other mechanisms that could also give rise to ZBCPs at finite magnetic fields also put a stop to a definitive conclusion of the existence of MZM. Those include Andreev bound states [75], the Kondo effect [76], weak antilocalization [77], disorder-induced ZBCPs, and fine-tuned so-called 'class D' peaks [78]. Among those effects, trivial Andreev bound states and 'class D' peaks are particular difficult to be distinguished with as they can mimic many signatures of well-separated Majorana bound states [41, 79, 80, 81, 82, 38, 83, 77, 84, 85]. Even quantized zero-bias conductance peaks, once believed to be unique to MZM, are shown to be ubiquitous in superconductor-semiconductor hybrid systems [39, 82].Those effects, when acting by themselves or combining together, generate similar ZBCPs at finite fields and thus cause great difficulty in distinguishing them from Majorana originated ZBCPs.

5.3 Experimental Phase Diagram of Zero-bias Conductance Peaks

This work is published in Science Advances [86] in collaboration with Chen, J., Stenger, J., Hocevar, M., Car, D., Plissard, S. R., Bakkers, E.P.A.M., Stanescu, T. D., Frolov, S.M..

Among those missing parts about MZM mentioned in the previous section, an important one is the topological phase diagram, which gives us the ability to predictably tune nanowire segments in and out of the topological phase. This ability is a prerequisite for Majorana braiding, an experiment that could demonstrate Majorana's non-abelian property and realize topological quantum bits [87, 88]. Motivated by that, we fabricate hybrid InSb nanowire devices using the methods described in the recipe 1 in appendix A. Our efforts mainly focus on two aspects. First, enhancing the electrostatic coupling between bottom gates and the nanowire with the use of a thin layer of high-κ gate dielectric (HfO_2, 10 nm) . That enhancement may enable us to tune the nanowire-superconductor hybrid region (hybrid region) into few or single subband regime, where most of the early theoretical models are valid and the topological phase diagram is simpler. Second, improving contact recipe to

yield transparent nanowire-metal interfaces and thus hard induced superconducting gaps.

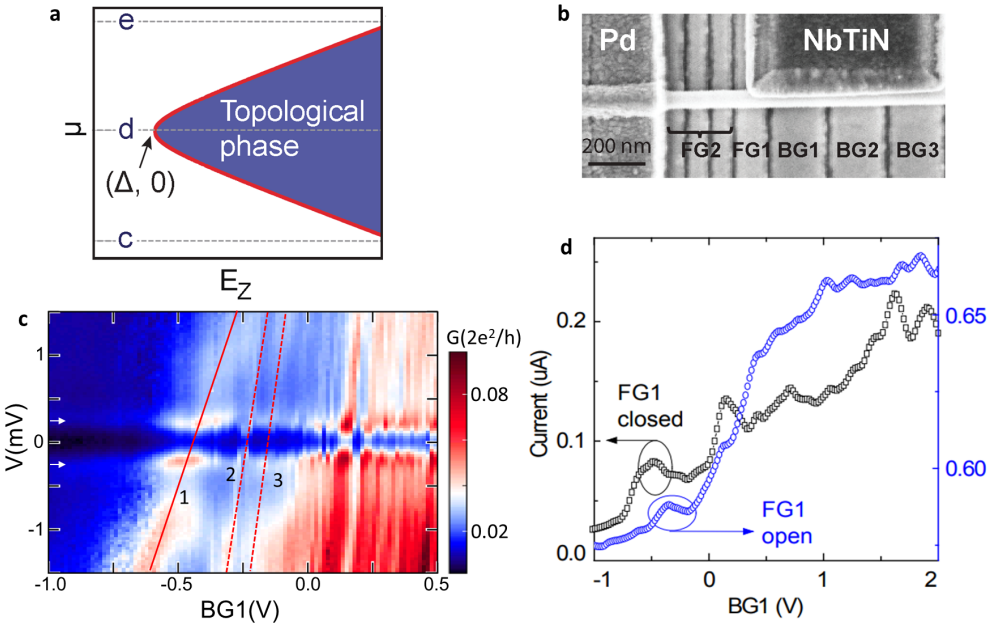

Figure 5.1: **Quantized one-dimensional subbands levels in device D. a** , Topological phase predicted by equation.5.1. **b**, SEM image of device A. **c**, Scan of differential conductance as a function of $BG1$ voltage and bias voltage at zero magnetic field. The first resonance is indicated by the red solid line. Red dashed lines indicate the second and the third resonance. Dispersion of the first and second resonances are 10 meV/V and 25 meV/V, respectively. **d**, $BG1$ traces at zero magnetic field while $FG1$ is set to open(blue) and close(black). Circles indicate the positions of the first crossings.

The studied device here is referred as device A, which has a superconducting NbTiN contact to induce superconductivity, and a normal metal Pd contact to perform tunneling spectroscopy by varying bias voltage V between normal and superconducting contacts (Fig. 5.1(b)). For that device, both magnitude and direction of field B can be controlled, as B should be pointed away from the direction of the effective spin-orbit field in order to induce MZMs. The induced superconducting gap Δ in 5.1 is set by the NbTiN/InSb interface transparency, the NbTiN film as well as by the electronic band structure in the nanowire. We treat Δ as a fixed parameter. Chemical potential μ in the nanowire is tunable with local

gate electrodes placed underneath the nanowire. We adjust voltage on gate $FG1$ to create a tunneling barrier between normal and superconducting sides. Gate $BG1$ located next to the tunneling barrier and underneath the superconductor is used to vary the chemical potential in the nanowire segment under investigation.

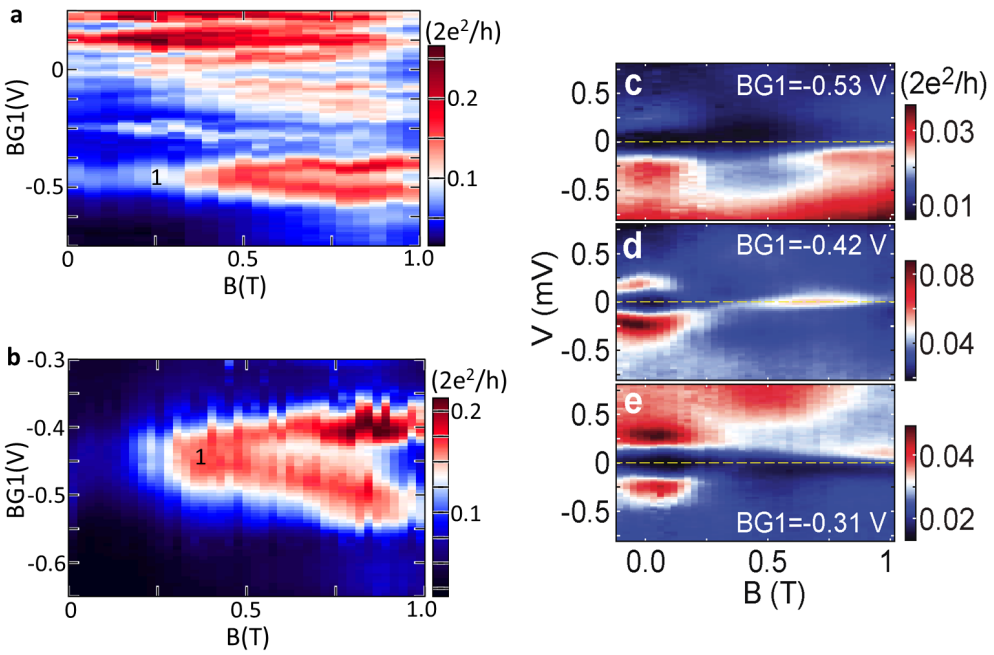

Figure 5.2: **Resonances splitting and ZBCPs controlled by BG1 voltage. a and b**, differential conductance maps as functions of BG1 voltage and magnetic field. The magnetic field is in parallel to the nanowire main axis. The first crossing exhibits clear splitting with a g factor of 40. **c-e**, differential conductance maps in bias voltage V vs. magnetic field B at three different settings of BG1

As a general observation, gate $BG1$ shows a strong coupling to the nanowire as it can almost pinch off the tunneling conductance (Fig. 5.1(d)). With a tunnel barrier created by $FG1$, we notice the bias voltage vs. $BG1$ scan at zero magnetic field reveals a series of resonances that extend both inside and outside the induced gap(Fig. 5.1(c)). The left-most resonances (indicted by red line) is referred as the first resonance as there is no more apparent resonance at lower $BG1$ voltage. And two following resonances are labeled as 2 and 3 as indicated by the red dashed lines. It is worth noting those resonances split with

magnetic fields (Fig. 5.2(a)) and the first resonance exhibits a g-factor of 40 (Fig. 5.2(b)).

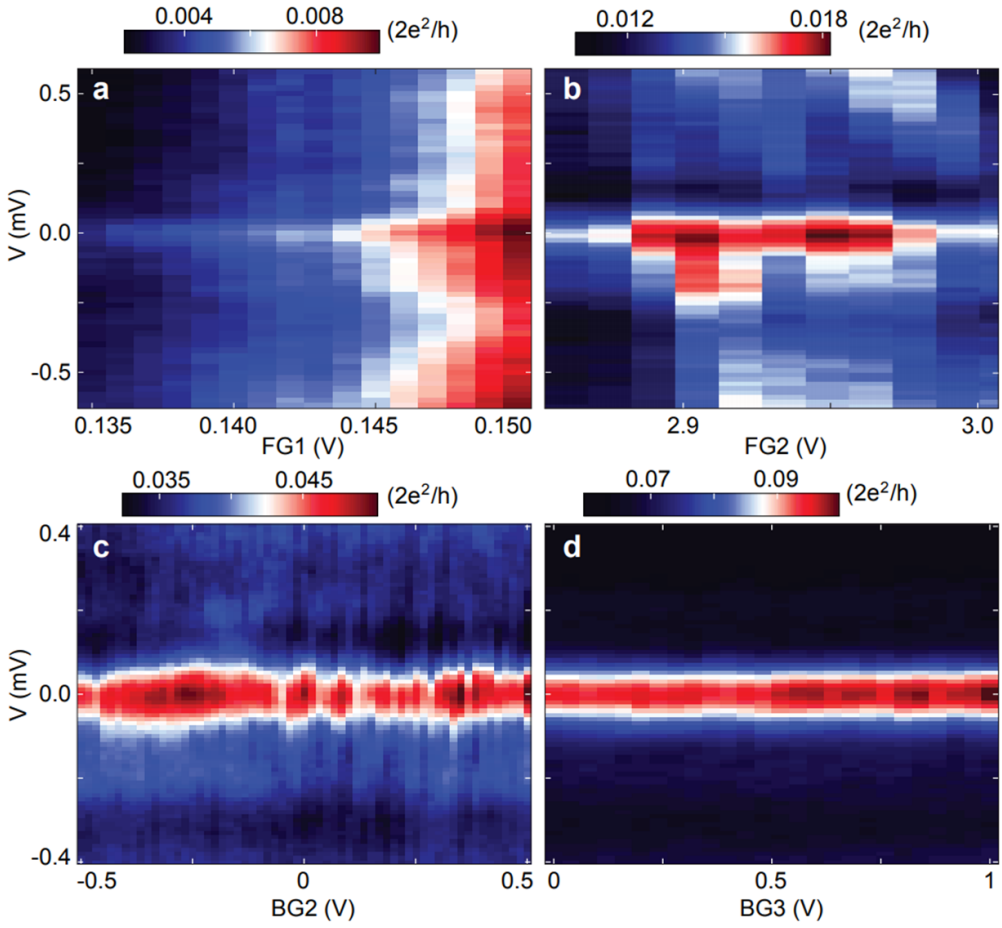

Figure 5.3: **Gates dependence of the ZBCP in device A. a-d**, at fixed magnetic field B=0.5 T and BG1=-0.42 V, conductance maps are plotted in bias vs. barrier gate FG1, gate FG2 at the normal side as well as big gates BG2 and BG3 under the superconductor.

We first demonstrate the ability to generate or eliminate a zero-bias conductance peak (ZBCP) in conductance over a wide range of B by switching voltage on gate $BG1$ around the first resonance. Figs. 5.2(c)-(e) present scans of bias voltage versus magnetic field applied along the nanowire at three different $BG1$ voltages. The scan obtained at $BG1 = -0.42$ V (Fig. 5.2(d)) shows a ZBCP persistent in magnetic field up to $B = 1$ T. When $BG1$ is changed by ± 0.11 V (Figs. 5.3(c),(e)), only a gradual closing of the induced gap is observed, with no subgap states up to 1 T. Thus, Figs. 5.2(c)-(e) constrain the ZBCP phase diagram (horizontal lines in Fig. 5.1(a)). The ZBCP shows no significant dependence on other gates ($FG2$, $BG2$ and $BG3$) as shown in Fig. 5.3, which indicates ZBCP is from quantum states located in the nanowire above $BG1$.

In Fig. 5.4 we present the emergence and the evolution of the zero bias peak within the phase space identified in Fig. 5.3(c)-(e). At zero field, a bias vs. gate scan exhibits an induced gap $\Delta = 0.25$ meV (Fig. 5.4a). We assign conductance maxima at $V = \pm 0.25$ mV and around $BG1 = -0.4$ V to an increase in the density of states at the bottom of a one-dimensional subband. At $B = 0.25$ T (Fig.5.4(b)) the apparent gap decreases but the regime remains qualitatively similar to that at $B = 0$ T. We point out that all bias vs. gate data from this device is asymmetric in bias. Namely, resonances that shift to more positive bias voltage with more positive gate voltage dominate. This effect is frequently observed in nanowire devices[12, 41], and we attribute this effect to the tunneling barrier asymmetry [89].

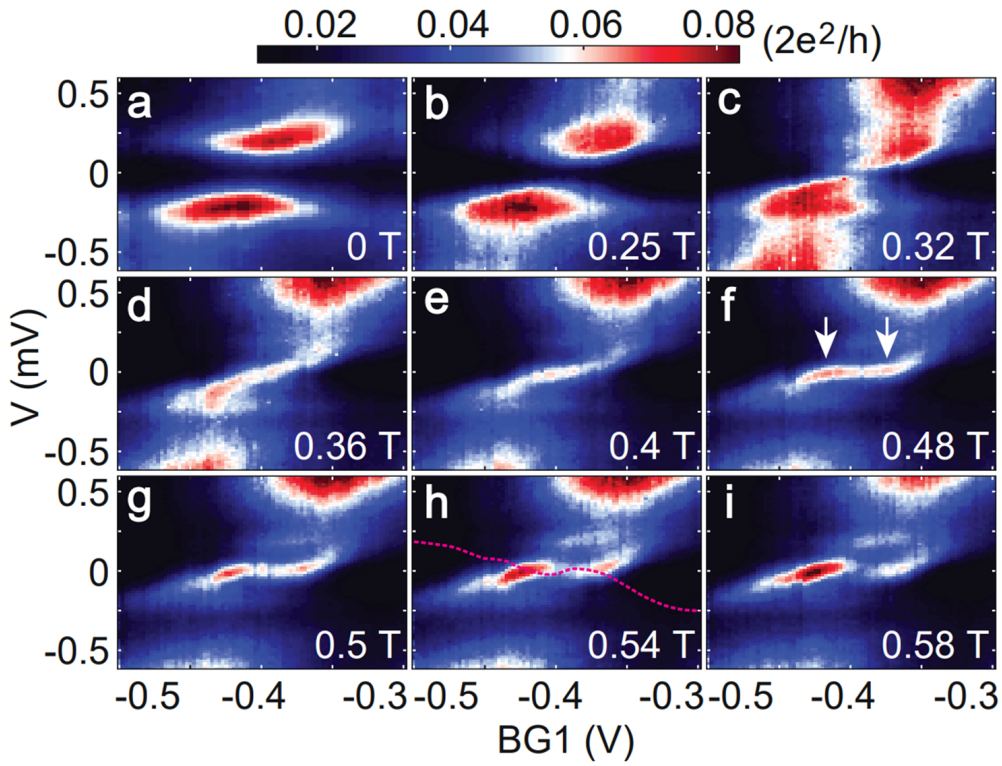

Figure 5.4: **The emergence and evolution of the ZBCP at finite fields. a-i**, conductance maps in bias voltage V vs. BG1 at different magnetic fields indicated in the lower right corner of each panel. Arrows in panel **f** mark the ZBCP onset gate voltages plotted in Fig.5.6. The dashed line in panel **h** is obtained by tracing the visible maximum in subgap conductance and flipping the resulting trace around V=0.

At $B = 0.32$ T (Fig. 5.4(c)), conductance within the induced gap is increased in the center of the $BG1$ range, giving an indication of a closing gap at $BG1 = -0.4$ V. According to theory behind Eq. 5.1, the gap should close around $\mu = 0$ at the topological phase transition. At $B = 0.36$ T a well-defined conductance resonance crosses zero bias and extends across the gap (Fig. 5.4(d)). The resonance appears to stick to zero bias in a widening range of $BG1$ at higher magnetic fields (Figs. 5.4(e)-(f)). Towards the edges of each $BG1$ scan, the conductance peak strongly deviates from zero bias and gradually merges into the apparent induced gap. At the boundary defined by Eq. 5.1, Majorana bound states at the opposite ends of the topological segment of the nanowire grow in length and strongly overlap because of the finite length of the segment. This overlap of the two MZMs leads to the MZM energy deviating from zero[90, 83, 35, 91, 92].

In addition to the strong deviations from zero bias at the phase boundaries, we observe that for $B \geq 0.5$ T (Figs. 5.4(g)-(i)) the peak wavers away from zero bias near the center of the scans. Particle-hole symmetry in the superconductor dictates that the energy spectrum within the gap must be symmetric with respect to zero bias. This is not observed due to barrier asymmetry[89]. However, to propose how the full spectrum inside the gap looks, we trace a subgap resonance in Fig.5.4(h) and flip it along the zero bias line. The full spectrum obtained this way suggests that the small deviations from zero bias also originate from zero-bias peak splitting due to gate-dependent overlap of MZMs within the topological phase (see Fig. 5.8).

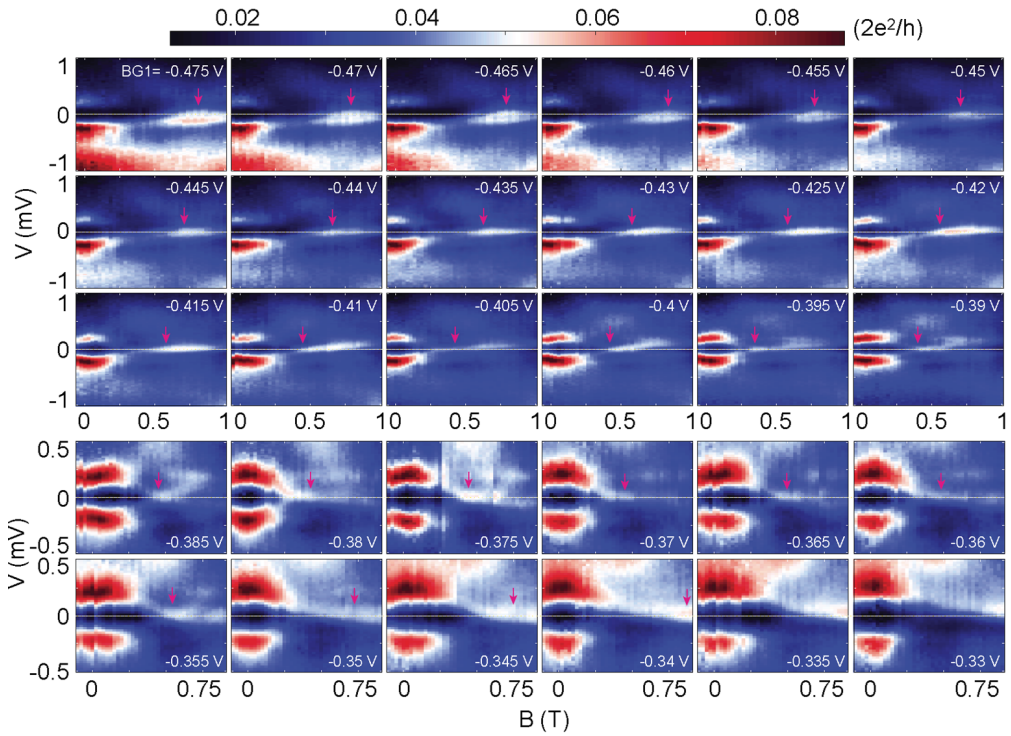

Figure 5.5: **ZBCPs evolution with BG1.** Conductance maps in bias voltage V vs. B at different BG1 indicated in the right corner of each panel. Note that, due to a charge jump, all the gate voltages of BG1 have been shifted by +0.02 V. The dashed lines mark zero bias voltage line. Arrows mark the ZBCP onset fields plotted in Fig.5.6. The onset fields are picked by judging from linecuts of bias scans where the conductance peaks first hit zero bias voltage.

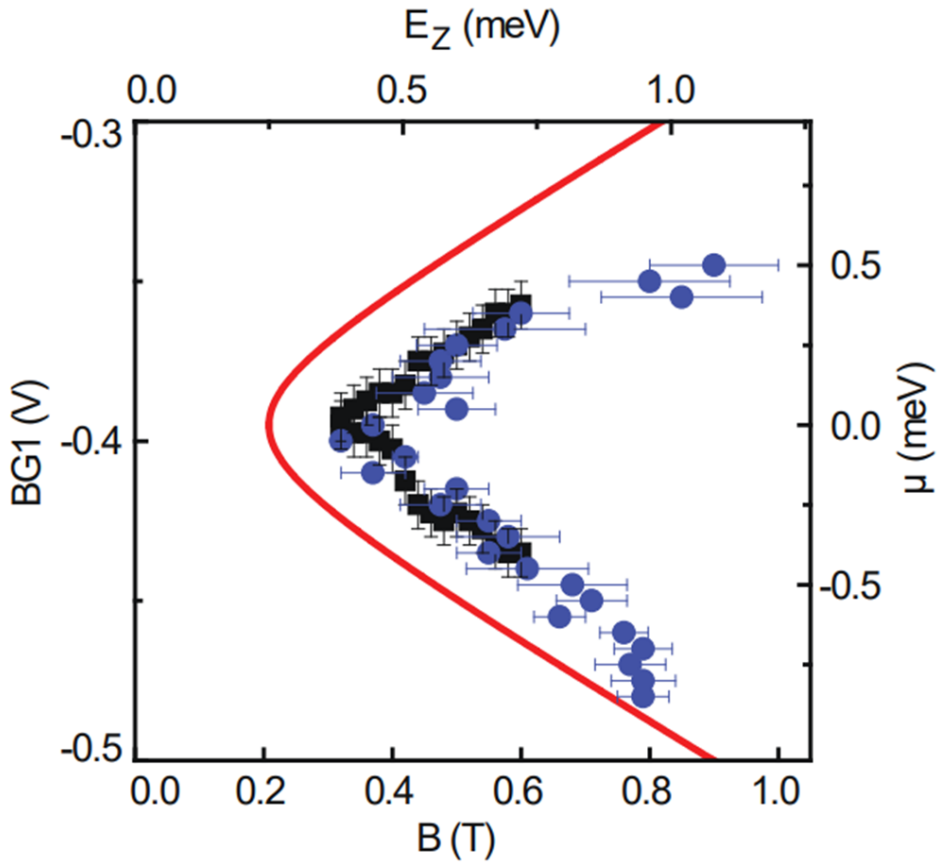

Figure 5.6: **Phase diagram of ZBCPs.** Zero-bias peak onset points are collected from data in Fig.5.4 (black squares) and Fig.5.5 (blue circles), with error bars judged by deviation of the peak from zero bias within 1/2 of the full width of half maximun of ZBCPs. Data extracted from Fig.5.5 are offset by +0.02 V in BG1 to compensate for a systematic shift due to a charge switch. The top axis E_Z is calculated from magnetic field using $g = 40$. The right axis μ is calculated from BG1 according to 10 meV/V, and set to be zero at the parabolic vertex, BG1 = -0.395 V. Eq.5.1 is plotted in solid line, using $\Delta = 0.25$ mV.

In Fig. 5.5, we scan magnetic fields along the nanowire main axis at fixed $BG1$ voltages. The magnetic fields scan direction is always from low to high fields to reduce hysteresis. As indicated by the red arrows, at $BG1$ = -0.475 V and $BG1$ = -0.33 V, the onset fields are above 0.8 T. The onset fields decrease when the $BG1$ voltages vary toward the center of the resonance and reach the lowest onset field of 0.32 T at $BG1$ = -0.4 V. Those observation confirms the finding of Fig. 5.4, which shows the topological regime, i.e. the $BG1$ region with ZBCP, grows with increasing fields.

By picking up the onset points of the ZBCPs from Fig. **??** and Fig. 5.5 and plot them together in Fig. 5.6, we mapped out a phase diagram of the topological superconductor. The two data sets obtained this way are consistent with each other and in good agreement with the square root dependence given by Eq.5.1. Based on the diagram, we identify $\mu = 0$ at $BG1$ = - 0.4 V. The minimal onset field B = 0.33 T converts into Zeeman energy of 0.4 meV (using $g = 40$), which is greater than the apparent gap at B = 0 T.

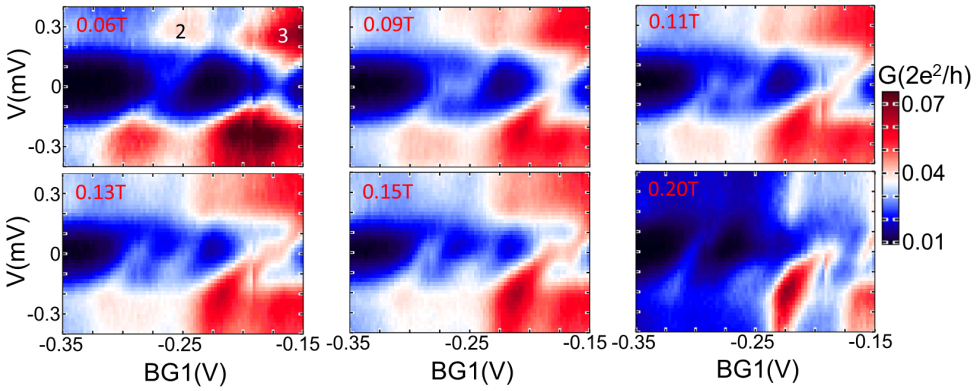

Figure 5.7: **Field evolution of the second and the third resonances.** The second and the third resonances developed near zero energy states at much lower fields comparing to the first resonance. The ZBCPs from the second and the third resonances disappear at B= 0.2 T.

However,in finite-length superconductors this is expected: due to MZM splitting at the topological transition point the ZBCP should onset at a higher field. For the same reason, ZBCP should appear in a narrower range of chemical potential around $\mu = 0$ for a fixed field. As a result, the area of the phase diagram with ZBCP present is reduced for finite-size

systems. In Fig.5.6 the theoretical phase transition line predicted by Eq.5.1 indeed encircles the extracted ZBCP onset points. It is worth noting that even for $B = 1$ T, the induced Zeeman energy ($\sim 1.2meV$) is still much smaller than the subband spacing ($\sim 10meV$), rendering the single subband topological phase condition(5.1) valid here.

The resonance which we investigate as MZM is pinned near zero bias over significant phase diagram area to the right of the onset curve in Fig. 5.6. The range of ZBCP in both chemical potential and Zeeman energy greatly exceeds the ZBP width, which is between 30 and 100 μeV. The phase diagram area with a ZBCP is strongly diminished when magnetic field orientation deviates from the nanowire main axis and approaches the spin-orbit field orientation, previously established as perpendicular to the nanowire [51, 12](see section **??** for more information).

We also studied the field evolution of the second and the third resonances. As presented in Fig. 5.7. These two crossings also split with increasing magnetic fields and developed ZBCPs at low field. The ZBCPs, however, disappear for fields above 0.2 T, making them unlikely due to MZM. Instead, they are most likely due to Andreev bound states [85].

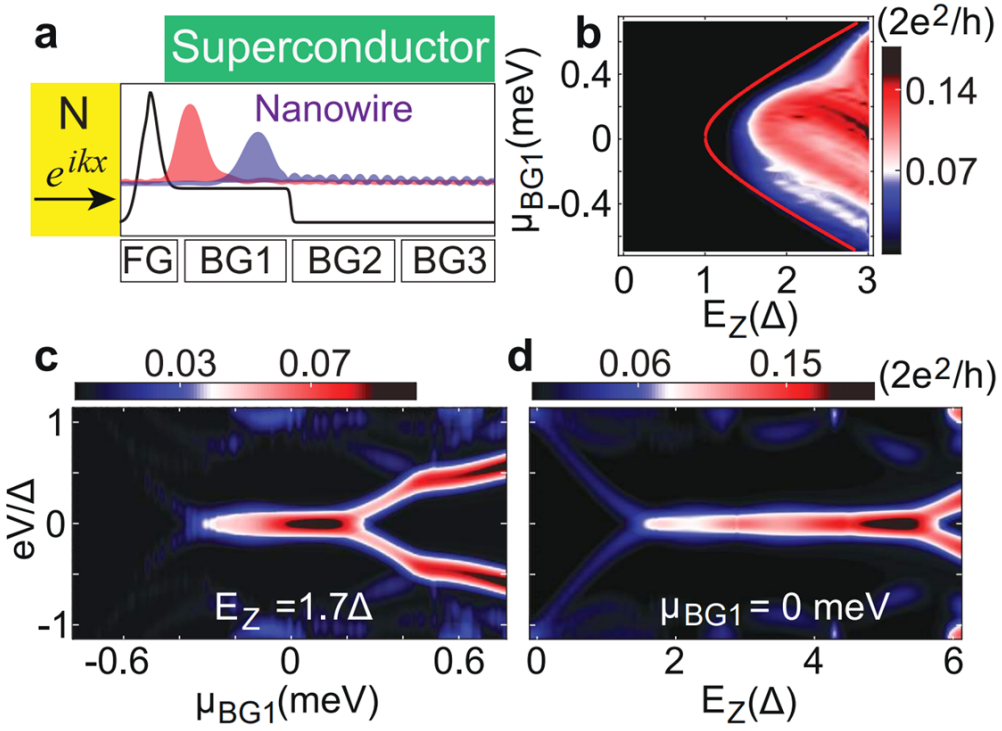

Figure 5.8: **Theoretical simulations using a tight-binding model.** **a**, model schematics. A nanowire is contacted by a superconductor and a normal metal. The potential profile in shown in black curve. A plane wave e^{ikx} coming from N can tunnel into the nanowire through the barrier above FG. The chemical potential above BG1, μ_{BG1}, is tunable, while potentials above BG2 and BG3 are fixed. The calculated wavefunction amplitudes for zero-energy states are shown in red and blue. **b**, conductance map taken at zero bias. The red curve corresponds to a plot of Eq.5.1. **c**, conductance map in bias energy vs. chemical potential at $E_Z = 1.7\ \Delta$. **d**, conductance map in bias energy vs. Zeeman energy splitting at $\mu_{BG1} = 0$ meV. In **b-d**, thermal broadening is set to 50 μeV to match the experimental ZBCP width.

Stenger and Stanescu set up a quasi one-dimensional tight-binding model to numerically study a finite length nanowire under the conditions set by Eq.5.1. To match our experimental conditions, a high potential barrier is created above FG. Potential above $BG1$, μ_{BG1}, is continuously tuned, while potential above $BG2$ and $BG3$ is kept constant (Fig. 5.8(a)). Fig. 5.8(a) also shows calculated wavefunction amplitude profiles of the two MZMs. The left MZM decays into the barrier region above FG. The right MZM has an evanescent tail that extends to non-topological regions above $BG2$ and $BG3$. These tails are responsible for a reduced overlap between left and right MZMs. Due to the small MZMs overlap, the oscillations of the MZMs don't reach large amplitudes in energy. Conductance map at zero bias in chemical potential versus Zeeman energy is calculated from the tunneling rates of quantum states (Fig. 5.8(b)). The boundary of increased zero-bias conductance is consistent with experimental data in Fig. 5.6, where the minimum onset field of the ZBCPs is also observed to be larger than $E_Z = \Delta$. The oscillations inside the high conductance region are due to MZMs oscillations.

If thermal broadening is included, conductance resonances appear as a single zero-bias peak despite MZMs oscillations. In Fig. 5.8(c), at a finite Zeeman splitting of 1.7 Δ, we observe an extended ZBCP at the center of the map. The zero-bias state occupies a similar range of chemical potential as in the experimental conductance map in Fig. 5.4(f), except that both branches of the spectrum are visible in the simulation. Conductance is suppressed at more negative values of the chemical potential because the states move farther from the probe lead N. In the conductance map at chemical potential $\mu_{\mathrm{BG1}} = 0$ meV (Fig. 5.8(d)), an extended zero-bias conductance peak is present from $E = 1.5\ \Delta$ up to $E = 5.8\ \Delta$. See methods summary and supplementary information in [86] for calculation details.

Comparison between the model(Fig. 5.8(b)-(d)) and the experiments(Figs. 5.4 - 5.5) allows us to conclude that ZBCP occurs in the parameter region that is consistent with the predicted topological superconducting phase. This observation makes it significantly less likely that these zero-bias peaks have an origin other than Majorana bound states. Beyond finite-size effects, the detailed experimental phase diagram of zero-bias peaks can be used in future experiments to study how the topological phase is affected by electron-electron interactions, disorder, vector potentials and electrostatics.

As a work finished in 2016 and published in 2017 [86], the above discussions and conclusions are based on the theoretical simulation and related theories back then. At that time, we suspected the first resonance we observed in Fig. 5.1(c) may be associated with the high density of states near the bottom of a one-dimensional subband. As the experiment results showed ZBCPs actually developed around the first resonance, that seems a plausible hypothesis. With the development of theories and experiments, however, we now think it might be meaningless to talk about subbands in a nanowire segment with the length of ∼200 nm, since subbands are so strongly mixed due to the longitudinal confinement. More likely, those resonance are trivial Andreev bound states (ABSs) induced by inhomogeneity inside the system. As shown in section 5.6, those Andreev bound states are pretty common in nanowire-superconductor hybrid devices. Moreover, partially separated ABSs, which consist of component MZMs separated by a distance of the order of the characteristic Majorana decay length, are shown to have nearly zero energy in a significant range of parameters, e.g. Zeeman energy and chemical potential [43]. As the consequence, we now think the phase represented by the ZBCPs may not be identified as the topological phase. While it is difficult to fully exclude the Majorana scenario in our case as we only measured one end of the hybrid region, it is fairly possible that our data is a manifestation of the partially separated ABSs.

5.4 ZBCPs Splitting

In a nanowire system with realistic length, overlap of Majorana wavefunctions is inevitable and could lead to the zero energy Majorana states to hybridize into charged Bogoliubov quasiparticles of finite energy[35, 93], i.e. the original ZBCPs should deviate from zero energy under the presence of MZM overlap. Observation of the simultaneously splitting of the ZBCPs from the two ends of the topological region are considered as the smoking gun evidence for the existence of the MZM [35].

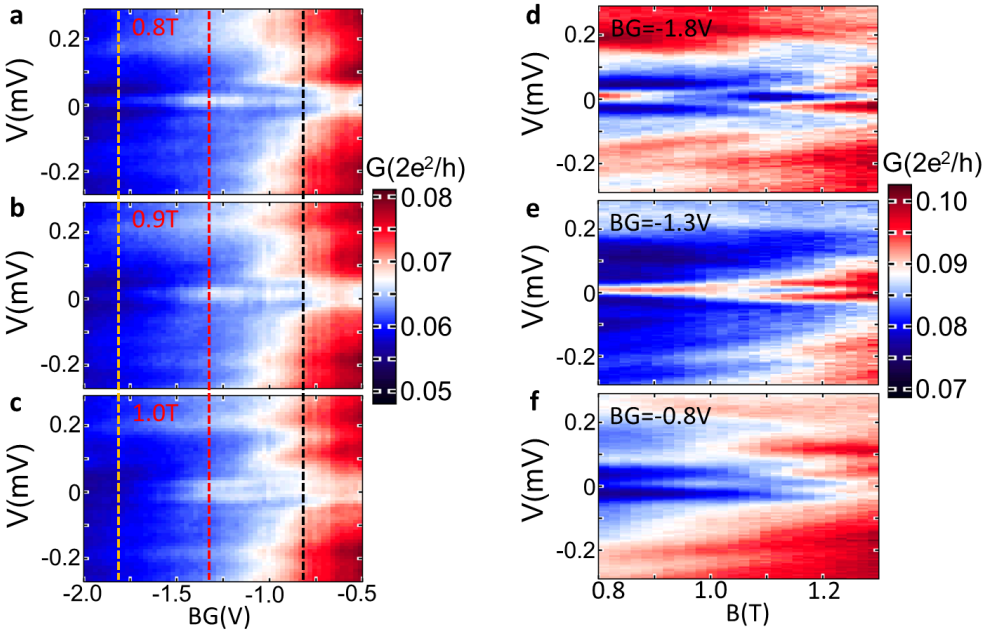

Figure 5.9: **ZBCPs splitting in device B. a-c**, Differential conductance scans as functions of bias voltage and BG voltage at different magnetic fields. The field direction is in parallel to the nanowire main axis. With increasing fields, the single ZBCP at 0.8 T splits into two peaks at 1.0 T. The dashed lines indicate the BG setting in panel **d-f**. **d-f**, Magnetic field scans at different BG voltages showing the splittings onset at different fields for different BG voltages.

Without taking into account of electronic interactions, the energy of overlapping MZMs would oscillate with chemical potential and magnetic fields with increasing amplitude [35]. Electronic interactions, particularly with bound charges in the dielectric surroundings, could suppress Majorana hybridization around parity crossings and drastically change the non-interacting paradigm [93]. Regions with pinning zero bias peaks can thus appear between the oscillation regions. It is worth noting that this effect could also lead Majoranas remain insensitive to local perturbations, despite their overlap [93].

In our experiments, we observed splitting of ZBCP as indicated in Fig. 5.4(h) in device A. In device B with similar gates and contacts configuration, we also observed ZBCP split with both magnetic fields and chemical potential(Fig. 5.9). The splitting exceeds two times the full width of half maximum of the ZBCP and robust against both BG1 and magnetic fields tuning. While the predicted oscillation behavior has not been observed in our devices, leaking of wavefunctions into the nearby nanowire regions could explain the suppressed oscillation as discussed in section5.3. We notice a steplike spin-orbit coupling could cause the oscillation to decay in magnetic fields [94], which may also explain our results.

5.5 Field Angle Dependence of ZBCPs

Majorana states are predicted to appear only when the applied field has a component perpendicular to the spin-orbit field, previously measured to be perpendicular to the nanowire [51, 95]. When the magnetic field is parallel to the spin-orbit field, no MZM should appear. We tested this requirement and the results from device A are shown in Fig. 5.10 and Fig. 5.11. In Fig. 5.10, magnetic fields were scanned in different directions regarding the spin-orbit field, where θ is the angle between the applied field and the nanowire main axis. ZBCPs are most prominent at θ=0 and θ=π and are totally absent when θ is close to π(Fig. 5.10(a)-(j)). In addition, when the field magnitude is fixed at 0.5 T, ZBCPs only appear within a small angle around θ=0 (Fig. 5.10(k)).

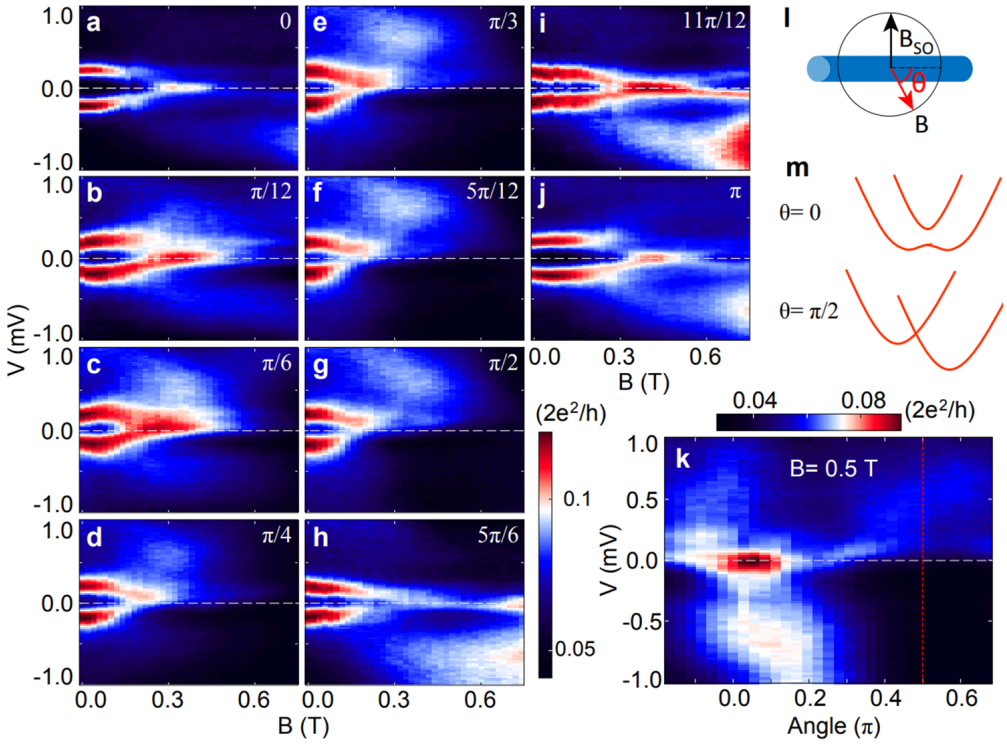

Figure 5.10: **Magnetic field orientation dependence of ZBCPs in device D. a-j**, conductance maps in bias vs. magnetic field at different angles indicated in the upper right corner of each panel, from 0 to π. **k**, conductance maps in bias vs. field angle at a fixed field B=0.5 T, the vertical dashed line marks the angle at $\pi/2$. **l**, Schematics of magnetic field direction. The angle is defined with respect to nanowire main axis. The dashed lines mark zero bias voltage line. **m**, Schematics of the band structure in magnetic field at an angle of 0 and $\pi/2$.

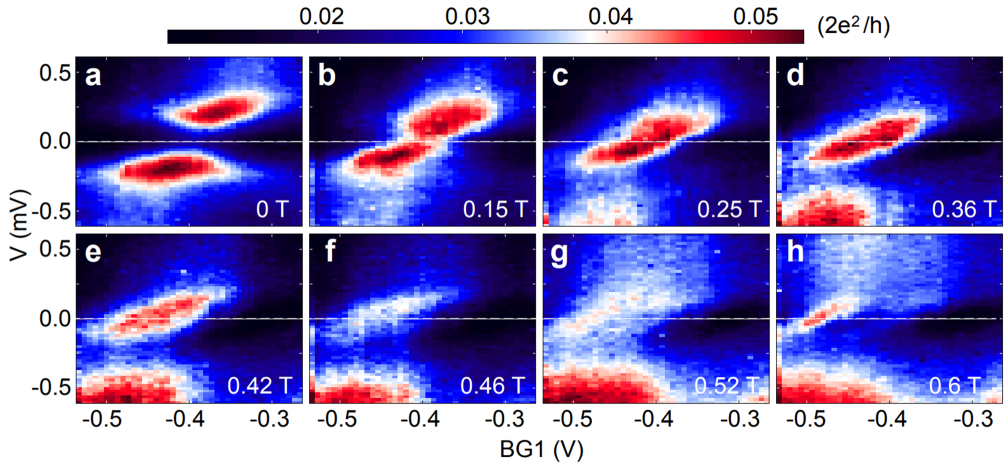

Figure 5.11: **Evolution of the first resonance in device D at an angle of $\pi/2$. a-h**, conductance maps in bias vs. BG1 at different magnetic fields indicated in the lower right corner of each panel. The dashed lines mark zero bias voltage line.

In Fig. 5.17, we show the field evolution of the first resonance in device A when the field direction is perpendicular to the nanowire. While the induced gap still closes around 0.3 T, no clear ZBCPs have been observed up to 0.6 T.

We also examine the field dependence of the ZBCP phase diagram in device C and the results are presented in Fig. 5.12. When the field angle θ=0, the regime hosting ZBCPs grows in BG voltage space with increasing fields. At θ=$\pi/18$, the regime with ZBCPs are similar to θ=0. At θ=$\pi/6$, however, ZBCPs occupy a smaller BG voltage space at each fields comparing to ZBCPs at θ=0. While the result is preliminary, it suggests the ZBCP phase does shrink with increasing θ.

5.6 Non-Majorana ZBCPs in Two-Terminal Devices

This work is published in Physical Review Letters [85] in collaboration with Chen, J., Woods, B. D., Hocevar, M., Car, D., Plissard, S. R., Bakkers, E.P.A.M., Stanescu, T. D., Frolov, S.M..

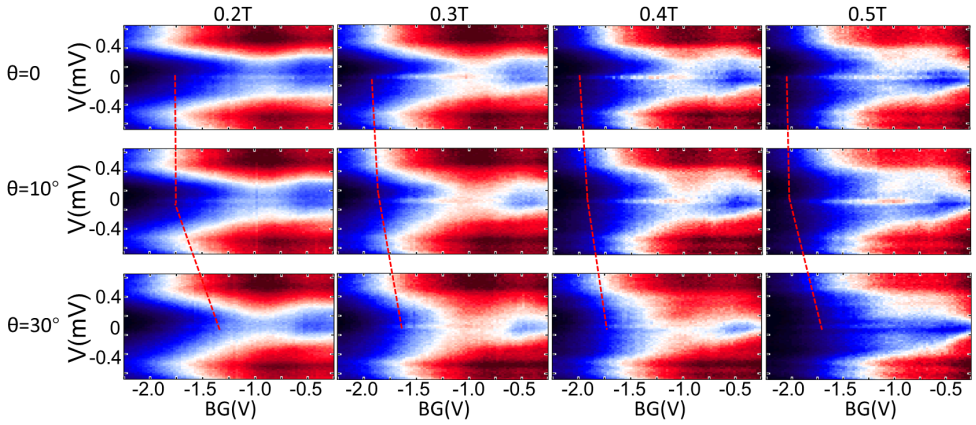

Figure 5.12: **BG dependence of ZBCPs at different fields and different field angles in device E.** At $\theta = 0$, this device shows similar results to device A, i.e. ZBCPs develop at finite field and grows in BG voltage space with increasing fields. At $\theta{=}\pi/6$, while the ZBCPs still present, they occupy a smaller BG voltage range than in $\theta = 0$.

A ZBCP in nanowire devices is known to have many other origins not related to Majorana modes. Disorder-induced ZBCPs can appear due to spectral crowding near zero bias. Fine-tuned so-called 'class D' peaks can manifest in the intermediate mesoscopic regime which does not correspond to a large disordered ensemble of states [96, 97, 98, 84, 77], this is a concept closely related to a set of a few randomly coupled quantum dots [85, 38]. Finally, trivial Andreev bound states in quantum dots were shown to exhibit ZBCP and some degree of resonance pinning to zero bias or near-zero oscillations due to gap closing and level repulsion from higher energy states [41, 80, 38, 79, 81, 82, 83]. There is no fundamental reason why any of such non-Majorana ZBCPs could not be tuned to have peak conductance close to a particular value, including the quantized value. While on the theory side it is clear quantized peak should be a prominent signature of MZMs as it comes out naturally from simple calculations [1], but on the experimental side it is not enough to just show a peak of the right value because it may be a result of fine-tuning [39, 40].

In particular, ABSs can arise due to inhomogeneity in the system and are known to share many features of MZMs [79, 82]. As we discuss in Chapter 2, for the simplest case

of a quantum dot (QD) coupled to a superconductor, the ground state is a spin singlet and the excited state is a spin doublet when the QD-superconductor coupling is strong at zero magnetic field. With finite field, the doublet state Zeeman splits while the singlet ground state does not. The transition energy corresponding to the transition between $|S\rangle$ to $|\uparrow\rangle$ decreases with increasing fields and eventually crosses zero energy and generates a ZBCP.

In the case without considering the effect of level repulsion and gap closing, the extension of the ZBCP in Zeeman energy or chemical potential should be comparable to the ZBCP width (See Fig. 5.13), which is distinct from the ZBCPs due to MZMs. With gap closing and level repulsion, however, the scenario is more complex and ZBCPs due to ABS can stick to zero bias for an extended range[80, 79, 82].

Here we present data from device D, which shows ubiquitous ZBCPs, which are likely due to trivial ABSs, appear at finite fields.

Device D (Fig. 5.14(a)) is fabricated with the same methods and configuration as device A, except that it only has one tunnel gate (FG) between the two contacts. In Figs. 5.14(b)-(d), we first show three magnetic field scans with different BG1 voltages. At zero field, this device exhibits a soft but otherwise featureless superconducting gap characterized by smooth evolution of suppressed conductance within the gap as a function of bias. In Fig. 5.14(b), the evolution within the magnetic field range 0-300 mT looks like a closing of the induced gap: the suppressed conductance window around zero bias shrinks and two branches of high conductance move from the apparent induced gap edges ($V = \pm 250\mu$V) toward lower bias reaching zero bias at around 300 mT. Beyond B = 300 mT, an apparent zero bias resonance is observed over a significant range of magnetic field, up to at least B = 1 T. This range, expressed in Zeeman energy (500 μeV), greatly exceeds the bias width of that resonance (150 μeV)—thus we identify it as 'pinned' to zero energy.

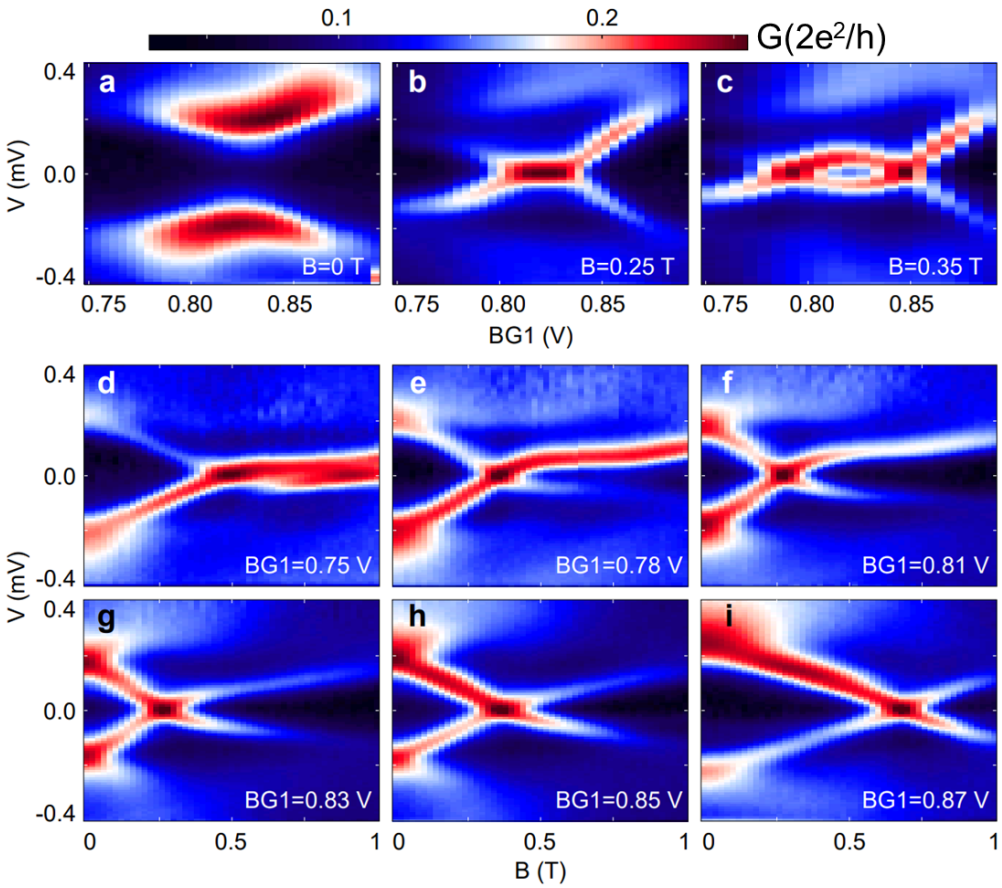

Figure 5.13: **Magnetic field evolution of apparent ABS. a-c**, The evolution of ABS with magnetic field in a device similar to device D. **a**, At zero field, a pair of conductance resonances appears symmetrically at positive and negative bias close to the superconducting gap edge. **b**, At a finite field of 0.25 T, conductance resonances split off from the gap edge and move to lower bias touching zero bias in the center of the scan. **c**, At 0.35 T top and bottom conductance resonances trade positions forming a loop in the center. This behavior is characteristic of a magnetic-field induced singlet-to-doublet ground state quantum phase transition in quantum dots coupled to superconductors. Panels **d-i** demonstrate how magnetic field dispersion of ABS is affected by BG1 set to different points throughout the range shown in panels **a-c**. In panel **d**, a near-zero resonance is observed over a significant range of magnetic field exceeding 0.5T. However, subsequent panels show that this pinning to zero bias is a result of fine-tuning and is only seen at a particular setting of BG1.

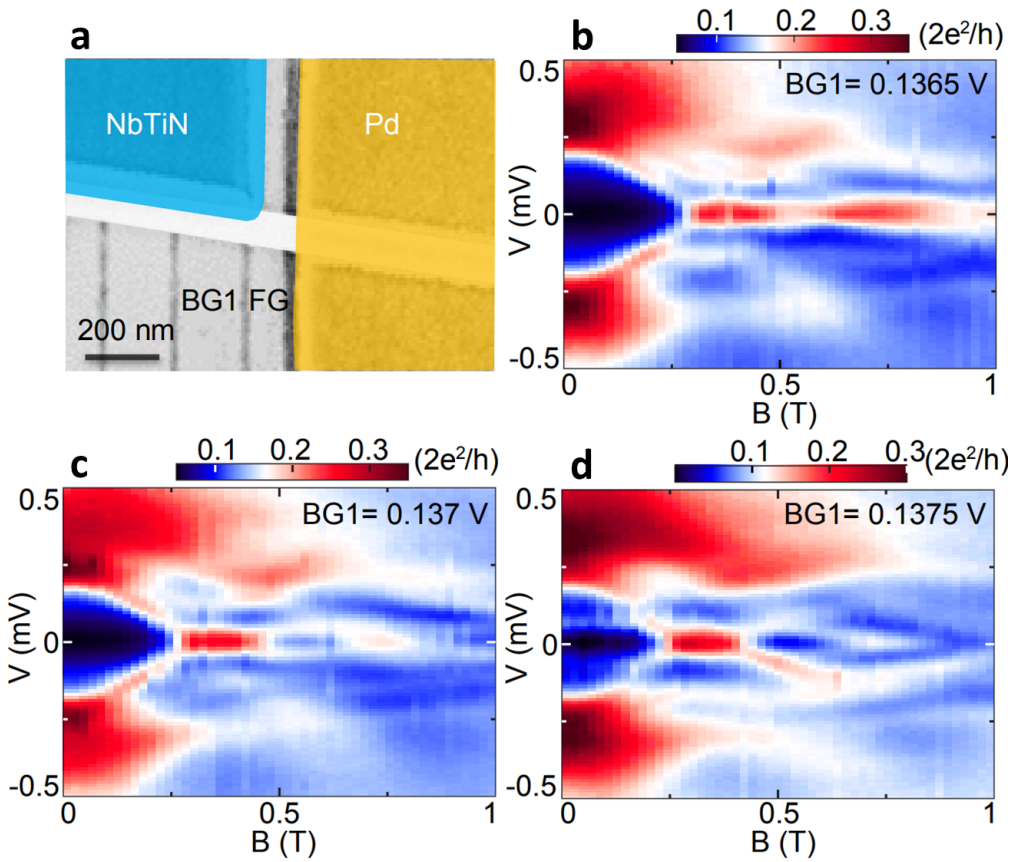

Figure 5.14: **ZBCPs at finite fields.** **a**, Scanning electron micrograph of the studied device. The bottom gates FG (100 nm wide) and BG1 (200 nm wide) are made of Ti(5 nm)/Au(10 nm). The nanowire is about 100 nm in diameter. The superconducting contact is a trilayer of Ti(5 nm)/NbTi(5 nm)/NbTiN(150 nm), while the normal contact is a Ti(15 nm)/Pd(150 nm) stack. **b-d** Differential conductance maps in bias voltage V vs. magnetic field at $BG1 = 0.1365$, 0.137 and 0.1375 V, respectively. $FG = 0.53$ V for data in Fig.5.14 and Fig.5.15.

Fig. 5.14(c) shows that with a minor variation in BG1 a single zero-bias resonance can be transformed into a pair of low-bias resonances oscillating around zero bias as magnetic field is increased to 1 T. Such oscillations are consistent with MZMs in a short nanowire [91], and in fact data in Fig. 5.14(b) can also be interpreted as similar oscillations of smaller amplitude, less than the resonance width. Fig. 5.14(d), however, conveys a different picture. After another change in BG1 that should not alter the bulk density in any significant way, we can resolve that the apparent oscillations are actually superimposed of two unrelated pairs of resonances moving to zero bias at different magnetic fields, 0.4 T and 0.7 T. This demonstrates that the visibility of different branches can be strongly affected by minor changes in gate voltages, and some of the branches may become invisible in differential conductance maps, creating the appearance of a sole zero bias resonance or a pair of oscillating resonances, both being important signatures of MZMs.

In Fig. 5.15, we show ZBCPs and low energy resonances are a ubiquitous feature in this device at finite fields. In large range BG1 vs. bias voltage scans, a large number of transient resonances can be seen crisscrossing the subgap region without sticking to zero bias at zero field (Fig. 5.15(a)). These resonances are likely due to states localized near the tunneling barrier, with their conductance partially suppressed within the soft induced gap. At finite magnetic field B = 0.3 T, the transient resonances are still visible, but another set of features tightly confined close to zero bias is now observed throughout the presented range of BG1 (Fig. 5.15(b)). The most important information here is that the finite field scan host about 30 distinct ZBCP regions. If all of these ZBCPs were due to topological superconductivity, we would expect being able to tune through tens of 1D subbands, which is inconsistent with quantum point contact measurements on similar nanowires [99]. Furthermore, the energy spacings between the nearby resonances are about 0.2 – 0.5 meV, which are much smaller than the energy spacings between one-dimensional subbands.

We zoom in on a representative BG1 range in Figs 5.15(c)-(e). At zero field the inside of the induced gap for $|V| < 250\mu V$ is featureless on this scale (Fig. 5.15(c)). In the same gate range at finite field $B = 0.3$ T (Fig. 5.15(d)), three oscillations around zero bias and higher bias subgap states are observed. At a higher field $B = 0.5$ T (Fig. 5.15(e)), an extended ZBCP is observed. Over a range of BG between 1.61 V and 1.62 V the ZBCP vanishes,

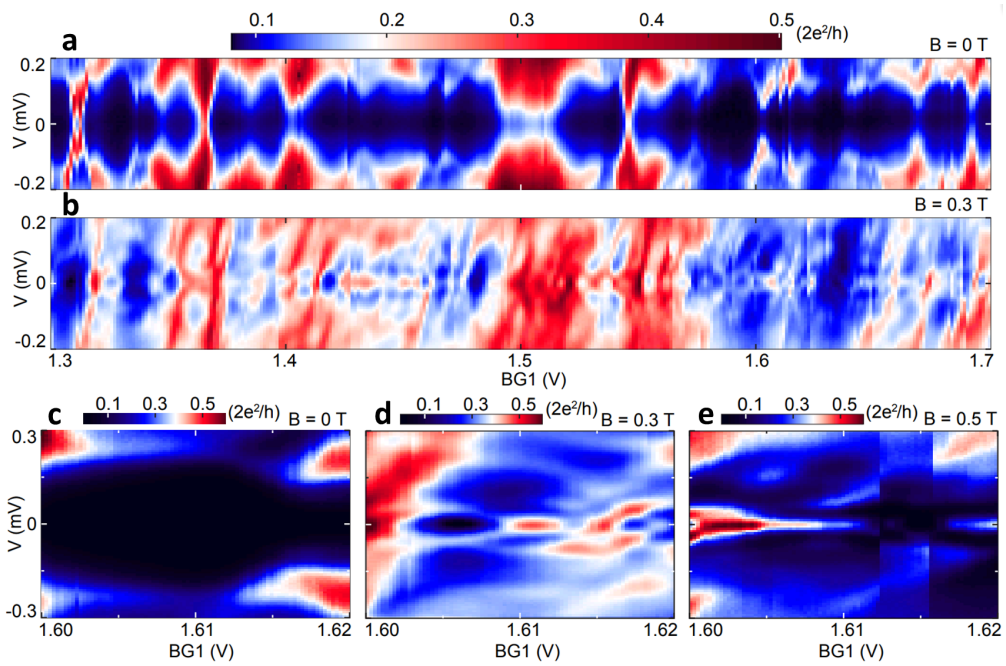

Figure 5.15: **Ubiquitous ZBP in extended range of gate** $BG1$**. a-b** Differentiate conductance maps in bias voltage V versus $BG1$ at $B = 0$ and 0.3 T, respectively. **c-e** Differentiate conductance maps in bias voltage V versus $BG1$ in a small range at $B = 0$, 0.3 and 0.5 T, respectively.

however this is an artifact due to charge jumps, i.e. charge rearrangements near the gate leading to a momentary shift in the electrostatic potential. Such charge jumps are common in nanowire devices.

We notice the regime shown in Fig. 5.15 is similar to the regime with positive BG1 voltage in device A (Fig. 5.1(c)). With highly packed resonances in those regimes, it is difficult to trace the field evolution of single resonance, and the ZBCPs at finite fields are more likely due to the coalescence of several adjacent resonances, e.g. as shown in Fig. 5.15(d)(e). We also claim device D does not provide a regime that resembles the negative BG1 regime in device A, which hosts resonances with large energy spacing.

Another important observation in Fig. 5.15 is that the low energy states often merge continuously into the transient resonances above the induced gap. This behavior is ex-

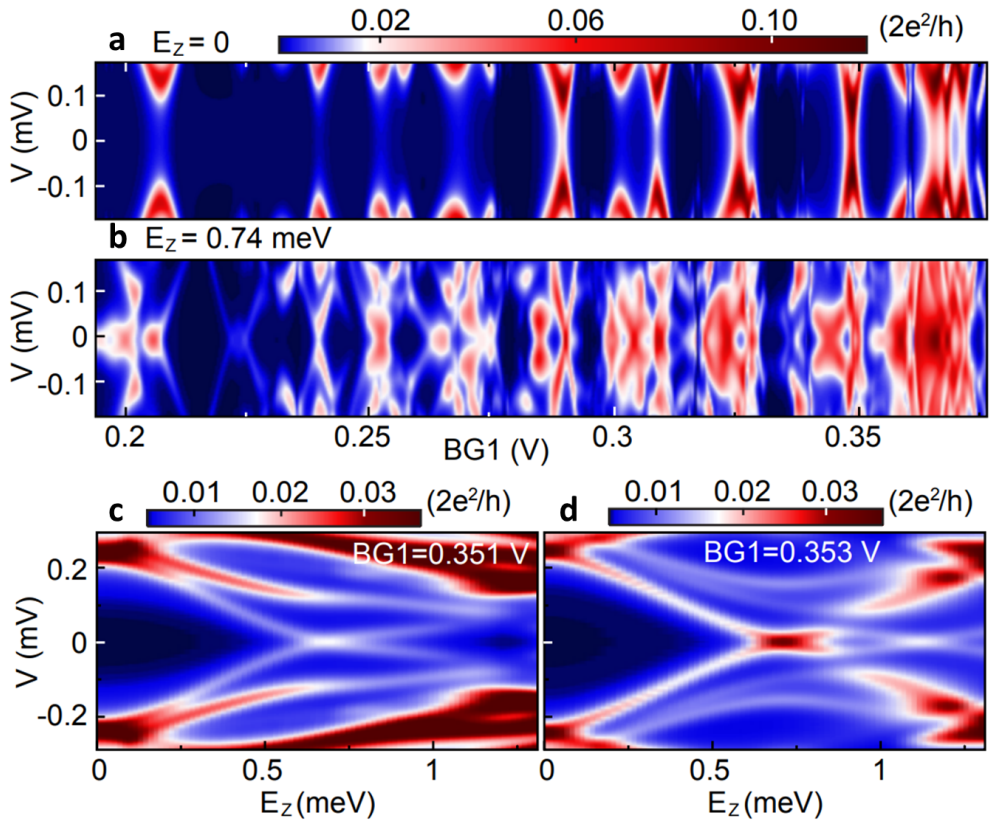

Figure 5.16: **Calculated differential conductance as a function of** BG1 **and bias-voltage** V**.** For panel **a**, $E_Z = 0$. For panel **b**, $E_Z = 0.74$ meV. The FG voltage is 0.38 V and the temperature $k_BT = 0.15$ meV. **c-d** Calculated differential conductance as a function of Zeeman energy and bias voltage V for BG1 = 0.351 and 0.353 V, respectively.

pected and observed in quantum dots strongly coupled to superconductors, where transport resonances due to ABS split from and merge into the induced gap as the dot occupation changes from even to odd [100, 41]. In general, ABS can emerge in nanowire system with inhomogeneity. And inhomogeneity can be induced by many effects, e.g. the configuration of multiple electrostatic gates, the shape of the half-covering superconducting contact, and by disorder at semiconductor-superconductor interfaces. Those effects are all common for hybrid nanowire devices. As a result, ABS induced ZBCPs and low energy states might be a ubiquitous feature in our nanowire devices at finite fields.

To study the possible mechanisms that cause the pinning of ABS near zero energy. Woods and Stanescu perform 3D Schrödinger-Poisson calculations that incorporate geometric and electrostatic details of our devices. In that work [38], it shows that the inhomogeneity can purely arise due to the device geometry, without taking account the disorder. The simulation well captures the packed crisscrossing resonances at zero field and ubiquitous ZBCPs at finite fields as shown in Fig. 5.16(a)(b). Simulations of differential conductance maps as a function of Zeeman energy and bias voltage (Fig. 5.16(c)(d)) also reproduce the pinning ZBCP and spitting feature as shown in Fig. 5.14(c)(d). Calculated wavefunction profiles for those states indicate all the corresponding wavefunctions are localized in the nanowire segment near the tunnel barrier (see [85] for more details).

In opposite to the simulation for the phase diagram in device A (Fig. 5.8), where wavefunctions have small weight in the tunnel barrier region, all the wavefunctions here have significant weight in FG, i.e. the tunnel region and thus are unlikely have a topological origin.

In conclusion, we have demonstrated that many of the commonly discussed features of MZMs and topological phase, such as gap closing, zero-bias pinning in magnetic field or gate are ubiquitous and easily observed when ensembles of trivial ABS are present. Improvements to reduce inhomogeneity, e.g. optimization of device geometry and semiconductor-superconductor interfaces, are thus necessary to provide a unambiguous prove of MZM.

5.7 Results in Further Optimized Devices

Motivated by the results of previous sections, we further optimized our device in following aspects: I) using only one tunnel gate (FG) and BG to have more uniform electric fields. II) fully covering the nanowire with the superconductor. iii) using a higher concentrated (1:200) ammonium sulfide water solution in sulfur passivation to achieve better superconductor and semiconductor interface (see section 4 for more details). With those improvements, we search Majorana signature again in device E.

As shown in the SEM image (Fig. 5.17(a)), device E has a 300 nm width BG underneath

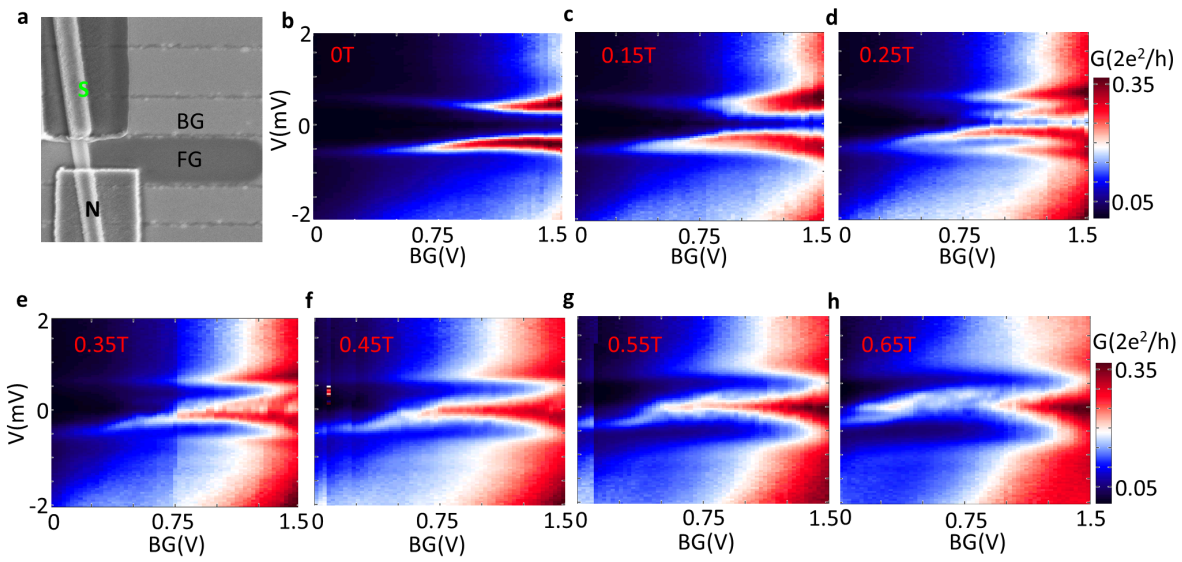

Figure 5.17: **BG dependence of ZBCPs in different magnetic fields in device E. a**, SEM image of device E. **b-h**, BG vs. bias voltage scans at different fields. A ZBCP forms with increasing fields and possibly split at high fields. The ZBCP grows in BG voltage space with increasing fields after it first appear around 0.35 T.

the superconducting contact and an FG to create the tunnel barrier. BG vs. bias voltage scan at zero field(Fig. 5.17(b)) shows the induced gap is much harder especially at lower BG voltage regime(see Fig.4.11 for more scans from the same device) comparing to the previous device A. The gap shows sharp gap edges and highly suppressed conductance(0.05 $2e^2/h$) inside the gap. We claim the BG regime is cleaner than previous devices as there are no crisscrossing resonance, but also with probably weaker coupling between the BG and the nanowire, as there is only one resonance around BG = 1.25 V manifested by the wiggling of the gap edges within similar gate voltage range comparing to device A.

With increasing field along the nanowire main axis (Fig. 5.17(c)-(h)), two states detach from the gap edges around BG = 1 V and move toward zero bias. Around 0.35T, the two states touch each other around and form into a ZBCP. The ZBCP becomes more prominent and grows to cover more BG voltage space at 0.45 T and 0.55 T. At 0.65 T, the peak near

the scan center deviates from zero bias and fade away while the peaks at the edges of the BG regime remain strong at zero bias. Those BG scans show how the ZBCP evolve and possibly split in high fields similar to what we observed in device A.

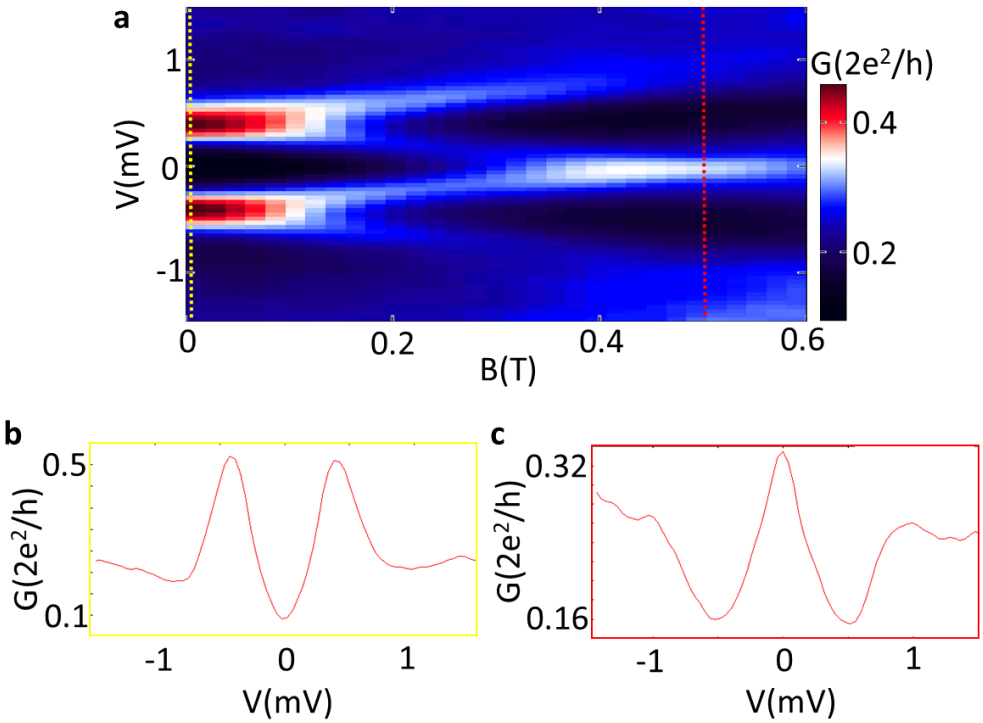

Figure 5.18: **Magnetic field dependence of the ZBCP in device E. a**, Differential conductance as a function of magnetic field and bias voltage, while BG is set to 1 V. The ZBCP first emerge around 0.35 T and persist to at least 0.6 T. **b**, bias linecut taken at B = 0 from panel **a**. **c**, bias linecut taken at B = 0. 5 T shows the shape of the ZBCP

The evolution of the ZBCP can also be seen in bias voltage vs. magnetic field scans (Fig. 5.18). With an increasing field, two states detached the apparent gap edges and move toward zero bias. The ZBCP forms around 0.3 T and persists to over 0.6 T. The peak height reaches over 0.3 $2e^2/h$, which is higher than those in device A. It is worth noting that an energy gap remains open up to at least B = 0.6 T.

While device E exhibits harder induced gap and cleaner BG regime with much less resonances, it generally does not provide more information than device A.

5.8 Conclusions

To summarize, we have observed ZBCPs in hybrid InSb nanowire devices. The general features about those ZBCPs are: (I) they emerge at finite magnetic field and stick around zero bias for a range of 0.3 T to 0.7 T. (II) ZBCPs are tunable with the gate BG that is close to the tunnel barrier but are robust against tuning of other gates. (III) ZBCPs only appear when the applied magnetic field direction is within a certain angle around the nanowire main axis and are absent when the field direction is perpendicular to the nanowire main axis. Apart from those, we also manifest ZBCPs can be predictably generated by tuning BG voltages and magnetic fields. An experimental phase diagram of ZBCPs has been mapped out, which is in good agreement with a theoretical simulation of two overlapped MZMs.

While those observations are consistent with Majorana theories, we also find ZBCPs can emerge due to trivial ABS in similar devices as a result of inhomogeneity. Lack of more Majorana evidence, e.g. quantized ZBCPs or ZBCPs oscillation, prevents us to further study of MZMs. Since Majorana nonlocality could also be used to distinguish MZMs from trivial states, we next turn to the study of three-terminal devices and the result is shown in the next chapter.

6.0 Tunneling Spectroscopy in Three-Terminal Devices

6.1 Introduction

Majorana bound states (MBSs) are predicted to appear in pairs in one-dimensional systems with one on each boundary of a topological regime after a topological phase transition. As shown in chapter 5, we did find possible signatures of MBS- namely zero bias conductance peaks (ZBCPs) that appear at finite magnetic fields in two-terminal devices.

Those ZBCPs show field dependence and gate dependence that are consistent with Majorana theories. However, as also presented in chapter 5, Andreev bound states (ABSs) and 'class D' peaks can mimic the behavior of Majorana ZBCPs. It is shown that those states, as a generic low-energy feature of spin-orbit coupled semiconductor-superconductor heterostructures, can even produce quantized ZBCPs in local tunneling experiments over an extended range of parameters [40, 39], making it hard to unambiguously identify MBS in two-terminal local measurements. On the contrary, nonlocal measurement, e.g. three-terminal measurement, could provide a better platform to study MBSs [43, 36]. With one more normal contact added to the other end of the nanowire-superconductor hybrid region, we gain the ability to monitor the two ends of the nanowire simultaneously and thus are capable of examining the existence of Majorana pairs. An observation of correlated ZBCPs at the two ends may serve as the smoking gun evidence of a pair MBSs [91]. Moreover, topological protection of Majorana based quantum computing requires spatially well-separated MBSs. It is thus of great importance to esteimate the nonlocality, i.e. the degree of separation, of the MBSs pair.

With those motivations, we fabricate and study three-terminal hybrid devices using InSb nanowires. Near zero magnetic field and thus in the topologically trivial regime, we successfully identify delocalized states that appear on both ends of the system and show correlated gate dependence. While those states demonstrate our system has the potential to host nonlocal states, localized states that only appear on one side of the region also emerge within the same S-gate regime. Moreover, correlation of the delocalized states is weakened and

obscured at finite fields, while no clear correlated ZBCPs has been observed at a field large enough for the topological phase.

Those non ideal observations suggest further improvement is necessary to confirm the existence of Majorana pairs. On the other hand, three-terminal measurement show its capability in identifying localized states. While one side of a device shows ZBCPs that are close to quantized value with field and gate dependence consistent with Majorana theories, we are able to claim a likely non-Majorana origin due to the lack of counterpart on the other side. Based on those results, we suggest all the possible Majorana signatures should be examined in three-terminal measurements to rule out of the possibility of them originating from localized wavefunctions. Even when a clear identification of correlated states may be difficult because of other states that obscure obvious conductance correlations, it is still possible to spot localized states based on their gate dependence.

The content of this chapter is presented as follows: in section 6.2, fabrication and measurement methods are discussed. In section 6.3, device information and characterization at zero magnetic field are presented. Section 6.4 shows data concerning the delocalized and localized states at zero magnetic field. In sections 6.5 and 6.6, finite field data and a quantized ZBCP originating from localized wavefunctions are discussed.

6.2 Device Fabrication and Measurement

Three-terminal devices are fabricated based on recipe 2 that we describe in chapter 4 and appendix A. The general procedures are:

1. Fabricating markers and bottom gates.
2. Making leads from the bonding pads to the local gate area.
3. Transferring nanowire from growth chip to pre-fabricated bottom gate chip.
4. Use EBL to define normal contact pattern on PMMA and deposite 10 nm Ti and 120 nm Pd after sulfur passivation and gentle sputter cleaning.
5. After lift-off of the normal metal film, define superconducting contacts by EBL and sputter 5 nm NbTi and 60 nm NbTiN using the angle deposition technique after sulfur

passivation and gentle sputter cleaning.

After fabrication processes, devices are wire bonded and measured in a dilution fridge. To measure the two sides simultaneously, we apply a bias voltage through the superconductor and connect each normal contact with a digital multimeter and AC lock-in. The signal is enhanced by the amplifiers in the IVVI racks. A schematics and a measurement circuit diagram of a typical there-terminal device can be found in Fig. 6.13. Current and differential conductance can thus be measured on the two sides. As described in Chapter 3, we correct the measured differential conductance from the lock-in removing the contribution from the measurement circuit.

Another measuring method is alternatively biasing one normal contact and measuring current from the grounded superconducting contact, while keeping the other normal contact floating. We verified these two methods yield similar results (see supplementary for more information). Since the first method measures the two ends at exact the same setting and also saves half of the time comparing to the second one, all the data shown in this chapter has been taken using the first method unless indicated. More information about the measurement setups can be found in section 3.

6.3 Device Information and Zero Field Characterization

Fig. 6.1(a) shows a scanning electron microscope (SEM) image of the device A, which we studied here in detail. The InSb nanowire is covered by a NbTiN superconducting contact (S-lead) in the middle and two normal Pd contacts N_L and N_R at the ends. It has a 400 nm wide electrostatic gate (S-Gate) underneath the superconducting contact. The two tunnel gates that are far away from the S-lead are shorted externally and controlled together as T_3, while T_L and T_R are used to create tunneling barriers for the tunneling spectroscopy. A bias voltage is applied through the middle superconducting contact and differential conductances G_L and G_R are measured from the two normal contacts simultaneously.

The starting point of measuring a three-terminal device is similar to measuring a two-terminal device. We first check the tunneling gate dependence and the induced gaps at zero

magnetic field for both sides to determine the general quality of the device.

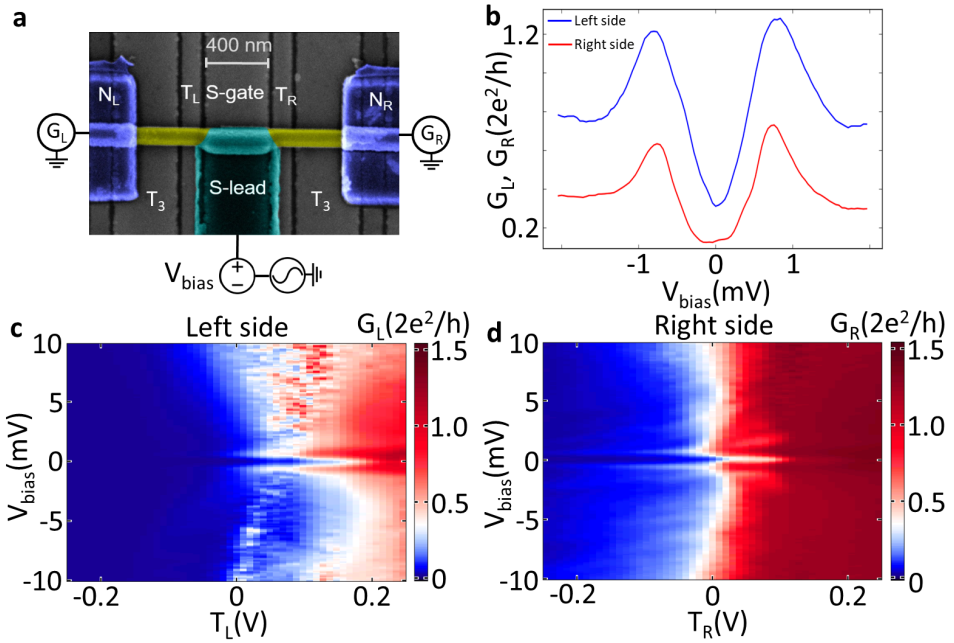

Figure 6.1: **Three-terminal nanowire device and basic characterizations.** **a**, False-color scanning electron micrograph of the measured device and the circuit diagram. **b**, Induced gap from both sides in the pinch-off regime where T_L = -0.015 V, T_R = -0.075 V and S-gate = -0.75 V. **c** and **d,** Differential conductance G_L and G_R as functions of tunnel-gate voltages and source-drain voltage. All the other gates are set to positive voltages (open regime), and magnetic field is set to B = 0.

As shown in Fig. 6.1(c)(d), bias voltage vs. tunnel gate voltage scans from the two sides in device A reveal G_L and G_R have similar monotonic tunnel gate dependence and similar saturation conductance. Near the pinch-off regimes, both sides exhibit soft but smooth induced gaps with magnitudes of 760-800 μeV(Fig.6.1(b)). More information of the induced gaps can be found in Fig. 6.14. In the following measurements, the two tunnel barriers are set to have similar overall conductance and to avoid the unstable regime.

6.4 Delocalized States at Zero Magnetic Field

Fig. 6.2 presents our main findings about the delocalized states at zero field in device A. By setting the two tunnel gates near the pinch-of regime(T_L = -0.17 V T_R = 0.09 V and scanning S-gate voltage from 0 to 0.5 V (Fig. 6.2(a)(b)), we observe resonances that appear at the same S-gate voltages on the two sides when S-gate>0.3 V. We identify four such states and label them as S1-S4. Zero bias linecuts (Fig. 6.2(c)) from panel(a)(b) capture those states more clearly. Note those resonances appear both inside and outside the induced gaps, indicating they are not created by Andreev reflections. We suppose they may be a manifestation of higher momentum wavefunctions that live away from the semiconductor-superconductor interface and closer to the bottom of the nanowire [85, 38].

Similar resonances were also observed in previous two-terminal devices with similar configuration (see chapter 5). The observation that those resonances can be probed on both sides at the same S-gate voltages implies they may be from the same states. And for those states to be observed by the tunneling measurement, which detects the local density of states near the tunnel barrier, their corresponding wavefunctions should span the whole nanowire segment that is underneath the superconducting contact, i.e. the entire hybrid region. We refer to those states as delocalized states. Apart from the delocalized states, localized states that are unique for each side also appear. For example, the right side has a strong resonance around S-gate= 0.11 V, which we label as R1. Such resonance is missing on the left side. Instead, several weaker resonances only appear on the left side around S-gate = 0.2 V and we label the most obvious one as L1.

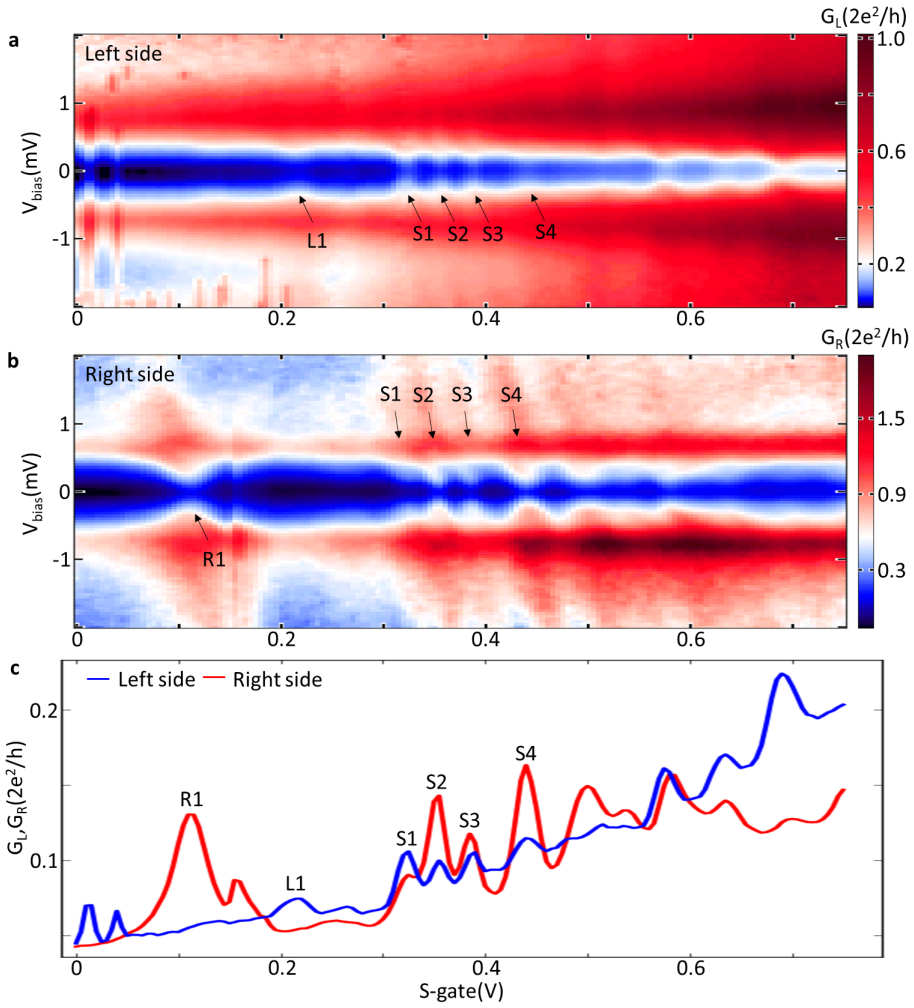

Figure 6.2: **Delocalized states in device A. a and b**, Differential conductances G_L and G_R as functions of S-gate voltage and bias voltage. T_L and T_R are fixed to -0.17 V and 0.09V respectively. Between S-gate = 0.3 V to 0.5V, four delocalized states are labeled as S1-S4 on both sides. Localized states L1 and R1 only appear on the corresponding side. **c**, Zero bias linecuts taken from panel **a** and **b**. Delocalized states from the two sides appear at the same S-gate voltages with different magnitudes of conductance.

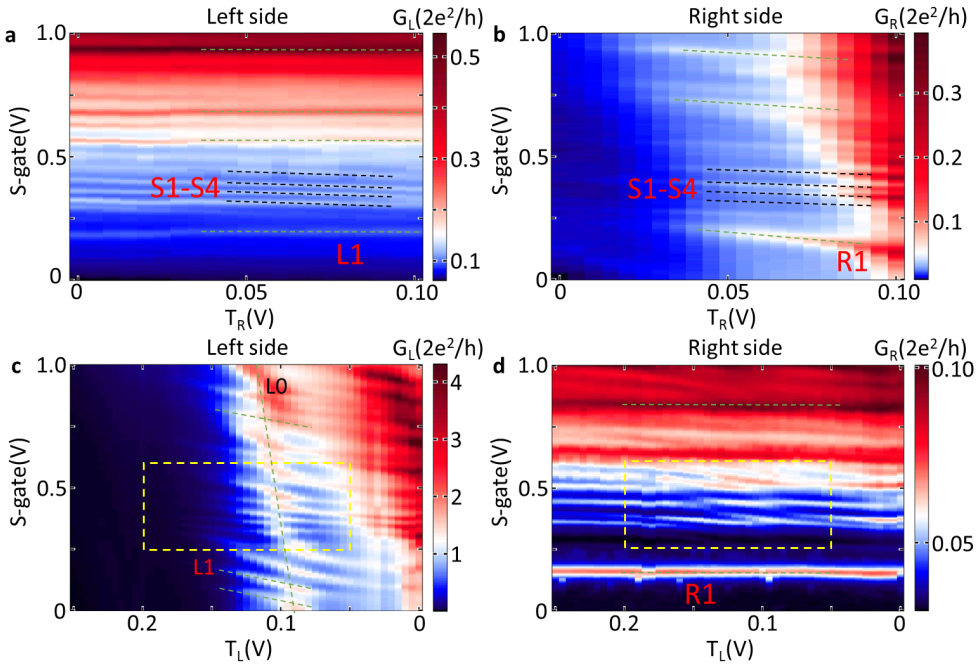

Figure 6.3: **Delocalized states in device A extended. a and b**, Zero bias differential conductances G_L and G_R as functions of S-gate voltage and T_R voltage at zero magnetic field while T_L is fixed to -0.17V. Delocalized states are indicated by black dashed lines. Those states appear on both sides at the same positions in gate voltage space. Notably, delocalized states observed on the left side show nonlocal T_R dependence. Localized states are indicated by green dashed lines and only appear on the corresponding side. **c and d**, Zero bias differential conductance G_L and G_R as functions of S-gate voltage and T_L voltage at zero magnetic field while T_R is fixed to 0.075V. Similar to panel **a** and **b**, localized states are indicated by green dashed lines. Delocalized states S1-S4 emerge in the yellow dashed square, which show complicated honeycomb patterns.

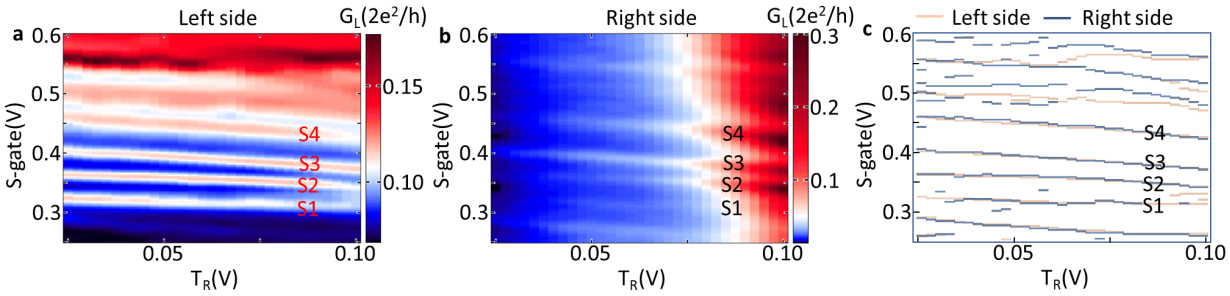

Figure 6.4: **Zoom in scans of delocalized states. a and b**, Zero bias differential conductances G_L and G_R as functions of S-gate voltage and T_R voltage at zero magnetic field while T_L is fixed to -0.17V. **c**, Plot of conductance peaks found in panel **a** and **b**. While delocalized states S1-S4 emerge below S-gate = 0.5 V, localized states appear on the left side for more positive S-gate voltages.

To further investigate those states and their spatial configuration, we perform tunnel gate vs. S-gate scans. Those conductance maps are obtained at zero magnetic field and with zero bias voltage. As shown in Fig. 6.3(a)(b), S-gate voltage vs. T_R voltage scans first reveal all the resonances have a strong S-gate dependence, indicating all the corresponding wavefunctions are coupled to the S-gate and thus are living in the nanowire segment above or near the S-gate. Second, localized states and delocalized states generally emerge as two groups of resonances with different tunnel gate dependence. Previously identified delocalized resonances S1-S4 (black dashed lines) appear on both sides and show correlated dependence on both gates. This is consistent with the assumption that we are probing the same states from the two sides. For the localized states (green dashed lines), since we are varying the T_R voltage, states localized near the right tunneling barrier, e.g. R1, show reasonable T_R dependence. On the contrary, left localized states, e.g. L1, appear as horizontal lines, which means those do not depend on T_R. Localized states also only appear on the corresponding side, e.g. R1 only appears on the right side as we also previously found in Fig. 6.2. It is notable that right localized states couple more strongly to T_R than the delocalized states, which indicates their corresponding wavefunctions may localize closer to T_R. It is also worth noting that localized states not only appear at lower S-gate voltages but also at higher S-

gate voltages than S1-S4, i.e. there is no chemical potential range in which we only have delocalized states.

In fact, there is no S-gate regime with only delocalized states and free of localized states. While resonances may accidentally appear at the same S-gate voltages on the two sides, correlated gate dependence especially the non-local dependence, i.e. S1-S4 observed on the left side show T_R dependence, confirm S1-S4 are truly from delocalized wavefunctions spanning the whole hybrid region. wThe fact that localized states are independent of the farther tunnel gate (e.g. L1 is independent from T_R), rules out the possibility that the nonlocal dependence of the delocalized states on the tunneling gate is due to electrostatic coupling between gates. Otherwise L1 should also be tunable with T_R through electrostatic gate coupling. Zoomed in S-gate vs. T_R scans on the delocalized states are shown in Fig. 6.4(a)(b). Between S-gate = 0.3 V to 0.5 V, S1-S4 emerge at exact same positions in the gate space. Above S-gate = 0.5 V, the left side scan shows localized states, which is distinct from those on the right side. The positions of each resonances can be seen clearly in Fig. 6.4(c), which plots conductance peaks from the two sides together. In Fig. 6.3(c)(d), we present the S-gate vs T_L scans in the same manner, i.e. at zero magnetic field with zero bias voltage. While an almost vertical and broad localized resonance L0 goes through the entire left side scan and interrupts other resonances, the general observation here is similar to Fig. 6.3(a)(b) and confirms the finding that localized and delocalized states coexist with different tunnel gate dependence. We claim both delocalized states and localized states in this regime show no considerable gate dependence on T_3 (See Fig.6.28 for more information).

We also perform T_L vs. T_R scans at fixed S-gate voltage to check the nonlocal dependence of delocalized states and the results can be found in Fig. 6.15.

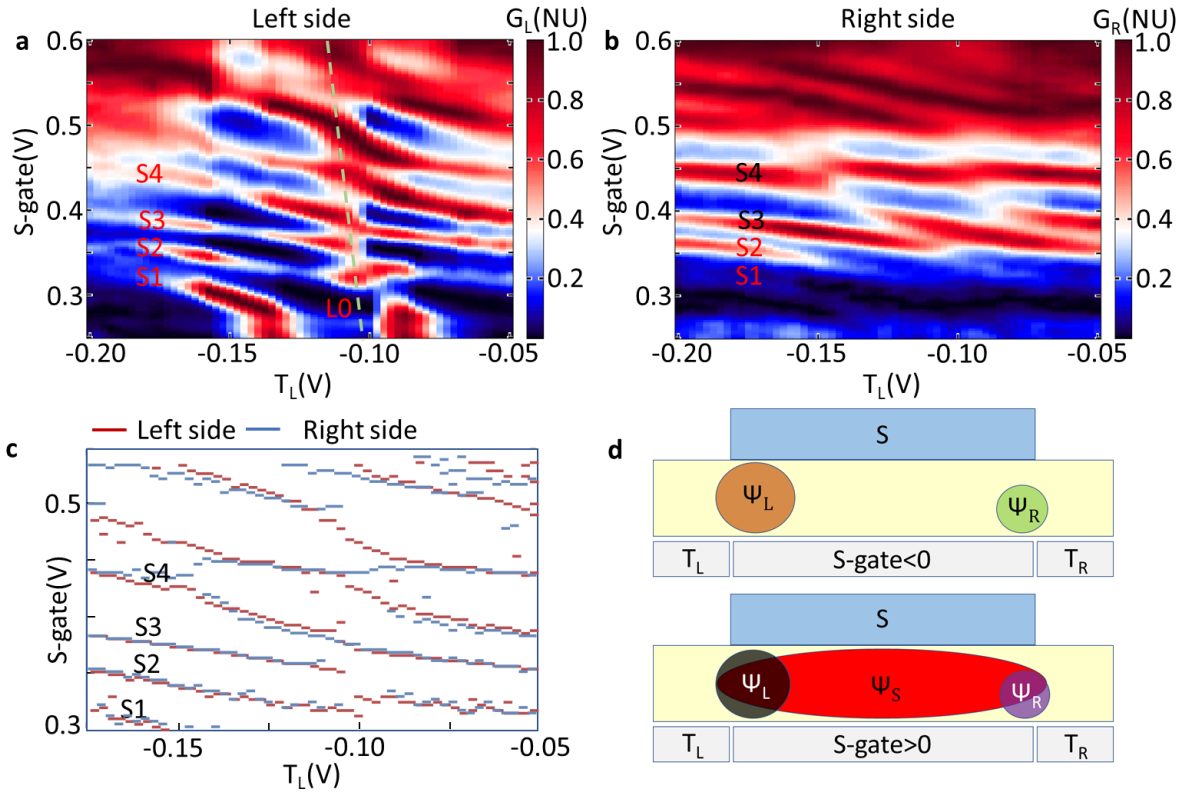

Figure 6.5: **Zoom in scans of the delocalized states.** **a,**, Zero bias differential conductances G_L and G_R as functions of S-gate voltage and T_L voltage at zero magnetic field while T_R is set to 0.075 V. Conductance is normalized to show resonances clearly. Notably, localized state L0 moves through the whole left side scans and creates discrepancy. **c**, Plot of peaks found in panel **a** and **b**. **d**, Sketches of the wavefunction configuration in the device for negative and positive S-gate voltages.

In Fig. 6.3(c)(d), the regime with delocalized states (indicated by yellow squares) shows more complicated features. Zoom-in scans of that regime (Fig. 6.5) exhibit honeycomb patterns that are common in the stability diagram of two coupled quantum dots. That observation suggests different delocalized states may couple differently to T_L. In Fig. 6.5(c), peaks found in panel (a)(b) are plotted together. While delocalized states from the two sides overlap, discrepancy does exist. We attribute the discrepancy to the presence of localized states. For example, left localized state L0 moves through the middle of the left side scan and coexists with the delocalized states.

Based on the information from the previous scans, We use Fig. 6.5(d) to propose a possible dot configuration in that device. With the influence of a nonuniform potential inside the nanowire, wavefunctions with small Fermi wave vector k_F localized near the tunnel barriers and emerge as left or right localized wavefunctions(Ψ_L or Ψ_R) in tunneling measurements. Wavefunctions(Ψ_S) corresponding to large K_F values penetrate through disorder and span the whole hybrid region. With non-zero probability amplitude on both left and right nanowire segments, those high K_F wavefunctions are detectable at both sides and appear as delocalized states. It is worth noting that delocalized wavefunctions only appear for positive S-gate voltage. No more delocalized states emerge with negative voltage on S-gate, indicating a possible increase of inhomogeneity in the system with lower chemical potential.

An important question here is whether the disorder can be mitigated by applying more positive S-gate voltage in this device. As shown in Fig. 6.16, this device shows localized states in more positive S-gate regime, indicating the persistence of inhomogeneity.

As shown in Fig. 6.17, we also find similar delocalized states and localized states in device B, which has similar bottom gate configuration, i.e. a S-gate underneath the superconducting contact and two tunnel gates T_R and T_R to create tunnel barriers. In S-gate vs. T_R scans, the top side and the bottom side present three delocalized states between S-gate = 1.5 V to 3 V. We take linecuts at $T_R = 0.25$ V and marked those states by black arrows (Fig. 6.5(b)). Bias voltage vs. S-gate scans (Fig. 6.18) confirm that delocalized states only emerge above S-gate = 1.5 V.

6.5 Field Dependence of Delocalized States and Localized States

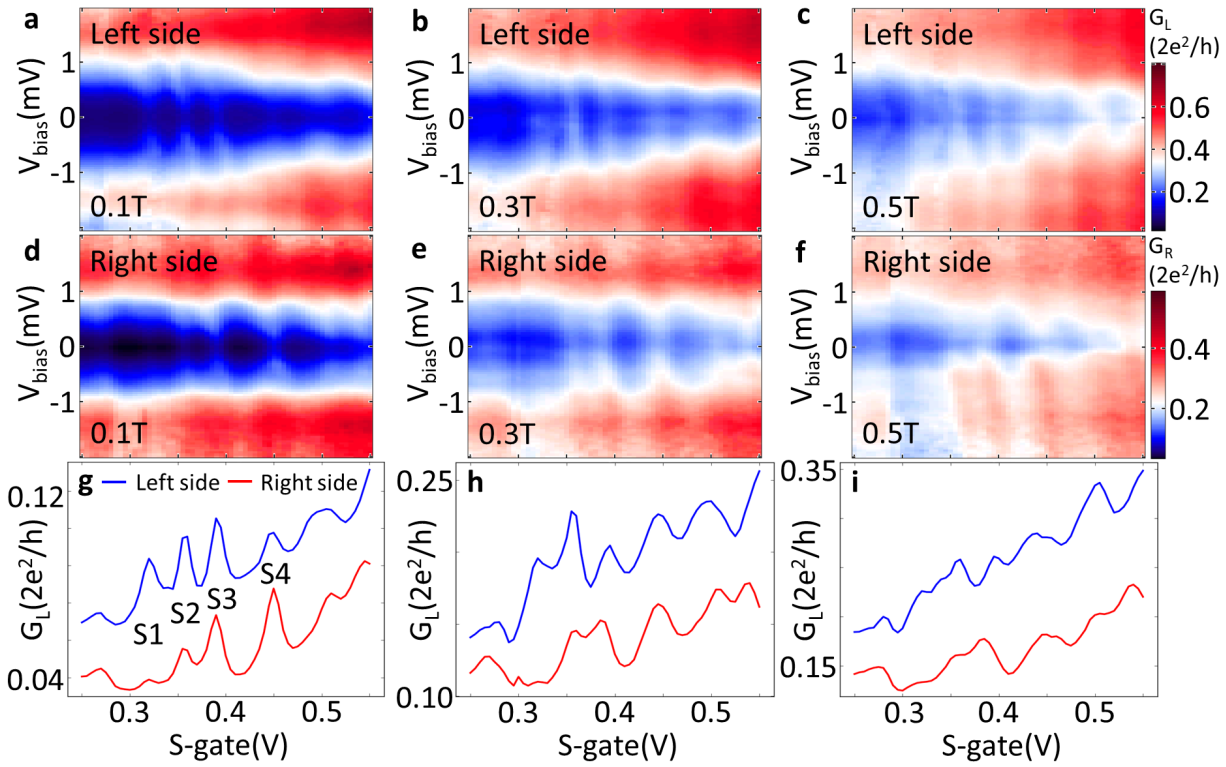

Figure 6.6: **S-gate dependence of the delocalized states at magnetic finite fields. a-f,**, Differential conductances G_L and G_R as functions of S-gate voltage and bias voltage at finite magnetic fields. With increasing fields, delocalized states S2 and S3 evolve differently on the two sides and appear at different S-gate voltages(panel **c and f**). **g-i**, Zero bias linecuts show the positions of delocalized states at finite fields.

In the previous section, we show our devices have the potential to host delocalized wavefunctions even in the presence of inhomogeneity. Since MBSs can still form at finite fields if inhomogeneity is smaller than a certain critical value [91], we next turn on the field and investigate the field dependence of the delocalized states. We study the regime with delocalized states first since they indicate low inhomogeneity compared to the regime without delocalized states and Majorana bound states favor low inhomogeneity.

Focused on the positive S-gate regime hosting delocalized states S1-S4, we scan S-gate

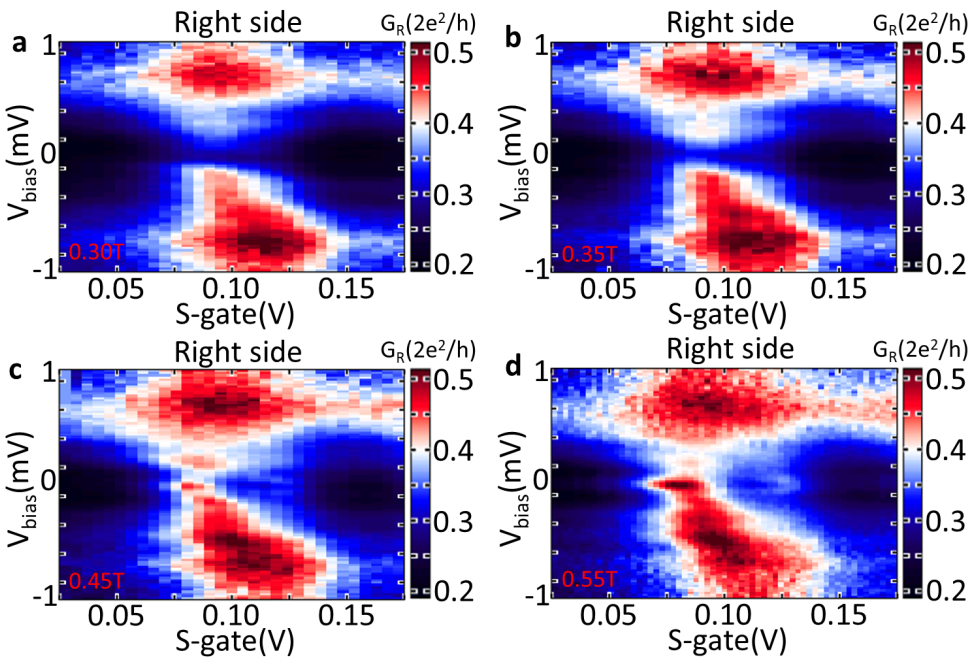

Figure 6.7: **S-gate dependence of the localized state R1 at finite magnetic fields.** Different from the behavior of delocalized states, right localized state R1 evolves into a ZBCP around 0.45 T(panel**c**. R1 also splits with magnetic field with a g-factor about 50

voltage vs. bias voltage at different fields. The magnetic field is pointing along the nanowire and satisfies the Majorana requirement as discussed in Chapter 2. As shown in Fig. 6.6(a), S1-S4 still emerge at same S-gate voltages at 0.1 T. However, at 0.3 T (Fig. 6.6(b)) and 0.5 T(Fig. 6.6(c)), states S2 and S3 apparently appear at different S-gate voltages on the two sides, manifesting the apparent decrease of correlation. The decreasing of correlation can also be noticed in S-gate vs. T_L scans at finite fields. As shown in Fig. 6.19, delocalized states on the right side show decreasing T_L dependence, i.e. nonlocal dependence, with increasing magnetic fields. Eventually at 0.8 T, most of the states on the two sides appear at different gate voltages (Fig. 6.19(c)).

We also study the field dependence of the right localized state R1. As presented in Fig. 6.7, R1 splits with field and evolves into a ZBCP above 0.4 T. The splitting behavior of

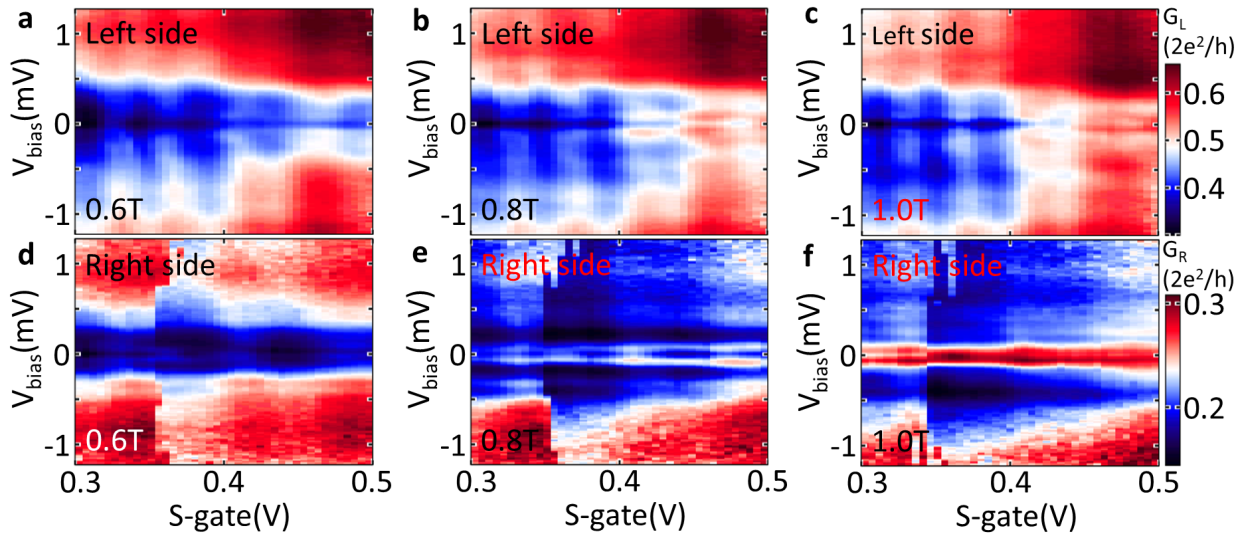

Figure 6.8: **S-gate dependence of the delocalized state at high magnetic fields. a-c**, Scans from the left side show low energy states develop with increasing fields. **d-f**, Right side scans show ZBCPs or split peaks develop around 0.8 T and extend to cover all the S-gate range at 1 T. Such ZBCPs, however, are missing on the left side.

R1 can also be seen in S-gate vs. fields scan (Figs. 6.20), which exhibits a g-factor about 50. Delocalized states also split but with smaller g-factor (Figs. 6.20). That observation is consistent with the assumption that localized states have lower k_F and thus stronger spin splitting for a given subband. That is because Zeeman energy appears within the square root along with the spin-orbit coupling in the energy spectrum [20], as k_F grows the Zeeman contributes less and less when spin-orbit coupling is much larger than Zeeman energy at low fields.

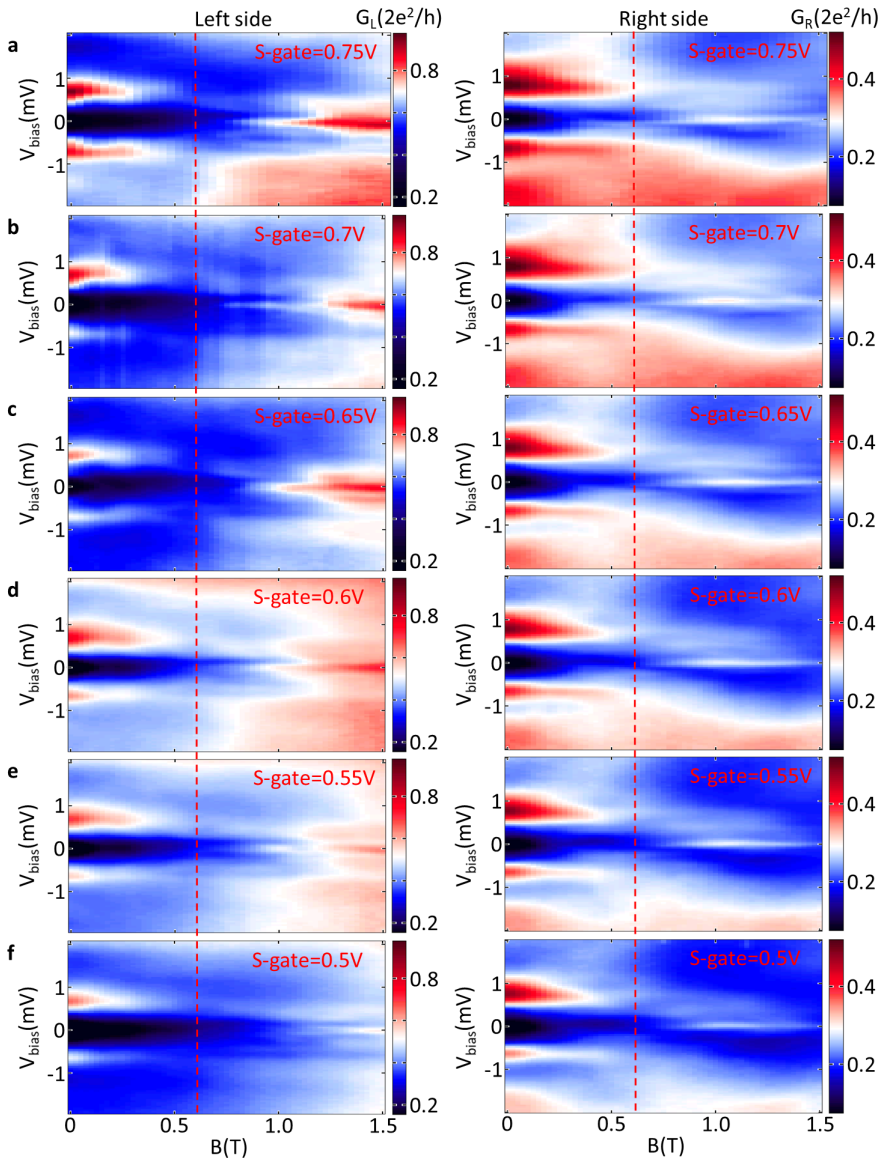

Figure 6.9: **ZBCPs at high magnetic fields on both sides** Here we present magnetic field scans for S-gate = 0.5 V to 0.75 V when T_L = -0.15 V and T_R = 0.09 V. As shown in the left panels, the onset fields of the ZBCPs on the left side change to higher fields when S-gate is reduced. And the ZBCPs also exhibits splitting features at S-gate = 0.55 V and S-gate = 0.5 V. On the right side, however, the ZBCP onset and splitting do not generally match the left side manifestations.

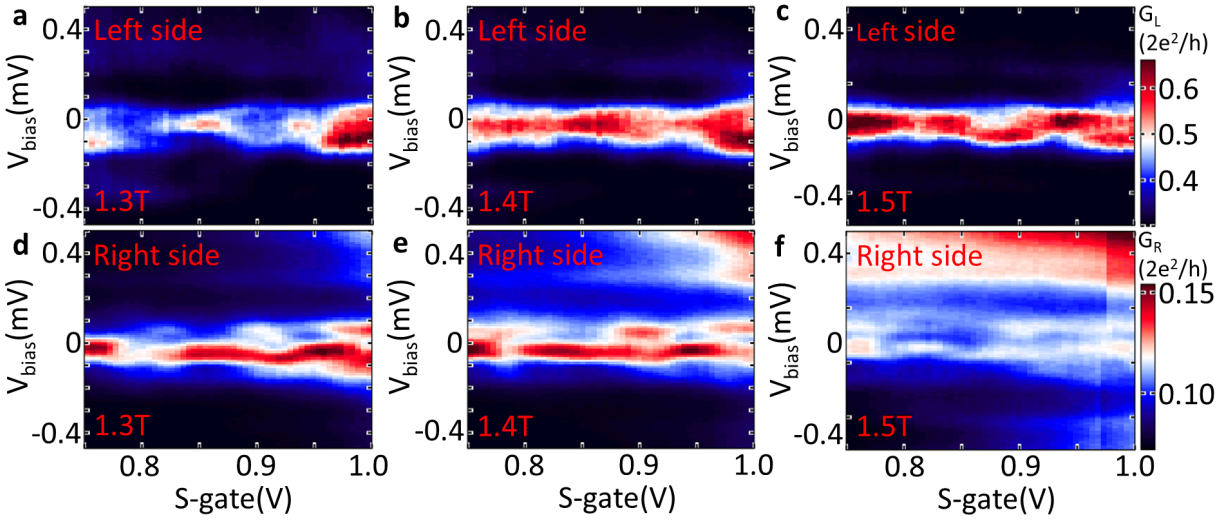

Figure 6.10: **ZBCPs at high magnetic fields on both sides extended. a-c**, for S-gate = 0.75 V to 1 V, differential conductances G_L and G_R as functions of S-gate voltage and bias voltage show ZBCPs on both sides. Those ZBCPs can not be traced to any delocalized states at low fields and do not exhibit any clear correlation between both sides.

At higher magnetic fields for the same S-gate regime(Fig. 6.8), low energy states develop and eventually form into ZBCPs around 0.9 T on the right side. On the left side, however, no prominent ZBCP has been observed. It is worth noting that for more positive S-gate voltage, ZBCPs are a generic feature of the both sides at high fields. For example, Fig. 6.9 presents a series magnetic fields scans when S-gate is fixed between 0.5 V to 0.75 V. While ZBCPs do appear on both sides and persist for a significant range of fields, the two sides show different onset fields for ZBCPs except for S-gate = 0.6 V (See Fig. 6.21). With identical onset fields for only one S-gate setting, it is impractical to make any claim about the correlation between the two sides. Similarly, for S-gate = 0.75 V to 1 V, S-gate vs. bias voltage scans for fields above 1.2 T (Fig. 6.10) also show ZBCPs on both sides. However, no correlation can be established again after careful examination. More field dependences of the two sides for S-gate > 1.5 V can be found in Fig. 6.22.

In summary, finite field weakens and eventually destroys the correlation we identified at zero magnetic field, manifested by the loss of correlation and nonlocality of the delocalized

states. At higher fields and for more positive S-gate voltage, ZBCPs appear on both sides. Those ZBCPs, however, fail to show correlation between the two sides. It is more likely those ZBCPs are due to trivial states localized near the tunnel barriers.

6.6 Near Quantized Zero Bias Conductance Peaks in Three-Terminal Devices

As we discussed in chapter 2, The tunneling process via an MBSs is called Andreev reflection, where an electron at energies less than the superconducting gap enters a superconductor from a normal state material. The incident electron forms a Cooper pair in the superconductor with the retroreflection of a hole, which has opposite spin and velocity to the incident electron. Due to the Majorana symmetry (particle equals antiparticle), tunneling amplitudes of electrons and holes via MBS are equal, which leads to a perfect resonant tunneling. And as the result, ZBCPs due to MBSs have unitary conductance of $2e^2/h$. Also due to the Majorana symmetry, this perfect quantization could survive disorder, interactions, and varying tunneling strength[37, 73, 1]. Finite temperature and finite system size[83, 101, 102, 92], however, may destroy the quantization. Approximate quantization may still be accessible when tunnel coupling dominates over both temperature and Majorana splitting. A tunneling rate-independent conductance is then expected at a nearly quantized level[1]. Conductance quantization was once thought a unique feature of MBSs comparing to other low energy states. Recent development of theory, however, shows approximate conductance quantization maybe achieved without Majorana modes by fine-tuning trivial low energy states[39, 40].

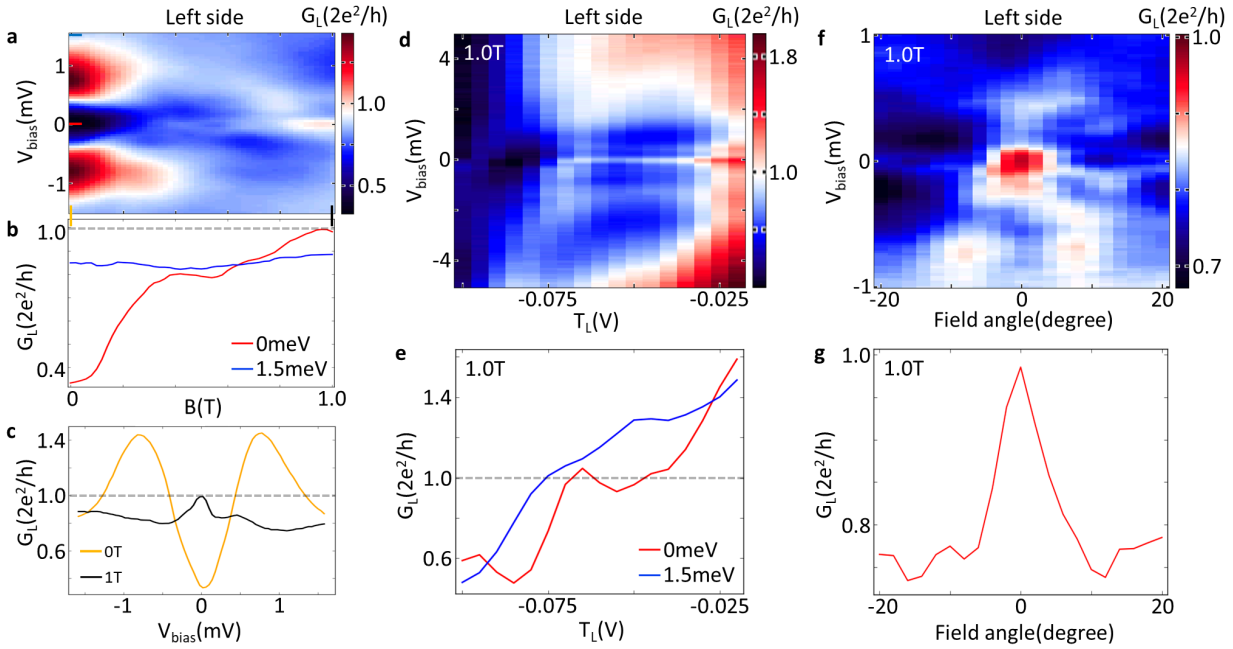

Figure 6.11: **Nearly quantized zero bias conductance peak on the left side.** **a**, Magnetic field dependence for S-gate = -0.17 V, T_L = -0.045 V and T_R=-0.105 V. The field direction is parallel to the nanowire. **b**, Linecuts taken at $V_{bias} = 0$ and 1.5 meV from **a**. **c**, Bias voltage linecuts from **a** at 0 T and at 1 T show the shape of the gap and the nearly quantized ZBCP. **d**, Tunnel-gate T_L dependence of the ZBCP. **e**, Linecuts taken at $V_{bias} = 0$ and 1.5 meV from **d**. A conductance plateau of nearly $2e^2/h$ associated with the ZBCP appear at zero bias, while the conductance above the gap evolve monotonically. **f**, Field angle dependence of the ZBCP at 1 T. 0 degree means the field is parallel to the nanowire and perpendicular to the spin-orbit field. **g,** linecut at zero bias from **f** shows a small deviation from 0 degree results in the drop of conductance from the quantized value. Note a contact resistance of 4 kΩ is subtracted.

In the more negative S-gate regime of device A. We find ZBCPs appear on the left side at finite fields with conductance close to the quantized value. Fig. 6.11 presents the results in Majorana manner. As shown in Fig. 6.11(a), when S-gate is fixed to -0.17V, magnetic fields scan shows a soft gap without resonances at low bias near zero field. At B ¿ 0.3T, conductance resonances are observed near zero bias: they are either a ZBCP or a split peak around zero bias. The peak conductance increases as the magnetic field increases and reaches the value of $2e^2/h$ near B = 1.0 T while the conductance beyond the gap remains nearly unchanged (Fig. 6.11(b)). In Fig. 6.11(c), bias voltage linecuts at 0 T and 1 T show the shape of the gap and the ZBCP. The ZBCP in Fig. 6.111(c) has a full width at half maximum of 150 μeV and reaches a conductance of nearly $2e^2/h$ after correction for contact resistance. The peak prominence above the background is of order $0.4*e^2/h$. It is worth noting that without correcting for any unknown contact resistances in the device, we find a peak value of $0.8*e^2/h$, and to achieve exact quantization, we have to correct for 4 kΩ series resistance based on the device conductance at saturation regime (see Fig. 6.23). That resistance could be attributed to the two interface resistances between nanowire and metals. The issue of unknown contact resistance is generic to all experiments where the exact quantization is not independently established (see chapter3 for an extended discussion).

To study the behavior of this ZCBP against barrier transmission, we set the magnetic field to 1 T and vary the voltage on T_L(Fig. 6.11(d)). The ZBCP only appears above T_L = -0.07 V and is stable for a finite range of T_L. When the ZBCP first appears, it immediately reaches its peak conductance of nearly $2e^2/h$, and maintains this conductance for a small range of T_L until the ZBCP conductance increases above the quantized value predicted for Majorana modes (Fig. 6.11(e)). The Majorana conductance may exceed $2e^2/h$ only if the barrier has multiple transmitting channels[1], and indeed here the above-gap conductance reaches beyond $2e^2/h$ for more positive T_L.

Another regular check for Majorana ZBCP is its behavior as a function of magnetic field angle with respect to the nanowire. Majorana states are predicted to appear only when the applied field is orthogonal to the effective spin-orbit field, previously measured to be perpendicular to the nanowire [12]. As shown in Fig. 6.11(f), the ZBCP on the left side reaches $2e^2/h$ when the magnetic field is parallel to the nanowire and perpendicular to the

spin-orbit field. Notably, a deviation of a few degrees results in the splitting of the ZBCP and a drop in conductance. More magnetic field anisotropy data can be found in Fig. 6.24.

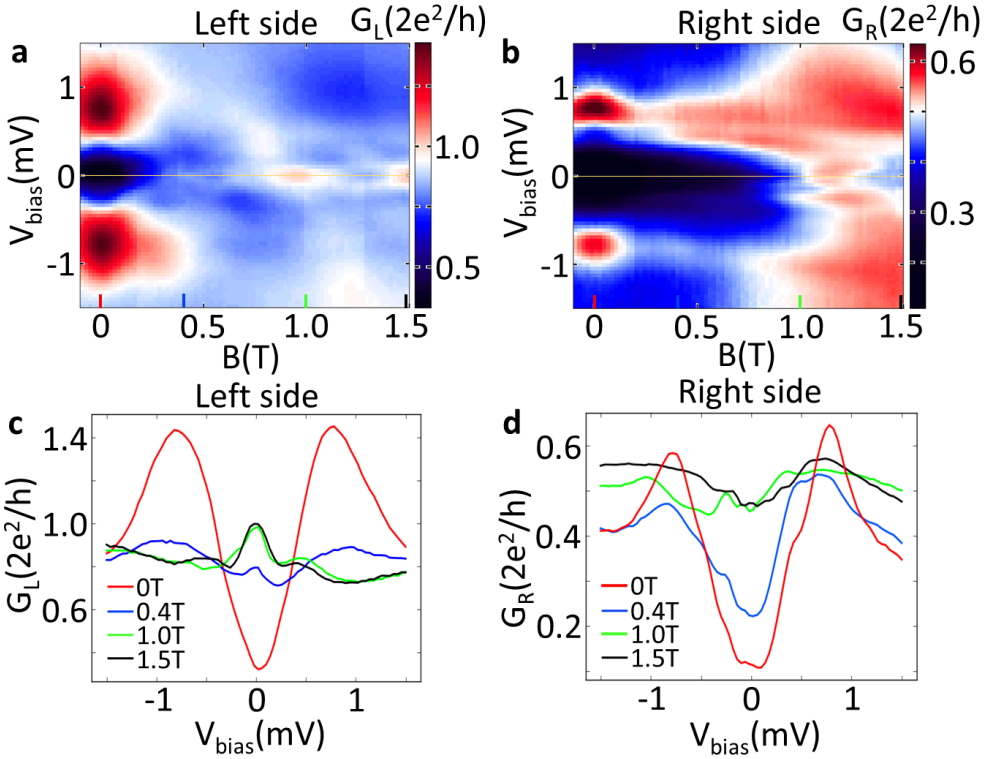

Figure 6.12: **Absence of zero bias conductance peak on the right side.** **a** and **b**, Magnetic field dependence of the subgap states on the two sides from the same dataset of Fig. 2(a) now in expanded field range, where S-gate = -0.17 V, T_L = -0.045 V and T_R=-0.105 V. A contact resistance of 4 kΩ is subtracted for the left side. **c** and **d**, Bias linecuts at 0 T, 0.4 T, 1.0 T and 1.5 T taken from **a** and **b** respectively.

As the way presented in Fig. 6.11, this ZBCP is consistent with Majorana theory, which dictates the Majorana ZBCP should emerge at finite magnetic field applied along the nanowire, persist in magnetic field, reach a peak height of $2e^2/h$, and be independent of tunnel barrier strength. If this ZBCP was shown in a two-terminal measurement, it will be hard to decisively conclude whether its due to Majorana or not, giving the existence of other alternative explanations for similar features. But here, since we are measuring in a three-terminal device, the other probe could provide important information by verifying the existence of the accompanying MBS on the other end of the nanowire segment. The simultaneous examination of conductance on the other side of the device, however, reveals a significant deviation from the basic Majorana picture: no ZBCP is observed on the right side to accompany the left-side ZBCP from Fig. 6.10. Fig. 6.12(a) originates from the same dataset as Fig. 6.11(a), but now we reveal a larger magnetic field range. Apart from the nearly quantized ZBCP described in Fig. 6.11, another peak splitting is observed at 1.2 T followed by another region of a $2e^2/h$ ZBCP around 1.5 T. Fig. 6.12(b) shows the simultaneously acquired conductance from the right side. While subgap resonances are also observed at finite fields, there is no quantized ZBCP, and in fact no ZBCP of any height is observed on the right side in this regime upon scanning T_L (more information in Fig. 6.25). Linecuts taken from Fig. 6.12(a),(b) show that the left side has high conductance ZBCPs at 0.4 T, 1.0 T and 1.5 T, while the right side does not have ZBCPs at those magnetic fields. Those observations from the right side of the device significantly weaken the possibility of a Majorana origin for the nearly quantized ZBCP. Since there is no Majorana on the right edge of the S contact, otherwise we should be able to observe it, little space is left for another Majorana within the 400 nm S-lead segment of the nanowire. And if there is another Majorana within that nanowire segment, we expect Majorana overlap, as the S-lead segment is only 3 wire diameters long, and peak splitting. However, the peak we observed on the left side remains at zero bias for an extensive field 0.5 T. Moreover, near that negative S-gate setting, no delocalized states have been observed, indicating likely stronger barriers inside the nanowire, which is not in favor of nonlocal MBS (See Fig. 6.26 and Fig. 6.27 for more information). Thus we conclude it is unlikely the ZBCP we observed is due to well-separated MBSs in that device and interpreting the observed ZBCP as overlapped Majorana hinges on

a multitude of assumptions, each of which has to play out favorably in just the right way. It is more likely the ZBCP is originated from topologically trivial states, e.g Andreev bound states[40] or 'class D' peaks[39].

6.7 Conclusions

In summary, we fabricated three-terminal hybrid nanowire devices with all the ingredients for MBSs. In three devices, we observed delocalized states. The general properties of those states are: (i) appearing on both sides at low magnetic fields as resonances extended both inside and outside the induced gap. (ii) showing same S-gate and barrier gates dependence. (iii) emerging only in regime with positive S-gate voltages. While the delocalized states indicate our systems have no strong barriers inside the hybrid region and could support extensive wavefunctions, the correlation between the two sides do not survive finite magnetic fields. Moreover, localized states also appear within the same S-gate regime of the delocalized states, indicating disorder induced localized wavefunctions do exist in the nanowire-superconductor hybrid region. In high magnetic fields and positive S-gate voltage regime, we found ZBCPs are generic feature on both sides. Those ZBCPs, however, are not related to the delocalized state and show no clear correlation between the two sides. We conclude those ZBCPs are most likely due to topologically trivial states localized near the two tunneling barriers. Although correlated ZBCPs are not observed in this work, three-terminal geometry shows it is a powerful method of diagnosing the localization of wavefunctions. By examining the simultaneous conductance on the right side, we exclude that we may have a ZBCP due to well-separated MBS on the left side, while the ZBCP show magnetic fields and gate dependence in agreement with Majorana theory and its conductance is close to $2e^2/h$. Based on our results, we suggest that all the possible tunneling signature of MBSs should be examined in the three-terminal geometry to exclude the origin of localized wavefunctions. To observe correlated MBSs signals, future improvement in growth and fabrication are necessary.

6.8 Supplementary

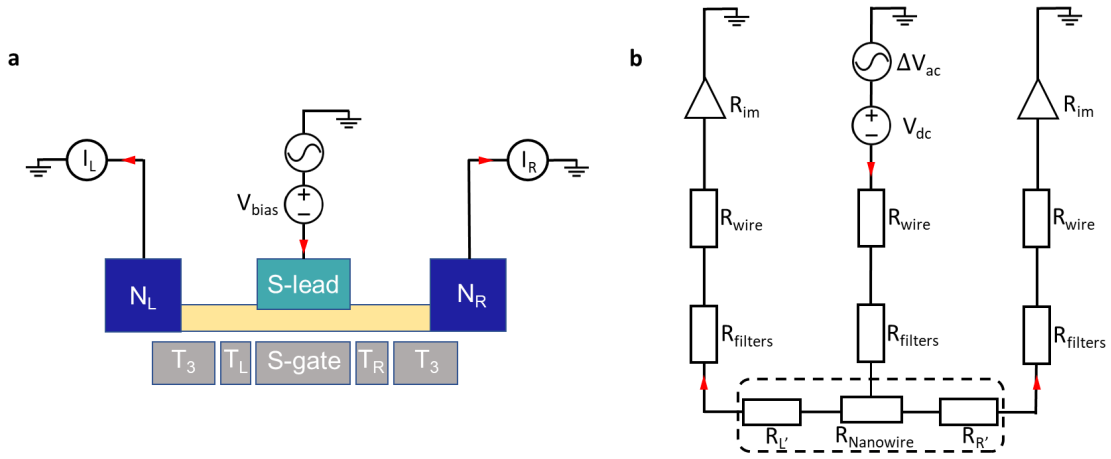

Figure 6.13: **Three terminal measurement setup. a**, Schematics of the device and measurement setups. Red arrows indicate the direction of dc current flow for positive bias. The source-drain voltage is applied through the superconducting contact, current and differential conductance are measured simultaneously at two normal contacts. The two wider tunnel gates are connected together as T_3. **b,** Simplified measurement circuit diagram representing all elements of the circuit as resistors. $R_{filters}$ is the resistance of RC filters and R_{im} is the input impedance of the current amplifier. Resistances within the dashed box are on chip. They are left and right nanowire segment resistances, R_L and R_R, as well as superconductor-semiconductor and superconductor-normal metal contact resistances, which are indicated by $R_{L'}$ and $R_{R'}$. The exact values of contact resistances are unknown, but they can be estimated from saturation current at positive gate voltages.

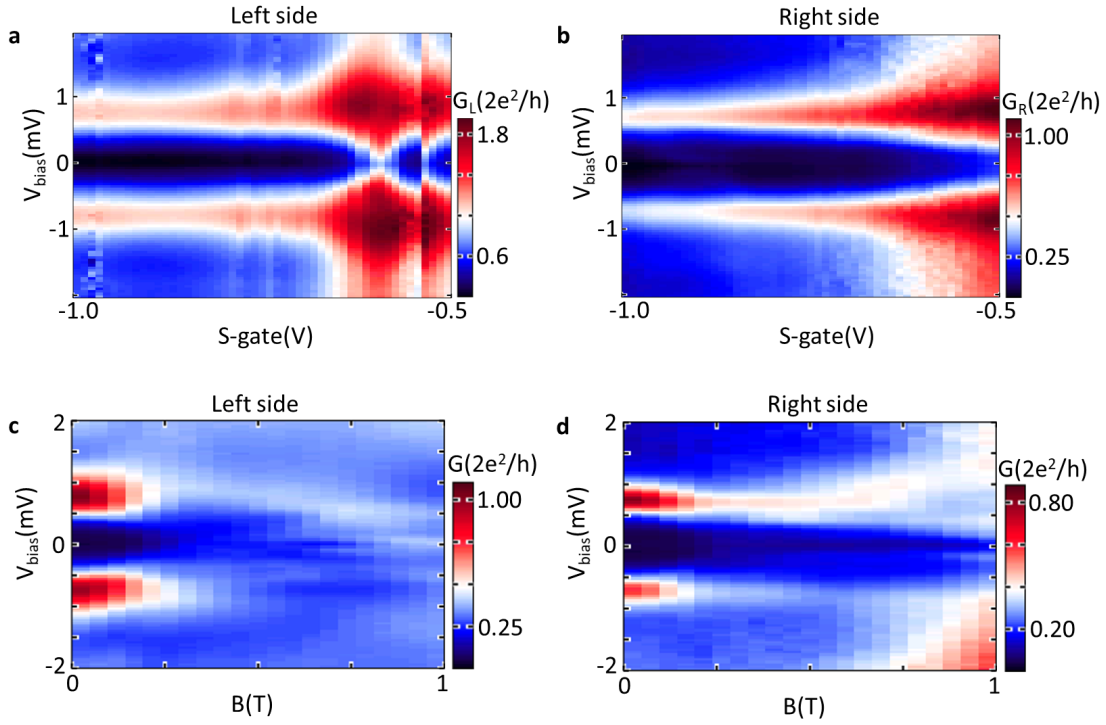

Figure 6.14: **Induced gaps at negative S-gate voltage in device A. a** and **b**, S-gate vs. bias voltage scans at zero magnetic field. Both sides show a soft but clean regime with induced gaps with magnitud of 750-800 μeV. Induced gap traces in Fig.6.1(b) are taken at S-gate = -0.75 V. **c** and **d**, Magnetic fields dependence of the induced gaps when S-gate is set to -0.75 V. The strong gap edges remain open to at least 1 T while low energy states develop on both sides.

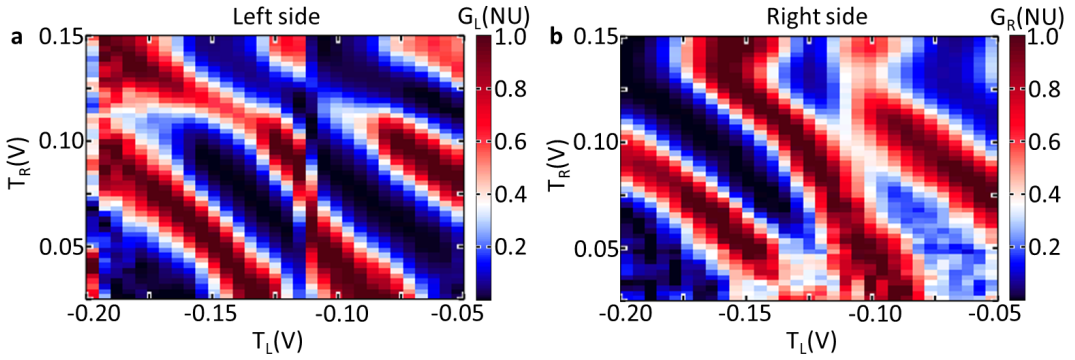

Figure 6.15: **Tunnel gate T_L vs T_R scans at zero magnetic field in device A.** **a** and **b**, T_L vs T_R scans at zero magnetic field when S-gate is set to 0.4 V. Delocalized states show dependence on both sides, manifesting the corresponding wavefunctions tunable with both tunnel gates.

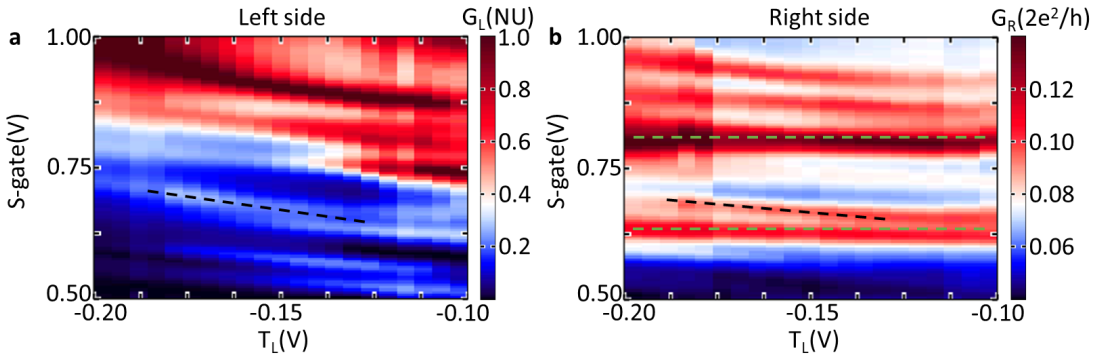

Figure 6.16: **Delocalized states at more positive S-gate voltage in device A.** **a** and **b**, differential conductances G_L and G_R as functions of S-gate voltage and T_L voltage at zero magnetic field. For the left side scan, conductance is normalized for each column. In this regime, delocalized states and localized states are mixed together. Delocalized states, e.g. black dashed line, appear on both sides and show dependence on both sides. Localized states, e.g. green dashed lines, only emerge on one side.

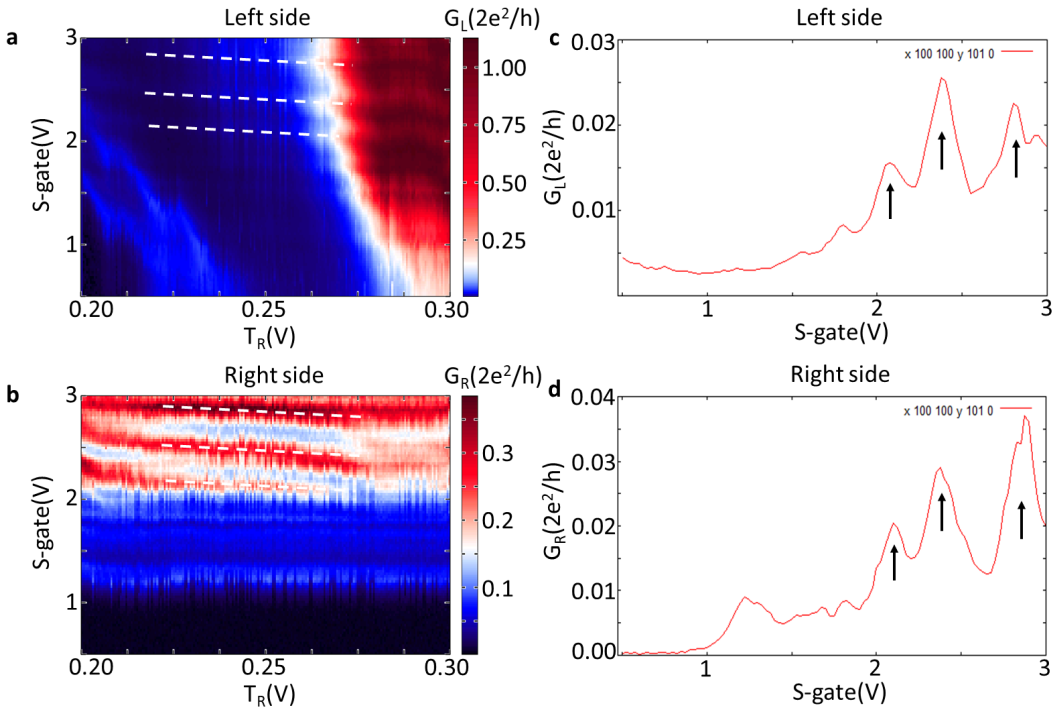

Figure 6.17: **Delocalized states in device B. a** and **b**, differential conductances G_L and G_R as functions of S-gate voltage and T_R voltage at zero magnetic field. In this device, delocalized states emerge when S-gate is set above 1.5 V. We indicate three delocalized states here by while dashed lines. **c** and **d**, linecuts taken at $T_R = 0.25$ V. delocalized states are indicated by black arrows.

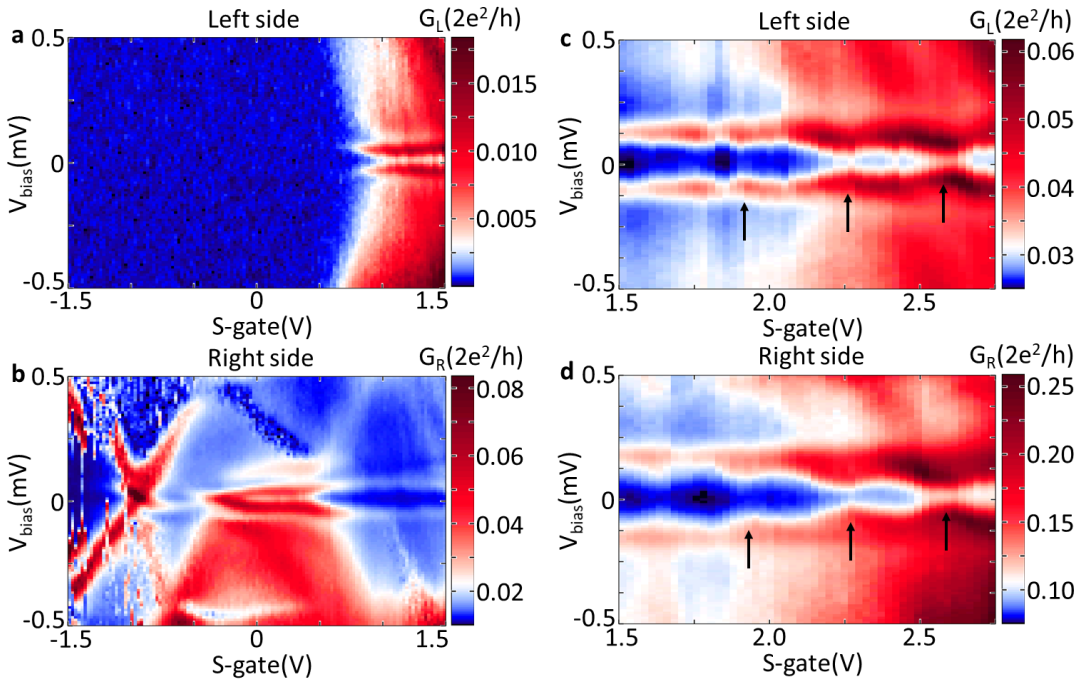

Figure 6.18: **Delocalized states in device B extended.** In S-gate vs. bias voltage scans, the two sides show distinct states when S-gate < 1.5(panel **a** and **b**) and delocalized states(indicated by black arrows) only appear when S-gate > 1.5 V(panel **c** and **d**).

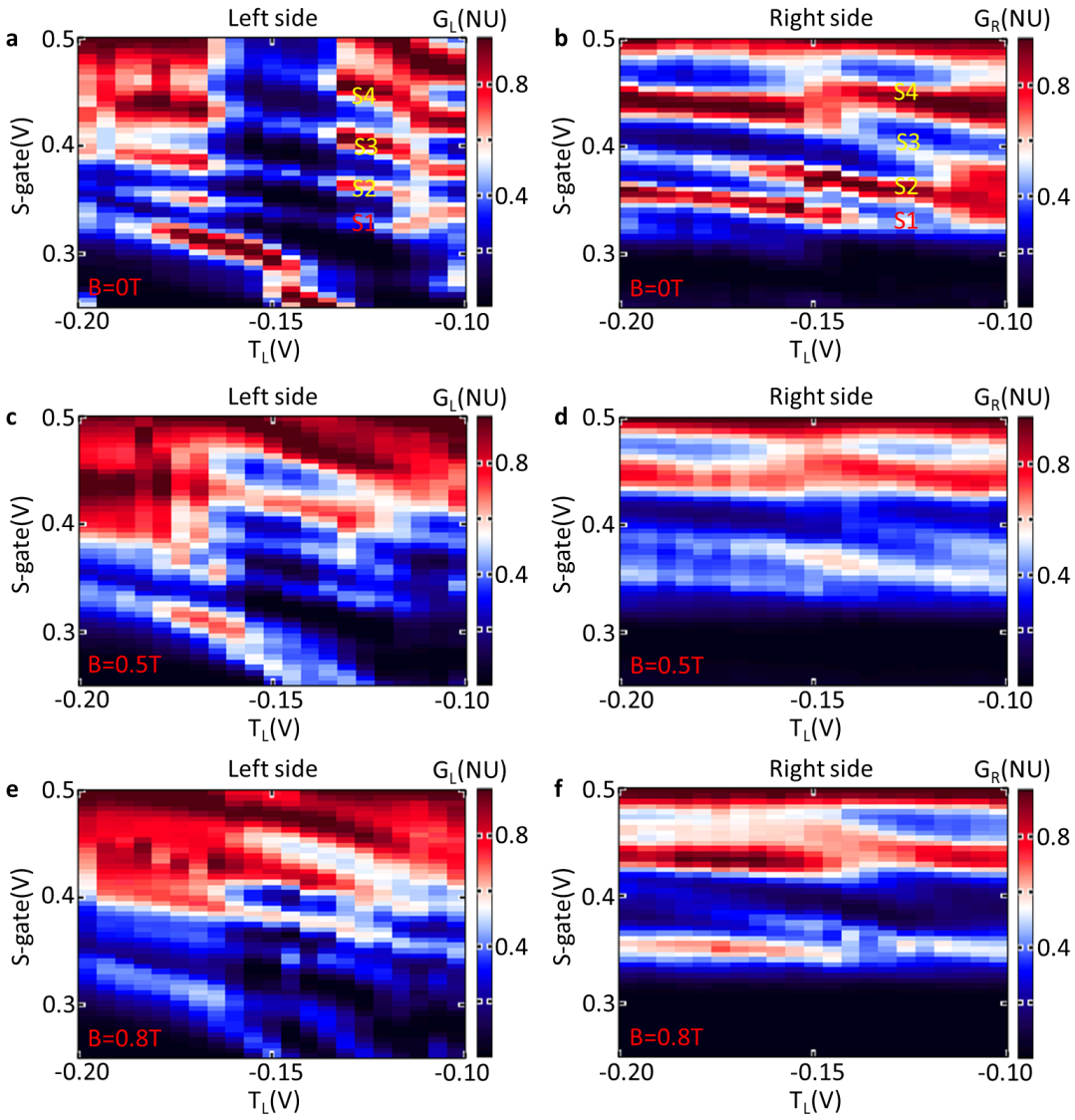

Figure 6.19: **Delocalized states at finite magnetic fields in device A extended. a and b**, Zero bias differential conductance G_L and G_R as functions of S-gate and T_L voltages at zero magnetic field, showing the delocalized states S1-S4. **c and d**, Similar scans as panel **a and b** but at 0.5 T. While states on the left side generally remain the same, States S1 and S3 become weaker and almost disappear on the right side. **e and f**, similar scans at 0.8 T. The two sides show distinct states. While some states on the right side still show T_L dependence, there is no clear correlated states on the left side. In each scan, conductance is normalized for each column to show states clearly.

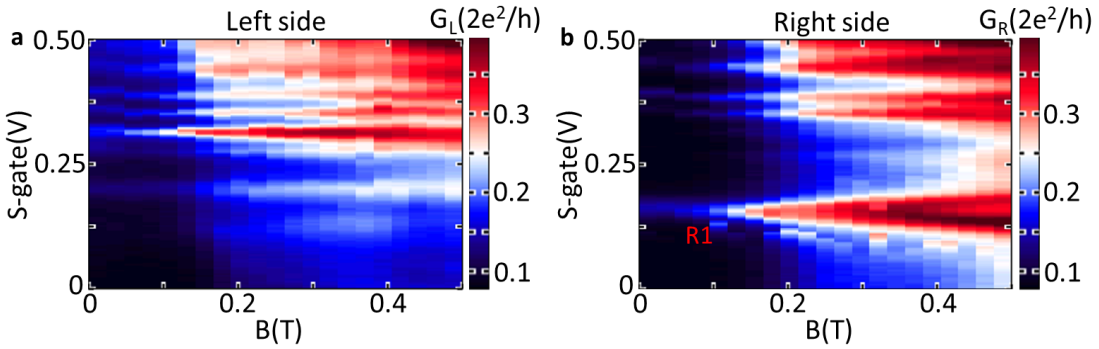

Figure 6.20: **Magnetic field dependence of the delocalized and localized states in device A. a and b**, Zero bias differential conductance G_L and G_R as functions of magnetic fields and S-gate voltage. Right localized state R1 show clear splitting with magnetic field and exhibit a g-factor about 50. Delocalized states appear between S-gate = 0.3V to 0.5V and show less clear splitting due to smaller g-factor.

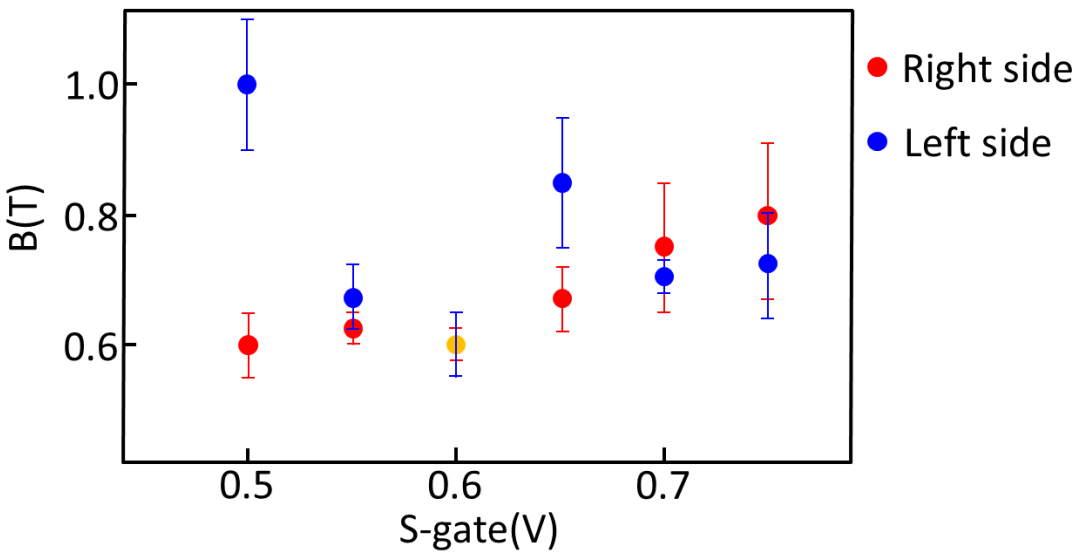

Figure 6.21: **Plots of the onset fields of ZBCP in Fig.6.9**, the onset magnetic fields of ZBCP for left and right sides extracted from Fig.6.9. Only at S-gate = 0.6 V, the two sides show the same onset field(orange circle). The error bars are determined by the field scan resolution.

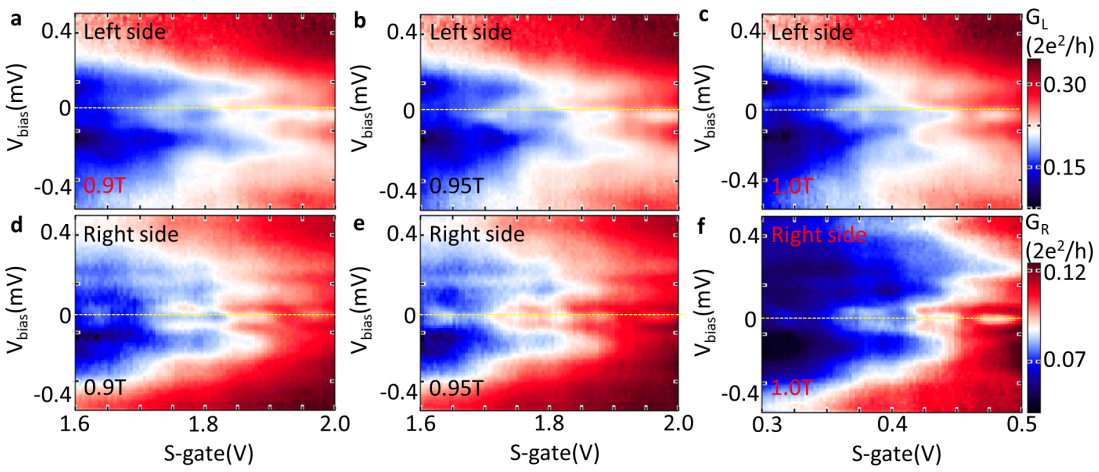

Figure 6.22: **More positive S-gate regime at high magnetic fields in device A .** For S-gate= 1.6 V to 2 V, ZBCPs and low energy states appear on both above 0.9 T. While the two sides show similarities for the general feature, no correlation can be established after careful examination. Yellow dashed lines are guide to zero bias.

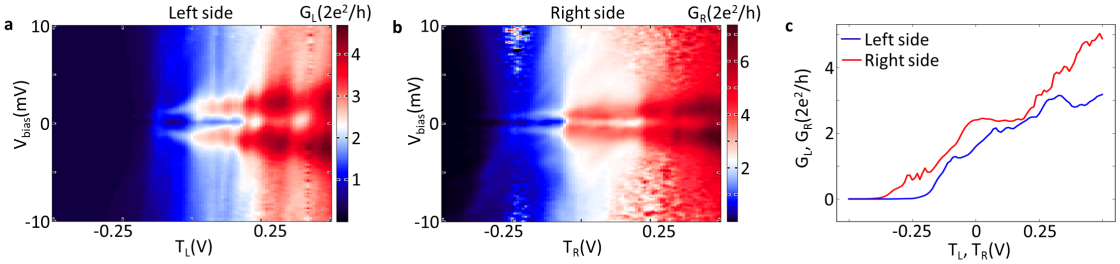

Figure 6.23: **Additional zero field tunnel barrier data from device A. a** and **b**, Larger barrier gate scans from the left and right sides respectively, while S-gate is set to 1 V. The two sides show similar barrier gate dependence and overall transparency. Note the left side reaches $3*2e^2/h$ at saturated regime, indicating a possible contact resistance of 3-4 kΩ. **c,** Pinch off traces at V_{bias} = 10 meV from **a** and **b**.

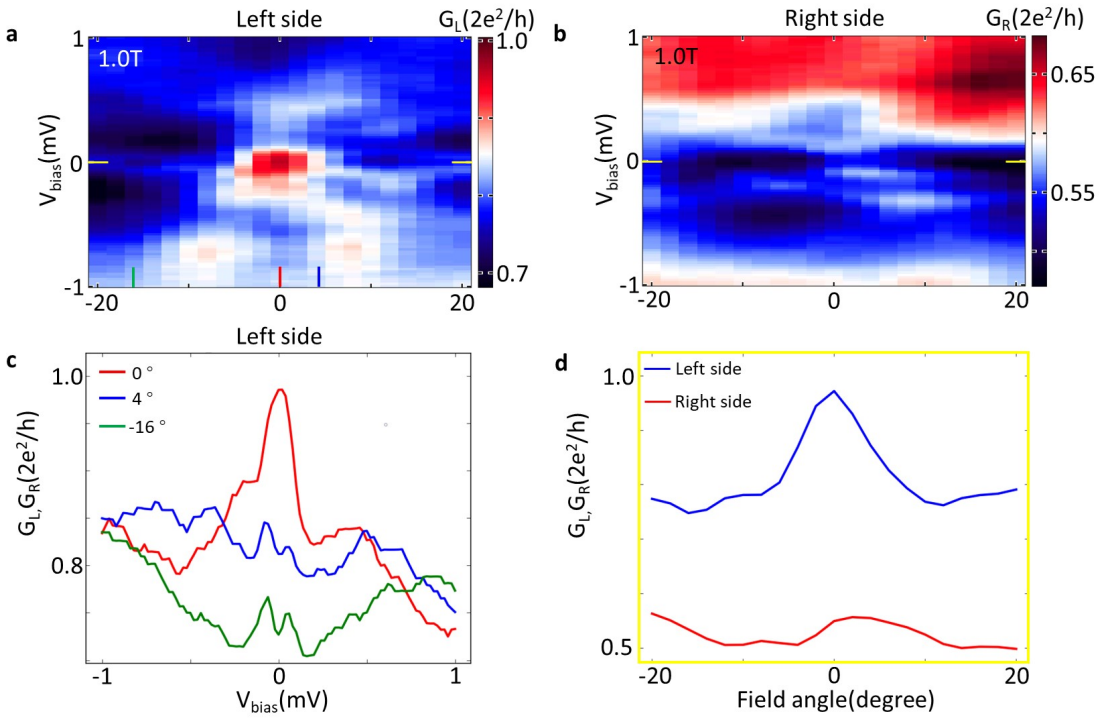

Figure 6.24: **Magnetic field angle dependence of the nearly quantized ZBCP and subgap states on both sides in device A. a** and **b**, Differential conductance G_L and G_R as functions of field angle and source-drain voltage when T_R = -0.105 V, T_L = -0.04 V, S-gate = -0.18 V. Note the contact resistance of 4 kΩ is subtracted for the left side. The field is parallel to the nanowire and perpendicular to the spin-orbit field when the field angle is zero. On the left side, the ZBCP only exists and reaches $2e^2/h$ within a small angle around zero degree. On the right side, the subgap states are asymmetrical in field angle. Most importantly, no ZBCP is observed in the range -20 degree to 20 degree. **c**, Bias linecuts at 0, 4, -16 degree field angle from panel **a**. The ZBCP splits into two peaks when the field angle deviates from 0 degree. **d**, Zero bias linecuts show distinct behavior on the two sides: the zero bias conductance on the left side peaks at zero degree while the zero bias conductance on the right side remains almost unchanged.

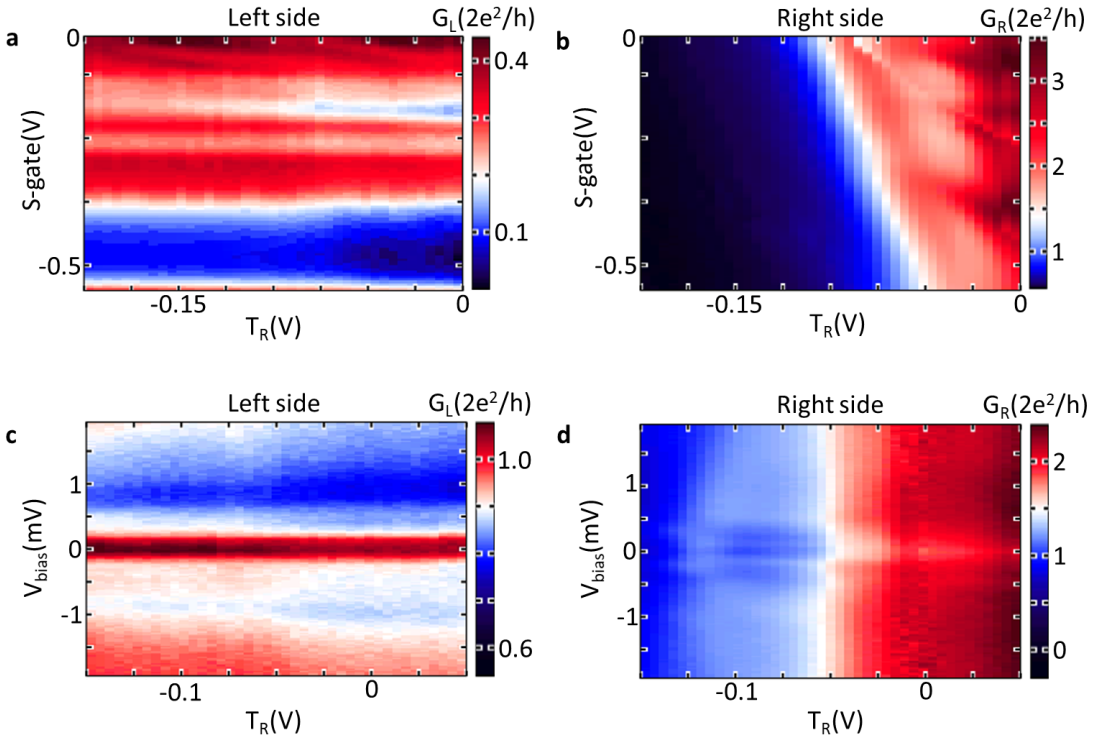

Figure 6.25: **Effect of T_R on the left-side-only ZBCP in Fig. 6.11 and Fig.6.12 . a** and **b**, Differential conductance G_L and G_R as functions of T_R voltage and S-gate voltage at zero field and zero bias when T_L is set to -0.04 V. This is the regime where we find the nearly quantized on the left side in Fig. 6.11 and Fig.6.12. The two sides show distinct states, which confirms the finding that there are only localized states in this regime. **c** and **d**, Differential conductance G_L and G_R as functions of source-drain voltage and T_R voltage at 1 T. While the T_R pinch off the right side, the ZBCP on the left side remains unchanged with conductance close to $2e^2/h$. Notably, there are also states near zero bias on the right side when T_R is below -0.05 V. However, they never form a ZBCP.

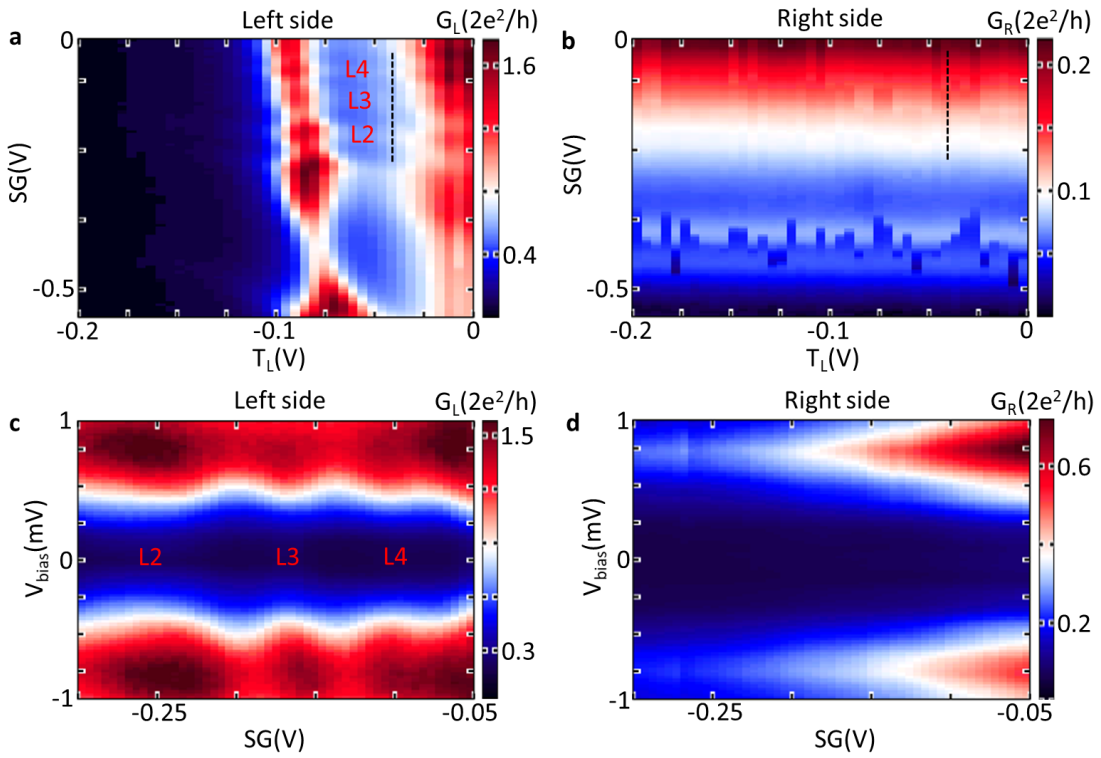

Figure 6.26: **Localized states in negative S-gate regime in device A.a** and **b**, Zero bias differential conductance G_L and G_R as functions of T_L voltage and S-gate voltage(-0.5 V to 0 V) at B = 0 T, while T_R is set to -0.15 V. This is the regime where we find ZBCPs close to quantization on the left side in Fig. 6.11. While there are three apparent resonances(labeled as L2, L3, L4) on the left side along the black dashed line, no similar features are observed on the right side. These scans confirm the low probability of having well separated Majorana bound states in that region, given the variety of localized and uncorrelated states within the nanowire. **c** and **d**, Source-drain voltage vs. S-gate scans along the black dashed line in panel **a** and **b** showing the resonances on the left side and the absence of similar features on the right side.

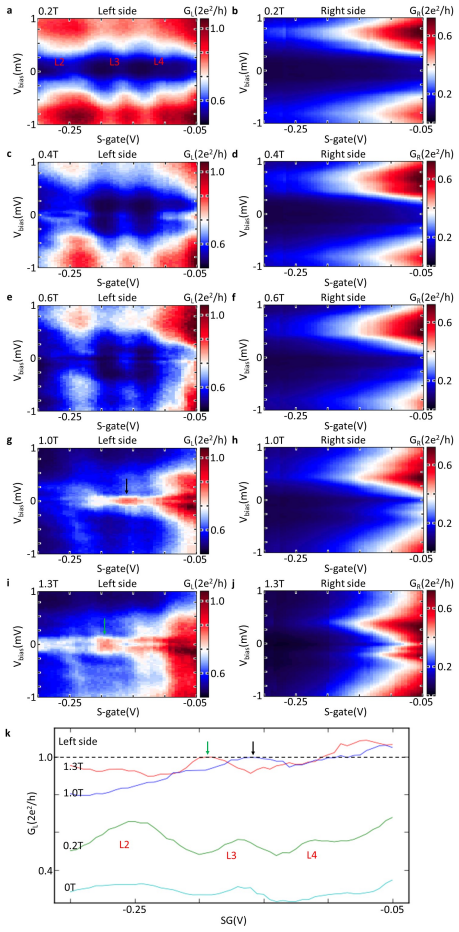

Figure 6.27: **Evolution of the nearly quantized ZBCP in magnetic fields. a-j**, Source-drain voltage vs. S-gate scans of the same regime of Fig 6.26(a)(b) at different fields. The gate settings are T_L = -0.045 V and T_R = -0.105 V. On the left side, subgap states and ZBCPs appear around B = 0.3 T. The height of the ZBCPs reaches $2e^2/h$ at 1 T (panel **g**) and again at 1.3 T (panel **j**). The contact resistance of 4 kΩ is subtracted for the left side. On the right side, sub-gap states develop at higher fields. Most importantly, no ZBCP is observed on the right side within the field range investigated. **k**, Zero bias linecuts taken from Fig. 6.26(e), and panel **a**, **g**, **i** show conductance increase with increasing magnetic field and reach $2e^2/h$ at 1 T and 1.3 T.

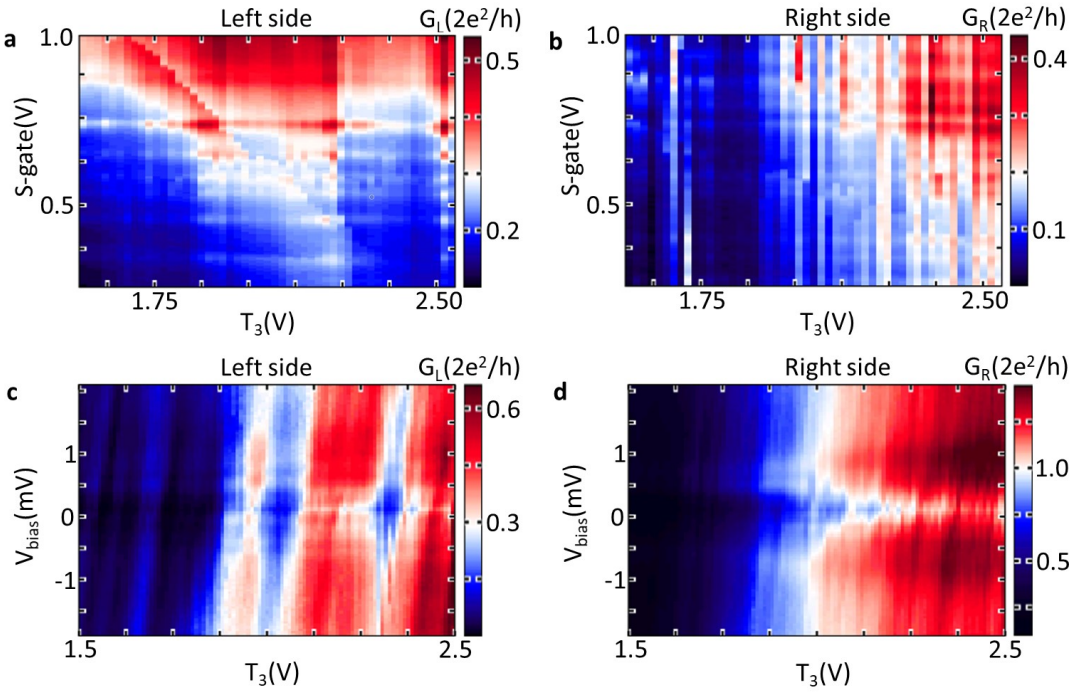

Figure 6.28: **Effect of gate** T_3**.** The two wider barrier gates are connected and controlled by a single voltage T_3. For all other measurements in this paper, T_3 is set to above 1.5 V to facilitate high transparency. **a** and **b**, Differential conductance G_L and G_R as functions of S-gate voltage and T_3 voltage at zero bias and zero magnetic field, while S-gate = 1 V, T_L = -0.15 V and T_R = 0.1 V. The resonances we observed in S-gate scans are independent of T_3, indicating the associated wavefunctions live far away from T_3. T_3 also tune different sets of resonances on the left and the right side, which can also be seen in the source-drain voltage vs. T_3 scans (panel **c** and **d**). The gate settings are S-gate = 1 V, T_L = -0.1 V and T_R = 0.075 V. Those states are independent of S-gate, indicating the existence of more dots above T_3.

7.0 Conclusions and Outlook

7.1 Introduction

As the last chapter of this thesis, I will first summarize the results of our work and the improvements we have made in pursuing the evidence of Majorana bound states (MBSs). A brief summary of the state of the art will be given for both experiments and theories. In the final section, my outlook for the future experiments is presented.

7.2 Conclusions of the Thesis

Following the theoretical proposal [10, 11] and early experiment results [12, 103, 104, 105, 106], we have spent our effort on providing an unambiguous evidence of Majorana bound states (MBSs) in quasi-1D nanowire-superconductor hybrid systems. The main findings of each chapter are summarized below.

In chapter 4, we focused on the improvement of the required ingredients for creating MBSs. We first optimized the deposition parameters to increase the T_C of the NbTiN films and obtain low film stress. Several etching processes to remove native oxide on InSb nanowires have been tested. Based on the results, we focus on the most promising combination: sulfur passivation plus a short time argon sputter cleaning. By fine tuning the sulfur passivation and sputter cleaning parameters, we achieve highly transparent nanowire-metal interfaces, which allowed us to observe conductance quantization in quantum point contact and multiple Andreev reflection between two nanowire-superconductor interfaces. By the measure of suppression of conductance within the gap and the shape of the gap, the best induced superconducting gaps in our testing devices were close to the gaps of molecular beam epitaxy (MBE) grown Al film on InAs nanowires. However, the yield of hard gap is lower in our devices and we didn't have the best gap in our Majorana devices. Apart from the methods to get better induced gaps, we also improved local electrostatic gates to enhance

the control of chemical potential inside the nanowire.

With the above improvements, we studied MBSs in the two-terminal geometry. As presented in chapter 5, we first mapped out a phase diagram for our topological superconductor. By tracing Majorana-like ZBCPs in chemical potential and magnetic field space, we successfully identified the ZBCP phase of the nanowire-superconductor hybrid device. The result is in good agreement with the calculations for a finite-length topological nanowire, which harbors two coupled MBSs. Our work shows ZBCPs can be predictably generated by tuning chemical potential and magnetic field. While that data supports the existence of coupled MBSs, we also found the widely studied MBS signal, i.e. zero bias conductance peaks (ZBCPs) at finite fields, is a ubiquitous feature in nanowire-superconductor hybrid systems [85]. Trivial ZBCPs, which are most likely due to Andreev bound states caused by inhomogeneity in the system, can really mimic the behavior of MBS induced ZBCPs [38, 41, 39, 80, 43]. While differences in gate dependence and field dependence do exist between the Majorana-like ZBCPs and the trivial ZBCPs, e.g. Majorana-like ZBCPs in chemical potential space grows with magnetic field, lack of other evidence, e.g. Majorana conductance quantization and ZBCP oscillations, prevents us from deterministically claim the existence of MBSs.

Due to the difficulty of distinguishing MBSs from other trivial states in two-terminal measurements, we switched to three-terminal geometry. With one more normal lead added to the other side of the nanowire, we aimed to gather more evidence of MBSs by studying the correlation between the two sides of the nanowire-superconductor hybrid region. For a hybrid region with length of 400 nm, we found delocalized states near zero magnetic field for positive S-gate voltages. These states were observed simultaneously on two sides and showed correlated gate dependence. While the existence of delocalized states suggests the device has the potential to host wavefunctions spanning all of the hybrid region, the presence of localized states and related theoretical simulation indicates the system still has moderate inhomogeneity. Moreover, finite field data shows the correlation between the two sides decreases with increasing fields. The signature of delocalized states, i.e. correlated resonance, becomes obscured below the field required for a topological phase. While ZBCPs do appear on both sides at high fields, they only accidentally exhibit the same onset field. In

most of the cases, the two sides show ZBCPs with different field and gate dependence, which indicates they are not from the same state and thus are not from well-separated MBSs.

Although our data do not support the existence of well-separated MBSs, three-terminal geometry is a powerful method of diagnosing the localization of wavefunctions. For one side of the three-terminal device, a ZBCP with conductance close to $2e^2/h$ emerges at finite fields at negative S-gate voltages. This ZBCP shows gate and field dependence similar to an MBS-induced ZBCP. However, we do not observe an accompanying peak at the other side of the nanowire at the identical settings. Considering that the hybrid region is only 4 times larger than the nanowire diameter, we are confident to claim the observed nearly-quantized ZBCP cannot be due to well-separated MBSs.

To sum up, we found evidence of coupled MBSs in hybrid nanowire-superconductor nanowire devices. The evidence, however, is not strong enough to unambiguously claim the existence of MBSs. In devices with similar configuration, we also found that non-Majorana ZBCPs are generic features at finite fields. Those trivial ZBCPs share behavior of MBS induced ZBCPs, and thus may not be disentangled from the signal of MBSs except perhaps in the three-terminal geometry.

7.3 Other Experiments Reporting Majorana Modes in Nanowires

As an active and fast growing area, a lot of related experimental results have been reported over these years. Many works have shown evidence of MBSs in nanowires with a two-terminal geometry, including Mourik et al [12], Rokhinson et al [103], Deng et al [104], Das et al [105] and Churchil et al [106]. Albrecht et al [90] and Deng et al [107] also reported Majorana non-locality in two terminal measurement. Other related experimental results include [108, 109, 110, 111]. Those works focused on the study of Majorana induced ZBCPs and supercurrent and showed results in agreement with some of the theoretical predictions.

In contrast to the two-terminal geometry, results from the three-terminal geometry are relatively scarce and no direct evidence of MBSs has been reported so far in that geometry. Some relevant three-terminal results in nanowires are works from Anselmetti et al [112],

Cohen et al [113] and Puglia et al [114]. While these works suggest correlation does exist between the two ends of the nanowire-superconductor hybrid region, clear indication of topological phase or MBSs is still to be established.

7.4 Recent Development of Theory

Apart from experiments, Majorana theory also experienced a rapid development and produced a lot of great works. Some of the works addressed the discrepancies between some experiments and theories, which include small height of the observed ZBCPs, missing of clear indication of gap closure and reopening and absence of ZBCP oscillations.

First, the small height (usually smaller than 0.5 $2e^2/h$) of the observed ZBCP can be explained by non-ideal tunnel barriers, non-uniform chemical potential inside the nanowire-superconductor hybrid region, finite temperature, soft gap and finite size of the device. These ideas have been demonstrated by the works of Rainis et al., Lin et al., Prada et al. and Pientka et al [92, 102, 83, 101].

Missing of gap closure and especially reopening, which indicates the emergence of topological phase at finite magnetic fields is an issue for most of the experiments. Stanescu et al [115] and others [92, 83, 101] suggest since the gap closure happens in the bulk of the nanowire-superconductor hybrid region, it may have a weak coupling to the tunnel probe and thus may be hard to be captured by the tunneling spectroscopy, which measures the local density of states near the tunnel barrier. Moreover, for a nanowire-superconductor region with finite length, Mishmash et al [116] argues the topological phase transition is turned into a cross-over instead of a sharp transition accompanied by gap closure and reopening.

Another common question in experiments is the absence or unclear oscillations [90, 108] of ZBCPs. One explanation for this issue might be the spin-orbit interaction strength is underestimated in the early theories. Instead of 50 μev as measured in quantum dot [51], Weperen et al [117] reported a much larger value of hundreds of μeV. Since stronger spin-orbit interaction leads to shorter Majorana coherence length, coupling between Majorana is suppressed with larger spin-orbit interaction strength. Furthermore, electronic interactions

with dielectric surroundings [93] and a steplike spin-orbit coupling [94] can also result in decays of Majorana oscillation as observed in some experiments.

While it seems most of the inconsistency between the simplest Majorana theory and experiment can be addressed by more detailed models, one consensus so far is that non-Majorana induced ZBCPs is a ubiquitous feature in Majorana devices and can really exhibit similar behavior to Majorana induced ZBCPs [41, 83, 79, 80, 81]. In particular, Woods et al [38] demonstrate Andreev bound states induced ZBCPs can arise due to inhomogeneity in systems with multi-band occupancy. Moore et al [40] show partially separated Andreev bound states, which can be viewed as overlapping MBSs, can generate signatures identical to MBSs in a two terminal-geometry. Pan et al [39] and Moore et al [40] illustrate topological-trivial ZBCPs can also exhibit approximate conductance quantization. Due to the difficulty in distinguishing MBSs from trivial counterparts, no deterministic claim can be made for the existence of well-separated MBSs to date.

7.5 Recent Development of Experimental Techniques

Experiments are always facilitated by the breakthrough in experimental techniques. In this section, I will briefly summarize technique advances in the related area.

For the early growth method of InSb nanowires [52], the nanowire length is limited by the InAs stem since arsenic evaporates during InSb growth. The foreign material of the stem may also be incorporated in the InSb segment. Recently, Badawy et al [53] reported a technique to grow InSb nanowires without any stems, resulting a significant enhancement of low-temperature electron mobility. For cleaning methods of the native oxide on nanowires, Webb et al [58] demonstrated a new method that uses hydrogen to clean the oxide in situ. By heating InAs or InSb nanowires in an hydrogen atmosphere, nanowire surfaces become clean and unreconstructed and the conductivity of individual nanowires is increased by 2 orders with metal contacts. Comparing to removal of the native oxide on nanowires post-growth, epitaxial growth of superconducting materials immediately after the growth of nanowire can provide a totally oxide free nanowire-superconductor interface. As first reported by

Krogstrup et al [70] with the combination of aluminum and InAs nanowires, that new route can yield atomically flat interface between nanowires and superconductor. Very hard induced gaps has been demonstrated with this technique [118]. After this, Gazibegovic et al [59] reported a bottom-up method to develop nanowire networks. This work also uses molecular beam epitaxy (MBE) to grow high quality aluminum film in situ and provide more flexibility than earlier nanowire crosses [119]. Since nanowire networks constitute a prerequisite for the synthesis of complex quantum devices, this work has profound significance for the future Majorana experiments, e.g. Majorana braiding. One downside in these two works, however, is that the Al film is very fragile, which prevents a direct contact being made on the film. Vaitiekėnas et al [71] reported a selective area growth method to solve that problem. By growing InAs nanowires in predefined SiO_x trenches, aluminum film can then be deposited on the nanowire as well as the substrate in-situ using MBE. Extra contact leads can be made on the aluminum film on the substrate, which connects to the aluminum film on the nanowire. This new technique allows lithographic process on the epitaxial film to be conducted away from the delicate superconductor-semiconductor interface and also allows growth of arbitrary semiconductor-superconductor networks.

Apart from in situ epitaxial growth of aluminum, tin has also been coated on InSb nanowires using MBE recently and results in very hard induced gap as well as two-electron charging effect [72]. Owing to the high T_c and the large coherence length of tin, this work, reported by Pendharkar et al opens future directions for heterostructure fabrication. Similarly, epitaxial Pd on InAs nanowires also yield promising results [120].

Advances in materials have also been made in 2D interfaces between Al and InAs [121, 122, 123]. Follw the proposal [124], quasi-1D system can also be engineered to hose MZMs with InAs 2DEG proximitized by an epitaxial Al layer. In such a system, phase difference Φ between the superconducting leads represents an additional tuning knob to the topological phase. Couple groups have already reported promising results [125, 126].

7.6 Outlook

Based on our results, I suggest that future experiments should focus on the unambiguous proof of well-separated MBSs in a short term as that is still an unfinished task. To achieve that goal, general improvements can be made in several directions. First, better induced superconductivity in the nanowire is always coveted. While epitaxial growth of superconducting shells on nanowires already exhibited promising induced superconducting gaps at zero magnetic field, further improvement is still necessary to achieve optimal induced gap at finite fields. Besides optimizing current methods, new techniques and new materials should definitely be explored. On the other direction, intrinsic topological superconductors should be searched for and may eventually provide an ultimate platform for MBSs.

Local electrostatic gates should also be further improved. As indicated by many theoretical simulations, non-ideal tunnel barriers, i.e. barriers with finite width and height, and non-uniform chemical potential inside the hybrid region can cause uncertainties and problems in identifying MBSs [83, 20, 127, 92]. In particular, a non-ideal tunnel barrier might be the breeding ground of trivial states, e.g. ABSs, and thus induce trivial ZBCPs. Those problems may get mitigated by optimizing the design and the flatness of the gates or using better dielectrics. Furthermore, growing a barrier inside the nanowire may also be an option to achieve optimal tunnel barriers [128].

For the experimental configuration, I strongly suggest that all the future Majorana tunneling measurement should be conducted in the three-terminal geometry. As proven by our results, three-terminal measurement is a powerful method to identify the localization of states. Instead of scrutinizing the difference between Majorana signal and trivial signal in a two-terminal geometry, three-terminal geometry provides a new dimension to identify MBSs by examining their non-locality.

While an unambiguous prove of MBSs seems still a tough task and the road to Majorana braiding and topological quantum computation is even longer and more arduous, we can already discern the glorious future, as the road is lightened by the wisdom and dream of brilliant people!

Appendix A Fabrication Recipes

Substrate preparation for EBL:

- Rinse chips in Acetone for 1 hour and IPA for 1 hour
- Apply oxygen plasma for 2 min to clean residue

Recipe for global markers:

- PMMA coating: PMMA 950 A4 at 5000rpm for 1 min; bake at 175°C for 15 min
- Using EBL to define global markers patterns on PMMA
- Developing: 60 s MIBK:IPA (1:3); 60 s IPA
- Removal of PMMA residue: low power oxygen plasma for 15 s
- Deposition: Evaporation of 5 nm Ti and 50 nm Au
- Lift-off in Acetone for 2 hours

Recipe for local bottom gates:

- PMMA coating: PMMA 950 A2 at 6000rpm for 1 min; bake at 175°C for 60 min
- Using EBL to define bottom gates patterns on PMMA
- Developing: 45 s MIBK:IPA (1:3); 45 s IPA
- Deposition: Evaporation of 3 nm Ti and 10 nm Pd30Au70 alloy
- Lift-off in Acetone for 12 hours and use ultrasound to ensure fully lift-off

Dielectric HfO_2 deposition:

- Using the same EBL recipe of global markers to define dielectric patterns on PMMA
- Setting all stages in ALD to 120°C
- For each deposition cycle: 0.015 s pulse of H_2O; wait 60 s; 0.15 s pulse of Hf(NMe2)4; wait 60s
- Deposition of 110 cycles for approximate 12 nm HfO_2
- Lift-off in Acetone for 12 hours

Recipe for normal and superconducting contacts:

- SEM imaging of nanowires for contact design.

- PMMA coating: PMMA 950 A4 at 5000rpm for 1 min; bake at 175°C for 15 min
- Using EBL to define contact patterns on PMMA
- Developing: 60 s MIBK:IPA (1:3); 60 s IPA
- Removal of PMMA residue: low power oxygen plasma for 15 s
- Using Sulfur passivation to remove native oxide
- Further cleaning with in-situ gentle sputter cleaning(20 s with 20 W power under 10 mbar argon pressure)
- Normal contact deposition: Evaporation of 15 nm Ti and 120 nm Pd; Superconducting deposition: Sputtering 5nm NbTi and 60-120 nm NbTiN
- Lift-off in Acetone for 2 hours

Sulfur passivation recipe 1:

- Mixing 0.29 g sulfur with 3 ml $(NH_4)_2\,S$ to get ammonium polysulfide solution $(NH_4)_2\,S_x$
- Diluting ammonium polysulfide solution with DI water at a ration of 1:500
- Passivating the device chip with 10 ml diluted solution for 30 min while heated by a hot plate at 60°C
- Rinse the device chip with DI water for 10 s and transfer the chip to deposition chamber

Sulfur passivation recipe 2:

- Mix 0.29 g sulfur with 3 ml $(NH_4)_2\,S$ to get ammonium polysulfide solution $(NH_4)_2\,S_x$
- Dilute ammonium polysulfide solution with DI water at a ration of 1:200
- Put device chip into a beaker with 10 ml diluted solution and heat the beaker in a water bath at 60°C for 30 min. Cover the the beaker with foil to prevent light exposure
- Rinse the device chip with DI water for 10 s and transfer the chip to deposition chamber

Appendix B List of Publications

Yu, P., Chen, J., Gomanko, M., Badawy, G., Bakkers, E.P.A.M., Zuo, K., Mourik, V., Frolov, S.M.. Non-Majorana states yield nearly quantized conductance in superconductor-semiconductor nanowire devices. arXiv:2004.08583. *Nature Physics* (in publishing).

Yu, P., Woods, B. D., Chen, J., Badawy, G., Bakkers, E.P.A.M., Stanescu, T. D., Frolov, S.M.. Delocalizd states in three-terminal nanowire-superconductor hybrid devices (in preparation).

Chen, J., **Yu, P.(co-first author),**Stenger, J., Hocevar, M., Car, D., Plissard, S. R., Bakkers, E.P.A.M., Stanescu, T. D., Frolov, S.M.. Experimental phase diagram of zero-bias conductance peaks in super-conductor/semiconductor nanowire devices. *Science Advances* **3**, e1701476 (2017).

Chen, J., Woods, B. D., **Yu, P.**, Hocevar, M., Car, D., Plissard, S. R., Bakkers, E.P.A.M., Stanescu, T. D., Frolov, S.M.. Ubiquitous non-Majorana Zero-Bias Conductance Peaks in Nanowire Devices. *Phys. Rev. Lett.* **123**, 107703 (2019).

Bibliography

[1] Wimmer, M., Akhmerov, A. R., Dahlhaus, J. P. & Beenakker, C. W. J. Quantum point contact as a probe of a topological superconductor. *New Journal of Physics* **13**, 053016 (2011).

[2] Dirac, P. A. M. & Fowler, R. H. The quantum theory of the electron. *Proceedings of the Royal Society of London. Series A, Containing Papers of a Mathematical and Physical Character* **117**, 610–624 (1928).

[3] Anderson, C. D. The positive electron. *Phys. Rev.* **43**, 491–494 (1933).

[4] Majorana, E. Teoria simmetrica dell'elettrone e del positrone. *Il Nuovo Cimento (1924-1942)* **14**, 171 (1937).

[5] Avignone, F. T., Elliott, S. R. & Engel, J. Double beta decay, majorana neutrinos, and neutrino mass. *Rev. Mod. Phys.* **80**, 481–516 (2008).

[6] Kitaev, A. Fault-tolerant quantum computation by anyons. *Annals of Physics* **303**, 2 – 30 (2003).

[7] Nayak, C., Simon, S. H., Stern, A., Freedman, M. & Das Sarma, S. Non-abelian anyons and topological quantum computation. *Rev. Mod. Phys.* **80**, 1083–1159 (2008).

[8] Ivanov, D. A. Non-abelian statistics of half-quantum vortices in p-wave superconductors. *Phys. Rev. Lett.* **86**, 268–271 (2001).

[9] Fu, L. & Kane, C. L. Superconducting proximity effect and majorana fermions at the surface of a topological insulator. *Phys. Rev. Lett.* **100**, 096407 (2008).

[10] Lutchyn, R. M., Sau, J. D. & Das Sarma, S. Majorana fermions and a topological phase transition in semiconductor-superconductor heterostructures. *Phys. Rev. Lett.* **105**, 077001 (2010).

[11] Oreg, Y., Refael, G. & von Oppen, F. Helical liquids and majorana bound states in quantum wires. *Physical review letters* **105**, 177002 (2010).

[12] Mourik, V. *et al.* Signatures of majorana fermions in hybrid superconductor-semiconductor nanowire devices. *Science* **336**, 1003–1007 (2012).

[13] Moore, G. & Read, N. Nonabelions in the fractional quantum hall effect. *Nuclear Physics B* **360**, 362 – 396 (1991).

[14] Read, N. & Green, D. Paired states of fermions in two dimensions with breaking of parity and time-reversal symmetries and the fractional quantum hall effect. *Phys. Rev. B* **61**, 10267–10297 (2000).

[15] Sarma, S. D., Freedman, M. & Nayak, C. Majorana zero modes and topological quantum computation. *npj Quantum Information* **1**, 15001 (2015).

[16] Qi, X.-L. & Zhang, S.-C. Topological insulators and superconductors. *Rev. Mod. Phys.* **83**, 1057–1110 (2011).

[17] Alicea, J. New directions in the pursuit of majorana fermions in solid state systems **75**, 076501 (2012).

[18] Leijnse, M. & Flensberg, K. Introduction to topological superconductivity and majorana fermions **27**, 124003 (2012).

[19] Elliott, S. R. & Franz, M. Colloquium: Majorana fermions in nuclear, particle, and solid-state physics. *Rev. Mod. Phys.* **87**, 137–163 (2015).

[20] Stanescu, T. D. & Tewari, S. Majorana fermions in semiconductor nanowires: fundamentals, modeling, and experiment. *Journal of Physics: Condensed Matter* **25**, 233201 (2013).

[21] Kitaev, A. Y. Unpaired majorana fermions in quantum wires. *Physics-Uspekhi* **44**, 131–136 (2001).

[22] Tinkham, M. *Introduction to Superconductivity* (Dover Publications, 2004), 2 edn.

[23] Nayak, C. & Wilczek, F. 2n-quasihole states realize 2n1-dimensional spinor braiding statistics in paired quantum hall states. *Nuclear Physics B* **479**, 529 – 553 (1996).

[24] Stern, A., von Oppen, F. & Mariani, E. Geometric phases and quantum entanglement as building blocks for non-abelian quasiparticle statistics. *Phys. Rev. B* **70**, 205338 (2004).

[25] Hyart, T. *et al.* Flux-controlled quantum computation with majorana fermions. *Phys. Rev. B* **88**, 035121 (2013).

[26] Takei, S., Fregoso, B. M., Hui, H.-Y., Lobos, A. M. & Das Sarma, S. Soft superconducting gap in semiconductor majorana nanowires. *Phys. Rev. Lett.* **110**, 186803 (2013).

[27] van Woerkom, D. J., Geresdi, A. & Kouwenhoven, L. P. One minute parity lifetime of a nbtin cooper-pair transistor. *Nature Physics* **11**, 547–550 (2015).

[28] Sau, J. D., Lutchyn, R. M., Tewari, S. & Das Sarma, S. Robustness of majorana fermions in proximity-induced superconductors. *Phys. Rev. B* **82**, 094522 (2010).

[29] Maeno, Y. *et al.* Superconductivity in a layered perovskite without copper. *Nature* **372**, 532–534 (1994).

[30] Talantsev, E. F. *et al.* p-wave superconductivity in iron-based superconductors. *Scientific Reports* **9**, 14245 (2019).

[31] Rex, S. & Sudbø, A. Tilting of the magnetic field in majorana nanowires: Critical angle and zero-energy differential conductance. *Physical Review B* **90** (2014).

[32] Doh, Y.-J. *et al.* Tunable supercurrent through semiconductor nanowires. *Science* **309**, 272–275 (2005).

[33] Stanescu, T. D., Lutchyn, R. M. & Das Sarma, S. Majorana fermions in semiconductor nanowires. *Phys. Rev. B* **84**, 144522 (2011).

[34] Nijholt, B. & Akhmerov, A. R. Orbital effect of magnetic field on the majorana phase diagram. *Phys. Rev. B* **93**, 235434 (2016).

[35] Das Sarma, S., Sau, J. D. & Stanescu, T. D. Splitting of the zero-bias conductance peak as smoking gun evidence for the existence of the majorana mode in a superconductor-semiconductor nanowire. *Phys. Rev. B* **86**, 220506 (2012).

[36] Stanescu, T. D., Lutchyn, R. M. & Das Sarma, S. Dimensional crossover in spin-orbit-coupled semiconductor nanowires with induced superconducting pairing. *Phys. Rev. B* **87**, 094518 (2013).

[37] Law, K. T., Lee, P. A. & Ng, T. K. Majorana fermion induced resonant andreev reflection. *Phys. Rev. Lett.* **103**, 237001 (2009).

[38] Woods, B. D., Chen, J., Frolov, S. M. & Stanescu, T. D. Zero-energy pinning of topologically trivial bound states in multiband semiconductor-superconductor nanowires. *Phys. Rev. B* **100**, 125407 (2019).

[39] Pan, H., Cole, W. S., Sau, J. D. & Das Sarma, S. Generic quantized zero-bias conductance peaks in superconductor-semiconductor hybrid structures. *Phys. Rev. B* **101**, 024506 (2020).

[40] Moore, C., Zeng, C., Stanescu, T. D. & Tewari, S. Quantized zero-bias conductance plateau in semiconductor-superconductor heterostructures without topological majorana zero modes. *Phys. Rev. B* **98**, 155314 (2018).

[41] Lee, E. J. *et al.* Spin-resolved andreev levels and parity crossings in hybrid superconductor-semiconductor nanostructures. *Nature nanotechnology* **9**, 79–84 (2014).

[42] Liu, C.-X., Sau, J. D. & Das Sarma, S. Distinguishing topological majorana bound states from trivial andreev bound states: Proposed tests through differential tunneling conductance spectroscopy. *Phys. Rev. B* **97**, 214502 (2018).

[43] Moore, C., Stanescu, T. D. & Tewari, S. Two-terminal charge tunneling: Disentangling majorana zero modes from partially separated andreev bound states in semiconductor-superconductor heterostructures. *Phys. Rev. B* **97**, 165302 (2018).

[44] Nilsson, H. A., Samuelsson, P., Caroff, P. & Xu, H. Q. Supercurrent and multiple andreev reflections in an insb nanowire josephson junction. *Nano Letters* **12**, 228–233 (2012).

[45] Gül, *et al.* Hard superconducting gap in insb nanowires. *Nano Letters* **17**, 2690–2696 (2017).

[46] Plissard, S. R. *et al.* From insb nanowires to nanocubes: Looking for the sweet spot. *Nano Letters* **12**, 1794–1798 (2012).

[47] Nilsson, H. A. *et al.* Giant, level-dependent g factors in insb nanowire quantum dots. *Nano Letters* **9**, 3151–3156 (2009).

[48] Thoen, D. J. *et al.* Superconducting nbtin thin films with highly uniform properties over a 100 mm wafer. *IEEE Transactions on Applied Superconductivity* **27**, 1–5 (2017).

[49] Önder Gül *et al.* Towards high mobility InSb nanowire devices. *Nanotechnology* **26**, 215202 (2015).

[50] Kammhuber, J. *et al.* Conductance quantization at zero magnetic field in insb nanowires. *Nano Letters* **16**, 3482–3486 (2016).

[51] Nadj-Perge, S. *et al.* Spectroscopy of spin-orbit quantum bits in indium antimonide nanowires. *Phys. Rev. Lett.* **108**, 166801 (2012).

[52] Caroff, P. *et al.* High-quality inas/insb nanowire heterostructures grown by metal–organic vapor-phase epitaxy. *Small* **4**, 878–882 (2008).

[53] Badawy, G. *et al.* High mobility stemless insb nanowires. *Nano Letters* **19**, 3575–3582 (2019).

[54] Flöhr, K. *et al.* Manipulating inas nanowires with submicrometer precision. *Review of Scientific Instruments* **82**, 113705 (2011).

[55] Tang, X., van Welzenis, R. G., van Setten, F. M. & Bosch, A. J. Oxidation of the InSb surface at room temperature. *Semiconductor Science and Technology* **1**, 355–365 (1986).

[56] Lie, F., Rachmady, W. & Muscat, A. A comparison of liquid and gas phase surface preparation of iii–v compound semiconductors for atomic layer deposition. *Microelectronic Engineering* **86**, 122 – 127 (2009). The 10th annual SEMATECH Surface Preparation and Cleaning Conference (SPCC).

[57] Suyatin, D. B., Thelander, C., Björk, M. T., Maximov, I. & Samuelson, L. Sulfur passivation for ohmic contact formation to InAs nanowires. *Nanotechnology* **18**, 105307 (2007).

[58] Webb, J. L. *et al.* Electrical and surface properties of inas/insb nanowires cleaned by atomic hydrogen. *Nano Letters* **15**, 4865–4875 (2015).

[59] Gazibegovic, S. *et al.* Epitaxy of advanced nanowire quantum devices. *Nature* **548**, 434–438 (2017).

[60] Pobell, F. *Matter and Methods at Low Temperatures* (Springer Science Business Media, 2007).

[61] Janssen, R. M. J. *et al.* High optical efficiency and photon noise limited sensitivity of microwave kinetic inductance detectors using phase readout. *Applied Physics Letters* **103**, 203503 (2013).

[62] Endo, A. *et al.* On-chip filter bank spectroscopy at 600–700ghz using nbtin superconducting resonators. *Applied Physics Letters* **103**, 032601 (2013).

[63] Ho Eom, B., Day, P. K., LeDuc, H. G. & Zmuidzinas, J. A wideband, low-noise superconducting amplifier with high dynamic range. *Nature Physics* **8**, 623–627 (2012).

[64] Zhang, L., Peng, W., You, L. X. & Wang, Z. Superconducting properties and chemical composition of nbtin thin films with different thickness. *Applied Physics Letters* **107**, 122603 (2015).

[65] Machhadani, H. *et al.* Improvement of the critical temperature of NbTiN films on III-nitride substrates. *Superconductor Science and Technology* **32**, 035008 (2019).

[66] Gill, S. T. *et al.* Selective-area superconductor epitaxy to ballistic semiconductor nanowires. *Nano Letters* **18**, 6121–6128 (2018).

[67] van Wees, B. J. *et al.* Quantized conductance of point contacts in a two-dimensional electron gas. *Phys. Rev. Lett.* **60**, 848–850 (1988).

[68] Wharam, D. A. *et al.* One-dimensional transport and the quantisation of the ballistic resistance. *Journal of Physics C: Solid State Physics* **21**, L209–L214 (1988).

[69] van Weperen, I., Plissard, S. R., Bakkers, E. P. A. M., Frolov, S. M. & Kouwenhoven, L. P. Quantized conductance in an insb nanowire. *Nano Letters* **13**, 387–391 (2013).

[70] Krogstrup, P. *et al.* Epitaxy of semiconductor–superconductor nanowires. *Nature Materials* **14**, 400–406 (2015).

[71] Vaitiekėnas, S. *et al.* Selective-area-grown semiconductor-superconductor hybrids: A basis for topological networks. *Phys. Rev. Lett.* **121**, 147701 (2018).

[72] Pendharkar, M. *et al.* Parity-preserving and magnetic field resilient superconductivity in indium antimonide nanowires with tin shells (2019).

[73] Flensberg, K. Tunneling characteristics of a chain of majorana bound states. *Phys. Rev. B* **82**, 180516 (2010).

[74] Sengupta, K., Žutić, I., Kwon, H.-J., Yakovenko, V. M. & Das Sarma, S. Midgap edge states and pairing symmetry of quasi-one-dimensional organic superconductors. *Phys. Rev. B* **63**, 144531 (2001).

[75] Zareyan, M., Belzig, W. & Nazarov, Y. V. Superconducting proximity effect in clean ferromagnetic layers. *Phys. Rev. B* **65**, 184505 (2002).

[76] Sasaki, S. *et al.* Kondo effect in an integer-spin quantum dot. *Nature* **405**, 764–767 (2000).

[77] Pikulin, D. I., Dahlhaus, J. P., Wimmer, M., Schomerus, H. & Beenakker, C. W. J. A zero-voltage conductance peak from weak antilocalization in a majorana nanowire. *New Journal of Physics* **14**, 125011 (2012).

[78] Bagrets, D. & Altland, A. Class d spectral peak in majorana quantum wires. *Phys. Rev. Lett.* **109**, 227005 (2012).

[79] Liu, C.-X., Sau, J. D. & Das Sarma, S. Role of dissipation in realistic majorana nanowires. *Phys. Rev. B* **95**, 054502 (2017).

[80] Kells, G., Meidan, D. & Brouwer, P. W. Near-zero-energy end states in topologically trivial spin-orbit coupled superconducting nanowires with a smooth confinement. *Phys. Rev. B* **86**, 100503 (2012).

[81] Vuik, A., Nijholt, B., Akhmerov, A. R. & Wimmer, M. Reproducing topological properties with quasi-Majorana states. *SciPost Phys.* **7**, 61 (2019).

[82] Moore, C., Zeng, C., Stanescu, T. D. & Tewari, S. Quantized zero-bias conductance plateau in semiconductor-superconductor heterostructures without topological majorana zero modes. *Phys. Rev. B* **98**, 155314 (2018).

[83] Prada, E., San-Jose, P. & Aguado, R. Transport spectroscopy of ns nanowire junctions with majorana fermions. *Phys. Rev. B* **86**, 180503 (2012).

[84] Sau, J. D. & Das Sarma, S. Density of states of disordered topological superconductor-semiconductor hybrid nanowires. *Phys. Rev. B* **88**, 064506 (2013).

[85] Chen, J. *et al.* Ubiquitous non-majorana zero-bias conductance peaks in nanowire devices. *Phys. Rev. Lett.* **123**, 107703 (2019).

[86] Chen, J. *et al.* Experimental phase diagram of zero-bias conductance peaks in superconductor/semiconductor nanowire devices. *Science Advances* **3**, e1701476 (2017).

[87] Alicea, J., Oreg, Y., Refael, G., von Oppen, F. & Fisher, M. P. A. Non-abelian statistics and topological quantum information processing in 1d wire networks. *Nature Physics* **7**, 412–417 (2011).

[88] van Heck, B., Akhmerov, A. R., Hassler, F., Burrello, M. & Beenakker, C. W. J. Coulomb-assisted braiding of majorana fermions in a josephson junction array. *New Journal of Physics* **14**, 035019 (2012).

[89] Kouwenhoven, L. P., Austing, D. G. & Tarucha, S. Few-electron quantum dots. *Reports on Progress in Physics* **64**, 701 (2001).

[90] Albrecht, S. M. *et al.* Exponential protection of zero modes in majorana islands. *Nature* **531**, 206–209 (2016).

[91] Stanescu, T. D. & Tewari, S. Majorana fermions in semiconductor nanowires: fundamentals, modeling, and experiment. *Journal of Physics: Condensed Matter* **25**, 233201 (2013).

[92] Rainis, D., Trifunovic, L., Klinovaja, J. & Loss, D. Towards a realistic transport modeling in a superconducting nanowire with majorana fermions. *Phys. Rev. B* **87**, 024515 (2013).

[93] Domínguez, F. *et al.* Zero-energy pinning from interactions in majorana nanowires. *npj Quantum Materials* **2**, 13 (2017).

[94] Cao, Z. *et al.* Decays of majorana or andreev oscillations induced by steplike spin-orbit coupling. *Phys. Rev. Lett.* **122**, 147701 (2019).

[95] Středa, P. & Šeba, P. Antisymmetric spin filtering in one-dimensional electron systems with uniform spin-orbit coupling. *Phys. Rev. Lett.* **90**, 256601 (2003).

[96] Motrunich, O., Damle, K. & Huse, D. A. Griffiths effects and quantum critical points in dirty superconductors without spin-rotation invariance: One-dimensional examples. *Phys. Rev. B* **63**, 224204 (2001).

[97] Brouwer, P. W., Duckheim, M., Romito, A. & von Oppen, F. Topological superconducting phases in disordered quantum wires with strong spin-orbit coupling. *Phys. Rev. B* **84**, 144526 (2011).

[98] Brouwer, P. W., Duckheim, M., Romito, A. & von Oppen, F. Probability distribution of majorana end-state energies in disordered wires. *Phys. Rev. Lett.* **107**, 196804 (2011).

[99] van Weperen, I., Plissard, S. R., Bakkers, E. P. A. M., Frolov, S. M. & Kouwenhoven, L. P. Quantized conductance in an insb nanowire. *Nano Letters* **13**, 387–391 (2013).

[100] Eichler, A. *et al.* Even-odd effect in andreev transport through a carbon nanotube quantum dot. *Physical review letters* **99**, 126602 (2007).

[101] Pientka, F., Kells, G., Romito, A., Brouwer, P. W. & von Oppen, F. Enhanced zero-bias majorana peak in the differential tunneling conductance of disordered multisubband quantum-wire/superconductor junctions. *Phys. Rev. Lett.* **109**, 227006 (2012).

[102] Lin, C.-H., Sau, J. D. & Das Sarma, S. Zero-bias conductance peak in majorana wires made of semiconductor/superconductor hybrid structures. *Phys. Rev. B* **86**, 224511 (2012).

[103] Rokhinson, L. P., Liu, X. & Furdyna, J. K. The fractional a.c. josephson effect in a semiconductor–superconductor nanowire as a signature of majorana particles. *Nature Physics* **8**, 795–799 (2012).

[104] Deng, M. T. *et al.* Anomalous zero-bias conductance peak in a nb–insb nanowire–nb hybrid device. *Nano Letters* **12**, 6414–6419 (2012).

[105] Das, A. *et al.* Zero-bias peaks and splitting in an al–inas nanowire topological superconductor as a signature of majorana fermions. *Nature Physics* **8**, 887–895 (2012).

[106] Churchill, H. O. H. *et al.* Superconductor-nanowire devices from tunneling to the multichannel regime: Zero-bias oscillations and magnetoconductance crossover. *Phys. Rev. B* **87**, 241401 (2013).

[107] Deng, M.-T. *et al.* Nonlocality of majorana modes in hybrid nanowires. *Phys. Rev. B* **98**, 085125 (2018).

[108] Finck, A. D. K., Van Harlingen, D. J., Mohseni, P. K., Jung, K. & Li, X. Anomalous modulation of a zero-bias peak in a hybrid nanowire-superconductor device. *Phys. Rev. Lett.* **110**, 126406 (2013).

[109] Suominen, H. J. *et al.* Zero-energy modes from coalescing andreev states in a two-dimensional semiconductor-superconductor hybrid platform. *Phys. Rev. Lett.* **119**, 176805 (2017).

[110] Nichele, F. *et al.* Scaling of majorana zero-bias conductance peaks. *Phys. Rev. Lett.* **119**, 136803 (2017).

[111] Laroche, D. *et al.* Observation of the 4π-periodic josephson effect in indium arsenide nanowires. *Nature Communications* **10**, 245 (2019).

[112] Anselmetti, G. L. R. *et al.* End-to-end correlated subgap states in hybrid nanowires. *Phys. Rev. B* **100**, 205412 (2019).

[113] Cohen, Y. *et al.* Nonlocal supercurrent of quartets in a three-terminal josephson junction. *Proceedings of the National Academy of Sciences* **115**, 6991–6994 (2018).

[114] Puglia, D. *et al.* Closing of the induced gap in a hybrid superconductor-semiconductor nanowire (2020). `2006.01275`.

[115] Stanescu, T. D., Tewari, S., Sau, J. D. & Das Sarma, S. To close or not to close: The fate of the superconducting gap across the topological quantum phase transition in majorana-carrying semiconductor nanowires. *Phys. Rev. Lett.* **109**, 266402 (2012).

[116] Mishmash, R. V., Aasen, D., Higginbotham, A. P. & Alicea, J. Approaching a topological phase transition in majorana nanowires. *Phys. Rev. B* **93**, 245404 (2016).

[117] van Weperen, I. *et al.* Spin-orbit interaction in insb nanowires. *Phys. Rev. B* **91**, 201413 (2015).

[118] Chang, W. *et al.* Hard gap in epitaxial semiconductor–superconductor nanowires. *Nature Nanotechnology* **10**, 232–236 (2015).

[119] Plissard, S. R. *et al.* Formation and electronic properties of insb nanocrosses. *Nature Nanotechnology* **8**, 859–864 (2013).

[120] Kanne, T. *et al.* Epitaxial Pb on InAs nanowires. *arXiv e-prints* arXiv:2002.11641 (2020). 2002.11641.

[121] Shabani, J. *et al.* Two-dimensional epitaxial superconductor-semiconductor heterostructures: A platform for topological superconducting networks. *Phys. Rev. B* **93**, 155402 (2016).

[122] Kjaergaard, M. *et al.* Transparent semiconductor-superconductor interface and induced gap in an epitaxial heterostructure josephson junction. *Phys. Rev. Applied* **7**, 034029 (2017). URL https://link.aps.org/doi/10.1103/PhysRevApplied.7.034029.

[123] Kjaergaard, M. *et al.* Quantized conductance doubling and hard gap in a two-dimensional semiconductor–superconductor heterostructure. *Nature Communications* **7**, 12841 (2016).

[124] Hell, M., Leijnse, M. & Flensberg, K. Two-dimensional platform for networks of majorana bound states. *Phys. Rev. Lett.* **118**, 107701 (2017).

[125] Ren, H. *et al.* Topological superconductivity in a phase-controlled josephson junction. *Nature* **569**, 93–98 (2019).

[126] Fornieri, A. *et al.* Evidence of topological superconductivity in planar josephson junctions. *Nature* **569**, 89–92 (2019).

[127] Stenger, J. & Stanescu, T. D. Tunneling conductance in semiconductor-superconductor hybrid structures. *Phys. Rev. B* **96**, 214516 (2017).

[128] Car, D. *et al.* Insb nanowires with built-in gaxin1–xsb tunnel barriers for majorana devices. *Nano Letters* **17**, 721–727 (2017).